SYNTHESIS OF SINGLE METAL AND BIMETALLIC CATHODE CATALYST FOR MICROBIAL FUEL CELLS USING M-BTC (M= Cu, Ni, Fe, Co)

by
Janset Otuzoğlu
B.S. Chemistry, Bilkent University, 2021

Submitted to the Institute for Graduate Studies in
Science and Engineering in partial fulfillment of
the requirements for the degree of
Master of Science

Graduate Program in Chemistry
Boğaziçi University
2024

Dedicated to my beloved father

ACKNOWLEDGMENTS

First and foremost, I would like to express my sincere gratitude to Assoc—Prof. Oktay Demircan, my advisor, whose knowledge, tolerance, and guidance were priceless. Your informative criticism and continuous support have been crucial to the accomplishment of this study. I am grateful for the numerous hours you spent examining my work and offering insightful feedback that shaped this thesis.

I would like to express my sincere gratitude to Professor Amitav Sanyal and Assoc. Professor Aligül Büyükaksoy for spending their important time reviewing my thesis as members of my thesis committee.

I thank Prof. Dr Arzu Çelik Fuss and Taha Akkülah from the Molecular Biology and Genetics Department of Boğaziçi University for their valuable contributions to the microbiology part of this thesis.

I want to thank Boğaziçi University for their financial support in the BAP project (Project No: 23B05P1).

A heartfelt thank you to my best friends Buse, Göksu, İpek, and Semanur. I was not too fond of the difficulties without your support and friendship. I appreciate my lab mates, my mentors Eslem and Müşerref, you have inspired and motivated me with your academic environment, companionship, and encouragement.

Special thanks to my family for their unwavering support and encouragement throughout my academic journey. To my father Cahit, my mother Nuran, my sister Azranur and my grandmother Safiye thank you for believing in me and providing me with the foundation to pursue my dreams. My big family, thank you all for your material and spiritual support. I am so lucky to have you. Finally, I dedicate this thesis to the memory of my deceased father.

ABSTRACT

SYNTHESIS OF SINGLE METAL AND BIMETALLIC CATHODE CATALYST FOR MICROBIAL FUEL CELLS WITH USING M-BTC (M= Cu, Ni, Fe, Co)

Metal-organic frameworks (MOFs) possess large surface area, high stability, and porous structure, making them suitable for oxygen reduction reaction catalysts in the cathode compartments of microbial fuel cells. In this study, 1,3,5-benzene tricarboxylic acid was used as an organic linker in metal-organic frameworks, and the metal centers were changed. For this purpose, Copper, Nickel, Cobalt, and Iron salts were used as metal sources. In addition to monometallic MOFs, bimetallic metal-organic frameworks were synthesized using copper-nickel and cobalt-iron pairs. Comparisons were made among copper, nickel, and copper-nickel BTC and cobalt, iron, and cobalt-iron BTC separately. Also, the solvent of the precursors was changed and a group of MOFs was synthesized using dimethylformamide (DMF) while the second group was synthesized with ammonia (NH_3) solvent. The effect of metal and solvent selection was examined. Sonochemically synthesized metal-organic frameworks were analyzed using X-ray diffraction (XRD), Scanning Electron Microscopy (SEM), and X-ray photoelectron Spectroscopy (XPS) techniques. Synthesized metal-organic frameworks as cathode catalysts in microbial fuel cells were applied by preparing slurries using carbon black as a carbon source and polyvinyl alcohol binder. The slurries were coated on stainless-steel meshes and coated meshes were analyzed before constructing Microbial fuel cells; Chronopotentiometry and Cyclic voltammetry (CV) were applied to meshes to obtain conductivity and oxygen reduction reaction activity information. The electrochemical properties of the MFC were obtained using electrochemical methods such as open-circuit voltage (OCV), electrochemical impedance spectroscopy (EIS), and linear sweep voltammetry (LSV).

ÖZET

M-BTC KULLANILARAK MİKROBİYAL YAKIT HÜCRELERİ İÇİN TEK METALLİ VE ÇİFT METALLİ KATOT KATALİZÖRÜ SENTEZLENMESİ

Metal-organik kafesler, yüksek yüzey alanı, kararlılık ve gözenekli yapıları nedeniyle mikrobiyal yakıt hücrelerinin katot bölümlerinde oksijen indirgeme reaksiyonu katalizörü olarak kullanılabilmektedirler. Bu çalışmada, metal organik kafesler içinde organik bağlayıcı olarak 1,3,5-trikarboksilik asit kullanıldı ve metal merkezler değiştirildi. Bu amaçla Bakır, Nikel, Kobalt ve Demir tuzları metal kaynakları olarak kullanıldı. Tek metalli metal organik kafeslerin yanı sıra, bakır-nikel ve kobalt-demir çiftleriyle çift metalli kafesler de sentezlendi. Bakır, nikel ve bakır-nikel kafesleri ile kobalt, demir ve kobalt-demir kafesleri ayrı olarak karşılaştırıldı. Sonokimyasal olarak sentezlenen metal organik kafesler X-ışını kırınım spektroskopisi, taramalı elektron mikroskobu ve X-ışını fotoelektron spektroskopisi teknikleri kullanılarak analiz edildi. Sentezlenen metal organik kafeslerin mikrobiyal yakıt hücrelerinde katot katalisti olarak uygulamaları karbon siyahı ve polivinil alkol kullanılarak çamur hazırlanması ile yapıldı. Bu çamurlar paslanmaz çelik süzgeçler üzerine kaplandı. Kaplanmış süzgeçler, mikrobiyal yakıt hücresinin kurulumundan önce analiz edildi; Kronopotansiyometri ve Dönüşümlü Voltametri, süzgeçlerin iletkenliklerini ve oksijen indirgeme reaksiyonu aktivitelerini ölçmek için yapıldı. Mikrobiyal yakıt hücresinin elektrokimyasal özellikleri, açık devre gerilimi, doğrusal taramalı voltametri ve elektrokimyasal empedans spektroskopisi ile elde edildi.

TABLE OF CONTENTS

ACKNOWLEDGMENTS iv

ABSTRACT v

ÖZET vi

LIST OF FIGURES ix

LIST OF TABLES xv

LIST OF SYMBOLS xvi

LIST OF ACRONYMS/ABBREVIATIONS xvii

1. INTRODUCTION 1

1.1. Microbial Fuel Cells (MFCs) 1

1.1.1. Working Principles 1

1.1.2. Factors Affecting Microbial Fuel Cell Performance 4

1.2. Metal-Organic Frameworks (MOFs) 7

1.2.1. Design and synthesis of Metal-Organic Frameworks (MOFs) 8

1.2.2. Factors Affecting MOF Synthesis 10

1.2.3. MOF Applications in MFCs 12

2. SCOPE OF THE THESIS 15

3. EXPERIMENTAL 16

3.1. Materials 16

3.2. Synthesis of Metal-Organic Frameworks (MOFs) 16

3.2.1. Dimethylformamide (DMF) Solvent 16

3.2.2. Ammonia (NH_3) Solvent 18

3.3. Preparation of Coated Stainless-Steel Mesh (SSM) Electrodes 19

3.3.1. SSM Electrodes Coated for Anode 19
3.3.2. SSM Electrodes Coated with MOF-CB for Cathode 20
3.4. Setup of MFC and Bacterial Inoculation 21
3.5. Characterization Methods 22
3.5.1. X-Ray Diffraction Analysis (XRD) 23
3.5.1. Scanning Electron Microscopy (SEM) 23
3.5.2. X-Ray Photoelectron Spectroscopy (XPS) 23
3.5.5. Electrochemical Impedance Spectroscopy (EIS) 25
3.5.6. Cyclic Voltammetry (CV) 25
3.5.7. Open Circuit Voltage Analysis (OCV) 25
3.5.8. Linear Sweep Voltammetry (LSV) 26
4. RESULTS AND DISCUSSION 27
4.1. Characterization of MOFs 27
4.1.1. MOFs Synthesized by Using DMF Solvent 27
4.2. Conductivities and ORR activities of Prepared Electrodes 45
4.2.1. SSMs Coated with Carbon Slurries 45
4.2.2. SSMs Coated with MOF Containing Slurries 46
4.3. Electrochemical Performance of SSM Electrodes in MFCs 54
5. CONCLUSION 69
6. FUTURE WORK 71
REFERENCES 72

LIST OF FIGURES

Figure 1.1. Schematic illustrations of (a) double-chamber and (b) single-chamber MFCs and their working mechanisms. 2

Figure 1.2. The electron transfer mechanism from microorganism to electrode through (a) direct electron transfer via cytochromes, (b) via nanowires and (c) mediated electron transfer. 4

Figure 1.3. Illustration of MOF formation. 8

Figure 1.4. Synthesis methods of MOFs. 9

Figure 3.1.Pictures of the synthesized MOFs, (a) FeBTC, (b) CoBTC, (c) FeCoBTC, (d) CuBTC, (e) NiBTC, and (f) CuNiBTC respectively. 17

Figure 3.2. Pictures of the synthesized MOFs, (a) CuBTC, (b) NiBTC, and (c) CuNiBTC respectively. 19

Figure 3.3. a) CoBTC, b) FeBTC, c) FeCoBTC, d) CuBTC, e) NiBTC and f) CuNiBTC. 21

Figure 3.4. a) CuBTC, b) NiBTC, and c) CuNiBTC. 21

Figure 3.5. Images of constructed MFC on operation. 22

Figure 3.6. Chronopotentiometry resulting graph for an example sample. 24

Figure 4.1. SEM images of FeBTC at a) 6000x, b) 25000x zoom level. 27

Figure 4.2. XRD pattern of FeBTC. 28

Figure 4.3. XPS pattern of FeBTC deconvoluted data a) XPS survey, b) Fe2p, c) O1s, and d) C1s. 28

Figure 4.4. SEM images of CoBTC at a) 1000x, b) 60000x zoom level..... 29

Figure 4.5. XRD pattern of CoBTC..... 30

Figure 4.6. XPS pattern of CoBTC deconvoluted data a) XPS survey, b) Co2p, c) O1s, and d) C1s..... 30

Figure 4.7. SEM images of FeCoBTC at a) 12000x, b) 50000x zoom level..... 31

Figure 4.8. XRD pattern of FeCoBTC..... 32

Figure 4.9. XPS pattern of FeCoBTC deconvoluted data a) XPS survey, b) Co2p, c) Fe2p, d) O1s, and e) C 1s..... 32

Figure 4.10. SEM images of CuBTC at a) 12000x, b) 50000x zoom level..... 33

Figure 4.11. XRD pattern of CuBTC..... 34

Figure 4.12. XPS pattern of CuBTC deconvoluted data a) XPS survey, b) Cu2p, c) O1s, and e) C 1s. 34

Figure 4.13. SEM images of NiBTC at a) 5000x, b) 100000x zoom level. 35

Figure 4.14. XRD pattern of NiBTC. 35

Figure 4.15. XPS pattern of NiBTC deconvoluted data a) XPS survey, b) Ni2p, c) O1s, and e) C 1s. 36

Figure 4.16. SEM images of CuNiBTC at a) 1000x, b) 8000x zoom level..... 37

Figure 4.17. XRD pattern of CuNiBTC..... 38

Figure 4.18. XPS pattern of CuNiBTC deconvoluted data a) XPS survey, b) Cu2p, c) Ni2p, d) O1s, and e) C 1s..... 38

Figure 4.19. SEM images of CuBTC at a) 50000x, b) 100000x zoom level..... 39

Figure 4.20. XRD pattern of CuBTC..... 40

Figure 4.21. XPS pattern of CuBTC deconvoluted data a) XPS survey, b) Cu2p, c) O1s, and e) C 1s..... 40

Figure 4.22. SEM images of NiBTC at a) 25000x, b) 100000x zoom level. 41

Figure 4.23. XRD pattern of NiBTC. 42

Figure 4.24. XPS pattern of NiBTC deconvoluted data a) XPS survey, b) Ni2p, c) O1s, and e) C 1s..... 42

Figure 4.25. SEM images of CuNiBTC at a) 24000x, b) 100000x zoom level..... 43

Figure 4.26. XRD pattern of CuNiBTC..... 44

Figure 4.27. XPS pattern of CuNiBTC deconvoluted data a) XPS survey, b) Cu2p, c) Ni2p, d) O1s, and e) C 1s..... 44

Figure 4.28. CV Curve of CB coated SSM (SSM#1) with O_2 purged and N_2 Purged at a scan rate of 50 mV/s..... 46

Figure 4.29. CV Curve of CB-CoBTC MOF composite coated SSM (SSM#2) with O_2 purged and N_2 Purged at a scan rate of 50 mV/s. 47

Figure 4.30. CV Curve of CB-FeBTC MOF composite coated SSM (SSM#3) with O_2 purged and N_2 Purged at a scan rate of 50 mV/s. 48

Figure 4.31. CV Curve of CB-FeCoBTC MOF composite coated SSM (SSM#4) with O_2 purged and N_2 Purged at a scan rate of 50 mV/s. 49

Figure 4.32. CV Curve of CB-CuBTC MOF composite coated SSM (SSM#5) with O_2 purged and N_2 Purged at a scan rate of 50 mV/s. 49

Figure 4.33. CV Curve of CB-NiBTC MOF composite coated SSM (SSM#6) with O_2 purged and N_2 Purged at a scan rate of 50 mV/s. 50

Figure 4.34. CV Curve of CB-CuNiBTC MOF composite coated SSM (SSM#7) with O_2 purged and N_2 Purged at a scan rate of 50 mV/s. 50

Figure 4.35. CV Curve of CB-CuBTC MOF composite coated SSM (SSM#8) with O_2 purged and N_2 Purged at a scan rate of 50 mV/s. 51

Figure 4.36. CV Curve of CB-NiBTC MOF composite coated SSM (SSM#9) with O_2 purged and N_2 Purged at a scan rate of 50 mV/s. 52

Figure 4.37. CV Curve of CB-CuNiBTC MOF composite coated SSM (SSM#10) with O_2 purged and N_2 Purged at a scan rate of 50 mV/s. 52

Figure 4.38.Maximum current density and maximum power density comparison between abiotic and biotic fuel cell constructed using CoBTC MOF (SSM #2) cathode catalyst. 55

Figure 4.39. EIS curve for MFC with CoBTC (SSM #2)..... 55

Figure 4.40. Maximum current density and maximum power density comparison between abiotic and biotic fuel cell constructed using FeBTC MOF (SSM #3) cathode catalyst..... 56

Figure 4.41. EIS curve for MFC with FeBTC (SSM#3). 57

Figure 4.42. Maximum current density and maximum power density comparison between abiotic and biotic fuel cell constructed using FeCoBTC MOF (SSM #4) cathode catalyst. 57

Figure 4.43. EIS curve for MFC with SSM#4 (FeCoBTC). 58

Figure 4.44. Maximum current density and maximum power density comparison between abiotic and biotic fuel cell constructed using CuBTC MOF (SSM #5) cathode catalyst. 58

Figure 4.45. EIS curve for MFC with CuBTC (SSM#5). 59

Figure 4.46. Maximum current density and maximum power density comparison between abiotic and biotic fuel cell constructed using NiBTC MOF (SSM #6) cathode catalyst. 60

Figure 4.47. EIS curve for MFC with NiBTC (SSM#6). 60

Figure 4.48. Maximum current density and maximum power density comparison between abiotic and biotic fuel cell constructed using CuNiBTC MOF (SSM #7) cathode catalyst. 61

Figure 4.49. EIS curve for MFC with CuNiBTC (SSM#7). 62

Figure 4.50. Maximum current density and maximum power density comparison between abiotic and biotic fuel cell constructed using CuBTC MOF (SSM #8) cathode catalyst. 63

Figure 4.51. EIS curve for MFC with CuBTC (SSM#8). 63

Figure 4.52. Maximum current density and maximum power density comparison between abiotic and biotic fuel cell constructed using NiBTC MOF (SSM #9) cathode catalyst..... 64

Figure 4.53. EIS curve for MFC with SSM#9 (NiBTC). 64

Figure 4.54. Maximum current density and maximum power density comparison between abiotic and biotic fuel cell constructed using CuNiBTC MOF (SSM #10) cathode catalyst. 65

Figure 4.55. EIS curve for MFC with CuNiBTC (SSM#10)..... 65

LIST OF TABLES

Table 3.1. SSM numbers of DMF solvent synthesis MOFs. 20

Table 3.2.SSM numbers of NH_3 solvent synthesis MOFs. 20

Table 4.1. Conductivity of SSM before and after the coating with CB-PVA-contained slurry. 45

Table 4.2. Conductivity values for Uncoated and MOF-CB composite coated SSMs. 47

Table 4.3. ORR Peak position table for MOF coated SSMs..... 53

Table 4.4. Comparison table for MOFs used in abiotic and biotic fuel cells..... 66

LIST OF SYMBOLS

λ	Wavelength
ρ	Resistivity
Ω	Resistance (ohm)
σ	Conductivity

LIST OF ACRONYMS/ABBREVIATIONS

2D	2-Dimensional
BMOF	Bimetallic Metal-Organic Framework
BTC	1,3,5-Benzenetricarboxylate
CB	Carbon black
CF	Carbon felt
CNT	Carbon nanotube
CV	Cyclic voltammetry
DET	Direct electron transfer
DMF	N, N-Dimethylformamide
DMSO	Dimethyl sulfoxide
EET	Extracellular electron transfer
EIS	Electrochemical Impedance Spectroscopy
EtOH	Ethanol
FC	Fuel cell
GO	Graphene oxide
HER	Hydrogen evolution reaction
HKUST	Hong Kong University of Science and Technology
H_3BTC	1,3,5-Benzenetricarboxylic acid
LSV	Linear Sweep Voltammetry
MeOH	Methanol
MET	Mediated electron transfer
MFC	Microbial fuel cell
MIL	Material Institute Lavoisier
MOF	Metal-Organic Framework
NaOH	Sodium hydroxide
OCP	Open Circuit Potential

OCV	Open Circuit Voltage
OER	Oxygen evolution reaction
ORR	Oxygen reduction reaction
PB	Phosphate buffer
PEM	Proton exchange membrane
PTFE	Polytetrafluoroethylene
PVA	Polyvinyl alcohol
RT	Room temperature
SBU	Secondary building unit
SEM	Scanning Electron Microscope
SS	Stainless-steel
TEA	Terminal electron acceptor
TPA	Terephthalic acid
US	Ultrasound
w %	Weight Percent
XPS	X-Ray Photoelectron Spectroscopy
XRD	X-Ray Diffraction Analysis
ZIF	Zeolitic Imidazolate Framework

1. INTRODUCTION

1.1. Microbial Fuel Cells (MFCs)

The increasing shortage of energy sources and the environmental drawbacks associated with using fossil fuels have accelerated the global energy crisis. This crisis has encouraged researchers to explore alternative sustainable energy sources. Thus, there is a significant increase in the utilization of renewable energy sources, such as solar, wind, and hydrogen. Among these alternatives, fuel cells have also been developed. William Grove invented the fuel cell concept using hydrogen, methanol, and waste as an energy production tool. Owing to the diversity of fuel cells, their applications are diverse and extensive. In 1911, Michael Cresse Potter explored the Microbial Fuel Cells (MFCs) and proposed to employ bacterial metabolism to produce electricity [1]. Microbial Fuel cells are devices that convert chemical energy into electrochemical energy through the activity of microorganisms. Microbial fuel cells are recognized in wastewater treatment because they are cost-effective and environmentally friendly [2]. These characteristics make MFCs an attractive option for sustainable energy production.

1.1.1. Working Principles

Microbial fuel cells (MFCs) represent an emerging technology that competes with energy demand, which makes it possible to produce energy from the degradation of organic matter through microbial activity. MFCs have a basic configuration similar to conventional fuel cells, consisting of an anode, cathode, and a porous membrane (Figure 1.1.a). The membrane separates the chambers while allowing to travel of protons (H^+). The difference between conventional and microbial fuel cells is that MFCs produce electricity from the metabolic activities of microorganisms. The anode chamber contained an anode electrode, bacteria, and a substrate. Bacteria are used as biocatalysts to oxidize substrates and produce electrons and protons. Carbon dioxide (CO_2) molecules are produced due to substrate

degradation. The cathode chamber consisted of a cathode electrode, catalyst, and oxygen (O_2) gas. With the help of an external circuit, the produced electrons move towards the cathode chamber, while protons travel through the membrane. In the cathode chamber, oxygen is reduced and combined with protons to form water molecules; here oxygen is used as the terminal electron acceptor (TEA) because of its low cost, sustainability, and environmentally friendly nature [3]. MFCs are ideal for application in wastewater treatment because of their dual capability to purify water while simultaneously generating electricity.

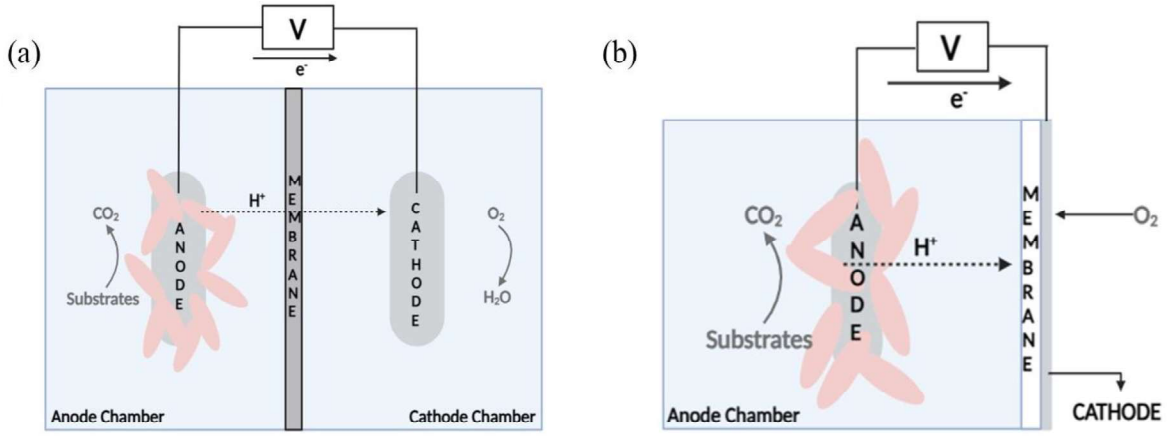

Figure 1.1. Schematic illustrations of (a) double-chamber and (b) single-chamber MFCs and their working mechanisms.

Substrate selection in MFCs varies, leading to different reaction pathways based on the substrates utilized. The most common substrates are acetate and glucose. The reaction pathway for acetate as a substrate is as follows [4]. The following equations show the anodic, cathodic, and overall reactions

$$CH_3COOH + H_2O \rightarrow 2CO_2 + 8H^+ + 8e^- \qquad E = -0.300\ V \qquad (1.1)$$

$$2O_2 + 8e^- + 8H^+ \rightarrow 4H_2O \qquad E = 0.805\ V \qquad (1.2)$$

$$CH_3COOH + 2O_2 \rightarrow 2H_2O + 2CO_2 \qquad E = 1.105\ V. \qquad (1.3)$$

In the anode chamber, acetate is degraded to produce carbon dioxide, protons, and electrons in the presence of bacteria. The electrons are transferred to the cathode via an external circuit, while the protons pass through the separator. As a result, water molecules are produced.

A similar pathway is observed when glucose is employed as a substrate. The following reactions occur if glucose is used as the substrate [5]. The anodic and cathodic reactions are given in the following equations

$C_6H_{12}O_6 + 6H_2O \rightarrow 6CO_2 + 24H^+ + 24e^-$ $E^0 = 0.014$ V (1.4)

$6O_2 + 24H^+ + 24e^- \rightarrow 12H_2O$ $E^0 = 1.23$ V. (1.5)

A device is considered a bio battery rather than an MFC if its fuel supply, which is oxidized at the substrate-anode interface, cannot be refilled intermittently or continuously. Most MFC setups are frequently used as anaerobic devices. This is because bacterial species that are now considered the high standard in terms of electron transport capabilities require anaerobic environments [6].

Although certain bacteria are capable of delivering electrons directly to the electrode, this is not always the case. Specifically, two species, Geobacter sulfurreducens, and Shewanella oneidensis can be recognized as being known as electrogens and hence the most studied [7]. These two species can interact with the electrode in two ways: directly through cytochromes or pili/nanowires (direct electron transfer mechanism, DET) and indirectly through anchoring electrons on soluble compounds that function as mediators (added to the system or self-produced) between the electrode and the cell (mediated electron transfer mechanism, MET) [8]. Numerous bacteria, including Pseudomonas aeruginosa, Shewanella oneidensis, and Pseudomonas alcaliphila, can independently generate redox mediators. For instance, it has been determined that P. aeruginosa's electrochemical activity is caused by pyocianine pigment [9].

Mediated electron transfer, in which the movement of electrons is facilitated by soluble redox mediators; these mediators can be endogenous electron "shuttles" or exogenous ones, which may be synthetic or natural. Because they are harmful and require constant supply, synthetic exogenous mediators put the MFC's sustainability for technological and environmental improvement in danger. However, in cases where the bacteria produce its shuttles as secondary metabolites, i.e., endogenous redox mediators, exogenous mediators are not required to carry out the mediation process [10]. Figure 1.2 illustrates the electron transfer mechanisms for direct electron transfer (DET) and mediated electron transfer (MET).

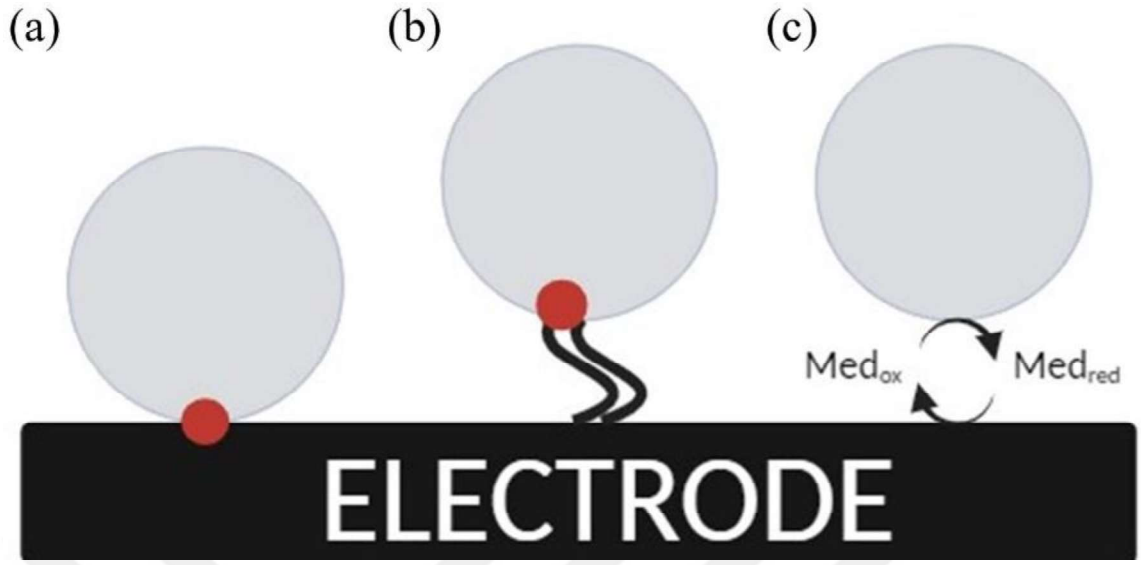

Figure 1.2. The electron transfer mechanism from microorganism to electrode through (a) direct electron transfer via cytochromes, (b) via nanowires and (c) mediated electron transfer.

1.1.2. Factors Affecting Microbial Fuel Cell Performance

In Microbial Fuel Cell (MFC) research, the primary objective is to improve the current density and power density output. Several factors affect MFC performance. Generally, the cathode is considered the main limiting factor because of the oxygen reduction reaction that occurs in the cathodic chamber. In addition, the MFC configuration, membrane, microorganisms, substrates, and anode are also effective in improving MFC performance.

The performance of an MFC depends on its configuration. The power density output can be increased by changing the size of the electrodes, membrane, reactor size, and the distance between the electrodes. Janicek et al. showed that lowering the distance between the anode and cathode electrodes causes a decrease in internal resistance [11]. There are two common types of MFC design configurations: single and double chambers. Although their fundamental principles are similar, differences arise from the use of a membrane/separator between the anode and cathode chambers. In other words, in double-chamber MFCs, there is a membrane separating the anode and cathode compartments, whereas in single-chamber MFCs, there is an anode compartment, and the cathode is exposed [12]. A single-chamber MFC configuration may also contain a membrane, which is possible using a sandwich

configuration [13]. Double chamber MFC is the most utilized type of microbial fuel cell. Figure 1.1. demonstrates both kinds of microbial fuel cells.

Nafion is the most recognized membrane for double-chamber MFCs. In single-chamber MFCs, an air cathode utilizes oxygen as a terminal electron acceptor (TEA). In double-chamber MFCs, oxygen is also used, in addition to oxygen, permanganate, and ferricyanide can be employed as electron acceptors. The structural differences between the two configurations lead to advantages and disadvantages. Single-chamber MFCs are advantageous since they are cost-effective and have reduced cell volume. However, owing to the absence of a membrane between the anode and cathode, both electrodes are in direct contact with the bacteria. This leads to the formation of a biofilm on the cathode. Biofilm formation causes increasing proton transfer resistance, thereby decreasing efficiency. However, single-chamber MFCs are advantageous for biosensors and large-scale applications [14]. Consequently, double-chamber MFCs are the most conventional and are preferred for the construction of MFCs in small-scale applications.

Membranes essentially divide the anode and cathode compartments. They are considered the most significant component of an MFC, as they are responsible for proton transfer and interference in the diffusion of oxygen [15]. While a membrane separates the anode and cathode compartments in a double-chamber MFC, it isolates the cathode from the anode in a single-chamber MFC [16]. The types of membranes include ion-exchange membrane, anion-exchange membrane, cation-exchange membrane, and porous membrane. In the selection of an appropriate membrane for MFC, properties such as ion conductivity, cost-effectiveness, internal resistance, selectivity, chemical, thermal, and mechanical stability, and fouling resistance should be considered. Nafion is the most widely utilized membrane in MFC construction owing to its high ionic conductivity. Nafion is a copolymer comprising a hydrophobic fluorocarbon backbone and a hydrophilic group attached to it. The high level of ionic conductivity is attributed to the negatively charged hydrophilic sulfonate groups [1].

The substrate is another factor that influences the performance and power generation ability of MFC. Substrates are related to the activity of microbes present in the anode since they provide nutrients to them. The substrate is also called ‘anolyte’ since it is present in the

anode chamber as a liquid solution. The most frequently utilized substrates are glucose, acetate, brewery effluents, and inorganic substrates [12]. The capacity of a microorganism to donate electrons is called exoelectrogen, and few microorganisms are exoelectrogenic. The electron transfer mechanism to the anode can be divided into three types: direct contact, using nanowires, and using mediators.

The performance and efficiency of an MFC depend on the choice of an appropriate anode material, particularly for large-scale applications. The anode plays a crucial role in oxidation reactions, and to obtain stable biofilm formation, the anode surface should be eligible for bacterial adhesion. Stable biofilm formation is essential for an effective electron transfer. An ideal anode material should exhibit biocompatibility, as it comes into direct contact with bacteria and high conductivity for electron transfer. Furthermore, an ideal anode material should be highly porous and have a high surface area [15].

The cathode electrode is the main component of an MFC because it has a significant effect on its overall performance. The selection of the material and surface area of the cathode electrodes, cathode catalysts, and type of electron acceptor is crucial. An effective oxygen reduction reaction takes place at the cathode making a microbial fuel cell produce higher energy. Carbon-based materials, such as carbon paper and graphite felt, are generally utilized in MFC construction [2]. However, the overpotential of carbon limits the MFC performance. The surface area of the cathode electrode also plays a crucial role, as the higher the surface area, the higher the cathodic reaction efficiency. Various materials, such as stainless steel, have been employed to increase the surface area. Oxygen reduction reaction (ORR) could follow two different pathways. The first one is a two-electron pathway which is called a partial reduction pathway that produces hydrogen peroxide (H_2O_2). The second mechanism does not involve the production of hydrogen peroxide and it is called four electron pathway. The mechanism depends on the selection of cathode material and catalyst [17].

Cathodic electron acceptors are generally oxidants with high redox potentials, and several types of acceptors, such as ferricyanide, permanganate, and hydrogen peroxide, are commonly employed. However, these materials cannot be regenerated through oxidation with oxygen [2]. According to Rabaey and Verstrate, MFC performance is related to the

reactions between the substrate and a final electron acceptor with high potential, such as oxygen [13]. Therefore, oxygen is the most frequently utilized TEA in MFC.

Operational conditions, including cathode oxidant concentration, temperature, and pH, influence MFC performance. Decreasing the pH promotes cathode performance, whereas temperature controls the kinetics of oxidant reduction, mass reduction, and proton transfer [2].

1.2. Metal-Organic Frameworks (MOFs)

Metal-organic frameworks (MOFs) are highly crystalline and porous structures composed of metal centers connected by organic compounds. In 1965, E.A. Tomic investigated these solids, and the combination of a high surface area and the presence of both inorganic and organic units makes MOFs highly attractive in the field. Metal centers are called inorganic secondary building units (SBUs), whereas organic linkers are called organic secondary building units [18, 19]. The applications of metal-organic frameworks vary according to specific requirements.

From a catalytic perspective, MOF materials provide several significant advantages over other materials that are commonly used as catalysts, including zeolites, clays, and mesoporous silica. Among the several potentialities of MOFs, the properties such as the structural tunability; the diversity of its constituent parts, such as linkers, nodes, and pores; different catalytic sites within a single MOF; the highly adjustable and homogeneous porous environments; the framework's well-defined and adjustable nature enables comprehension of the catalytic mechanism; the molecular structure-function relationship; and rigorous catalysis in a broad range of catalytic reactions are the most noteworthy ones of MOFs.

Various metals and organic linkers can be used to synthesize MOFs. Each MOF has unique properties and nomenclature. MOF nomenclatures vary based on conditions and changes in the naming of MOFs. They can be named after the metal utilized in synthesis, such as Cu-MOF and Fe-MOF, and the place where they were discovered, such as MIL (Material Institut Lavoisier), UiO (Universitetet I Oslo) and HKUST (Hong Kong University of Science and Technology) or the structural similarity such as ZIF (Zeolitic Imıdazole

Framework). The combinations of these names are also possible, and the numbers after the names correspond to the order of synthesis, like MIL-53 and MIL-88 [18].

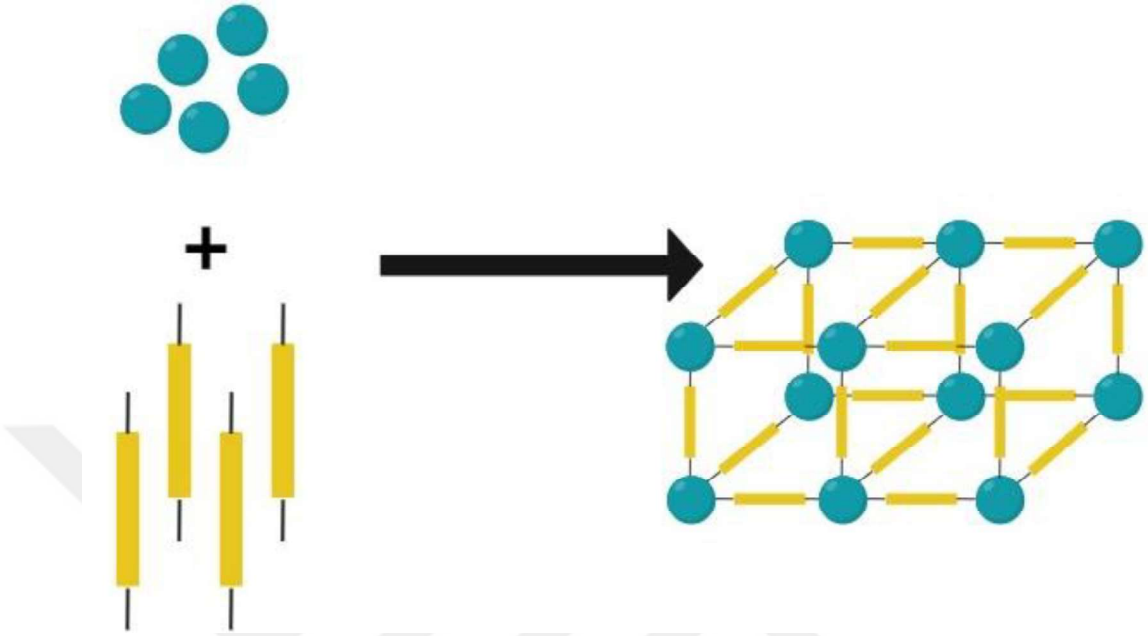

Figure 1.3. Illustration of MOF formation.

1.2.1. Design and synthesis of Metal-Organic Frameworks (MOFs)

MOFs can have many qualities added to them by design and synthesis, such as pore size, electrical and magnetic properties, and catalytic ability by choice of a particular metal node and an organic ligand. The number of binding sites and the possible connection geometry of the metal ion/cluster are crucial fundamental parameters to consider while building the desired MOF. Owing to their partially filled d orbitals, transition metals are frequently used in the synthesis of metal-organic frameworks and exhibit a variety of coordination geometries, including trigonal planar, pyramidal, square planar, tetrahedral, square pyramidal, trigonal bipyramidal, and octahedral [20].

MOFs have been recognized as a significant class of porous compounds due to their distinctive functional and structural characteristics. These structures are made of metal ions, metal ion clusters, and organic linkers that connect them. Choosing the main components for the MOF is another critical factor in the final structure and its characteristics. However, additional synthetic procedures and variables must be considered, including temperature, solvent, pressure, reaction time, and pH [21].

In the sonochemical synthesis method, the term ‘sono’ is used for ultrasound, the energy source used to synthesize MOFs. The solution mixture of the desired MOF is introduced into an ultrasound bath, and ultrasonic waves cause cavity formation in the solution mixture, which leads to physical or chemical changes. Sonication (acoustic cavitation) generates very high temperatures and pressures similar to 5000K and 1000 bar and thus leads to a decrease in crystallization time and particle size [18, 19, 21].

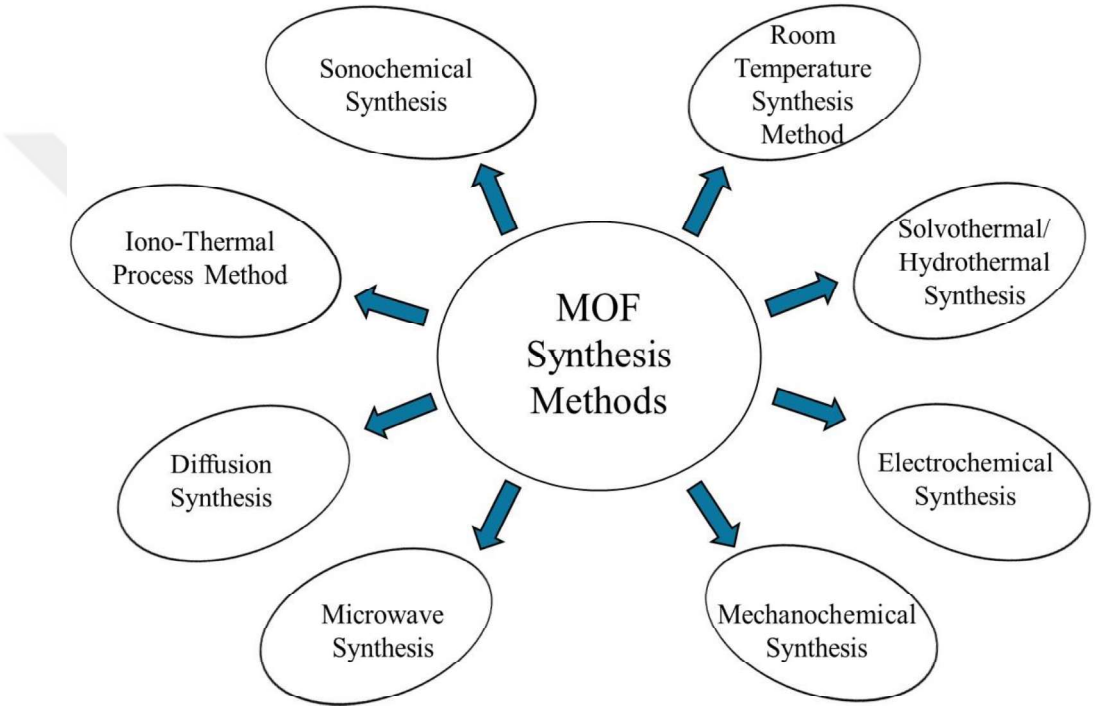

Figure 1.4. Synthesis methods of MOFs.

The room-temperature synthesis method is the most conventional and accessible regarding energy supply. There is no need for an external energy supply, so it occurs at room temperature. The organic linkers and metal precursors are mixed in a solvent and stirred at a fixed temperature. Although this method offers simplicity, the reaction procedure takes longer than other methods due to the low energy usage [21].

The solvothermal/hydrothermal synthesis method involves mixing the metals and organic ligands in a solvent, which can be water, and the name becomes hydrothermal. The mixture is then moved to a Teflon-lined autoclave, which works under pressure above the boiling points of the solvents and a temperature range between 80 and 260 °C. Nevertheless, this method requires a long reaction time to synthesize optimal crystals [18, 19].

MOFs are employed in several applications, and powerful large-scale production methods, such as the electrochemical method, allow us to produce many MOFs using mild conditions and short reaction times. The synthesis includes a reaction tank with an anode, a cathode, and a medium containing metal salt and organic ligands [21].

The mechanochemical synthesis method involves grinding solid substances. There is no need for a solvent during the reaction; the intramolecular bonds break mechanically, and energy consumption decreases. For this reason, this method is considered simple and environmentally friendly. Some situations require a small amount of solvent to mix the solid substances for grinding [18, 19].

The microwave synthesis method is generally used to produce crystals with smaller sizes than those made with conventional heating methods. High temperature helps produce highly crystalline and porous nanostructures at a high speed. The advantage of this method is controlling the size and shape of the particles produced [18, 19].

The diffusion synthesis method can be conducted in three ways: (i) liquid phase, which is the diffusion of metal ions and organic ligands in non-miscible solvents. (ii) gas phase, the solvent is an organic volatile ligand solution, and (iii) gel diffusion, the metal ions and organic ligands dispersed in a gel substance for a time. Although mild conditions were needed for the reaction, the longer reaction times made this method less preferred [19].

The iono-thermal processing method is another easy method that utilizes an ionic liquid medium instead of an organic solvent or water. Ionic liquids are preferred due to their excellent solvation properties, no vapor pressure, and stability. They are also environmentally friendly owing to their recyclability [21].

1.2.2. Factors Affecting MOF Synthesis

MOFs' structure, porosity, crystallinity, and topology depend on several factors besides the metal precursor type and organic linkers utilized. These factors include solvent type, pH conditions, reaction temperature and time, the molar ratio of the reactants, and, in some cases, modulators.

Solvent selection is crucial to producing an MOF. The low solubility of organic ligands hinders the progress of the reactions. To overcome this problem, an organic solvent with a high boiling point is needed. For this reason, organic solvents such as dimethylformamide (DMF), diethyl formamide (DEF), and dimethylsulfoxide (DMSO) are employed in reactions. However, the toxicity of these solvents threatens nature, and researchers are trying to find environmentally friendly solvents [19]. Besides the solubility problem of organic ligands, solvent selection affects the crystal structure of the MOFs. A study investigated the effect of the different solvents by preparing Zn-BTC MOFs with DMF, EtOH, MeOH, isopropanol (IPA), and deionized water (DI). It utilized DMF-only, DMF-MeOH, EtOH-DI, and DMF-IPA-DI solvent groups, and the results demonstrated that different solvents cause different crystal structures [22].

The reaction medium's acidity or basicity significantly impacts MOF development and crystallization. Since metal ion clusters, linkers, and modulators—if any—have an acidic character, MOF synthesis is often conducted at low pH levels. However, at deficient pH levels, organic linkers like imidazolates and 4,4'-bipy cannot bind with metal ions because of protonation. Therefore, they function as limiting reagents. Low pH values can also affect the extent of deprotonation of carboxylate-type ligands, resulting in lower yields and longer reaction durations [23]. Deprotonating chemicals and pH modulators such as sodium hydroxide and trimethylamine accelerate the deprotonation of organic linkers as carboxylates in MOF synthesis [24, 25].

Modulators/additives produce MOFs by controlling their growth, phase, or kinetics. The method adjusts the coordination equilibrium by introducing capping agents with the same chemical functionality as the linkers. Adjusting the coordination contacts between metal ions and organic linkers offers control over the size and shape of the resulting crystals, as well as the rate of framework extension and crystal formation [26]. The particle size and morphological control over HKUST-1, $[Cu_3(1,3,5\text{-btc})_2]_n$, where 1,3,5-btc = 1,3,5-benzenetricarboxylate, further proved the coordinative interaction of modulators with developing MOF crystals. The particle size changed from nanoscale to micron scale when the dodecanoic acid modulator was added in increasing amounts during microwave syntheses in n-butanol. The crystal morphology could also be tuned from octahedron to cuboctahedron to truncated cube to cube [27].

Time and Temperature: In most MOF synthesis techniques, reaction temperature and time are crucial variables. The temperature of the synthesis medium significantly impacts the solubilities of organic linkers, reaction energy barriers, and reaction kinetics.
The temperature affects nucleation and crystal growth rates, which have been used to create nano-size MOFs using a supersaturated crystallization solution. The synthesis of HKUST-1 nanocrystals involved incubating the reaction solution, nucleating at a high temperature, and then cooling the mixture to a low temperature to start the crystal development process [28]. For MOF-5, comparatively slow crystal development and rapid nucleation produced a homogeneous nanocrystal [29]. On the other hand, nucleation persisted at low temperatures in HKUST-1 and coincided with crystal growth. As a result, it was discovered that crystals could grow to a size of 200 nm in under 10 minutes, although SEM pictures and static light scattering tests verified continual new nucleation.

The molar ratio of the reactants plays a crucial role in the synthesis of MOFs, as the stoichiometry of the reactants determines the morphological structure of MOFs [30]. A study investigated the effect of the molar ratio of the reactants on the production of MOF-5. The experiment aimed to determine how the molar ratio of zinc ion to terephthalic acid, reaction temperature, and reaction duration affected the crystal MOF-5's production. By using the molar ratio of the metal ions to the organic ligands of 2:1 at 140°C, the reaction time of 12 hours, the drop acceleration of zinc nitrate at 50 $mL \cdot min^{-1}$, the drop acceleration of terephthalic acid at 40 $mL \cdot min^{-1}$, and the drying temperature at 110°C, the crystal of MOF-5 was synthesized using the parallel flow drop solvothermal method. The results showed that when the molar ratio of metal ions to ligands was increased, the MOF-5 crystals' thermal stability also increased [30].

1.2.3. MOF Applications in MFCs

MOFs are important materials in many different application fields, including drug delivery, biomedicine, batteries, gas adsorption and separation, fuel cells, and many more, because of their unique properties.

For MFC systems, a wide variety of MOFs and related compounds could be employed as catalysts. In order to improve the overall performance of power generation and MFC

degradation, they were frequently utilized as catalytic materials to act on the cathode, anode, and proton exchange membrane (PEM). Microorganisms on the anode caused MFC to produce protons and electrons, which were then transferred to the cathode. Protons and electrons finished the redox reaction with water in the cathode area.

Practical MFC applications were still limited by lower power density and higher cost. The primary elements influencing MFC's overall performance were thought to be microbial propagation and electrode materials. The MFC cathode mainly took both protons and electrons from the anode and used them to perform a cathodic redox reaction with water. MOF composites catalyzed the MFC cathode area. The primary function of MOF composites was to increase the rate at which protons and electrons are transferred and to speed up this process. On the other hand, the composites directly affected the redox reaction process, increasing its rate, encouraging the cathodic reaction to occur, and ultimately boosting the power generation of MFC, which in turn encouraged the degradation of anode microorganisms [31].

According to a study, ZIF-67 grown on NiAl-layered double hydroxide/graphene oxide composite material (NiAl-LDH/GO@ZIF-67) might be utilized as cathode catalysts to increase the power density of MFC to 501.26 mW/m^2 [32]. Another research shows that the power density of an MFC was 587.01 mW/m^2 when two-dimensional material joined by covalent/metal-organic frameworks (COF-300/ZIF-8@Ti_3AlC_2) was utilized as the cathode catalyst [33].

The MFC anode was used for substrate oxidation, electron transfer, loading microorganisms, etc. It has a significant impact on the MFC's ability to generate power. The performance of MFC might be enhanced by using MOFs and their composites as the catalyst-modified anode, which would lower the film impedance and internal resistance of activation, accelerating electron transport and system conductivity. The ability of composite materials to strengthen the MFC anode, enhance microbial adhesion to MFC, and promote pollutant breakdown at the anode was the most crucial factor [31].

The studies showed that MOFs and their derivatives as the MFC anode enhanced anode microbe adherence, decreased system resistance, and accelerated the system's proton-

electron transmission capacity, technology, and enhanced MFC's performance. According to certain research, the anode of MFC made of a composite of ammonia and MIL-53 series MOFs (NH_2-MIL-53(Fe)) decreased electron transfer resistance, enhanced bioelectric catalytic performance, and promoted bacterial adherence on the anode surface. NH_2-MIL-53(Fe)-MFC produced 2.55 W/m^3 of energy [34].

One of the studies demonstrated that the greatest power density of 5.3 ± 0.2 W/m^2 and the coulomb efficiency of 54 ± 4% obtained by MFCs constructed with MOF materials of Fe and Co bimetals (FeCo-MOF/CNFs) anodes [35].

One of the main parts of MFC was the proton exchange membrane, which had two purposes such as transferring the protons and separation of the cathode and anode. The current issues with proton exchange membranes are that the penetration causes damage to the membrane and that reactants and intermediates damage it. Creating new membranes with increased chemical stability was the solution to this issue. The membrane was filled with a variety of inorganic nanomaterials, including silicon dioxide, titanium dioxide, MOFs, etc. These materials have the potential to have high stability, high strength, and other great features, which may help control a variety of penetration problems [31].

Several researches revealed that the proton exchange membrane doped with MOF material may considerably raise the proton conductivity and water absorption of the system while increasing battery power density. A study proved that the UiO-66-NH_2-MOFs composite material was used to create the composite membrane, and it had a proton conductivity of 0.29 S/cm [36].

Further, it has been demonstrated through studies that MIL-53(Al) was utilized as a filler to create the PEM-2 composite membrane and the results demonstrated that the water absorption and proton conductivity of the composite membrane were increased by 2.1 times, and 92% power density was achieved [37].

2. SCOPE OF THE THESIS

Metal-organic frameworks (MOFs) are highly porous materials from metal ions or clusters and organic linkers. Their distinctive properties include high surface area, high porosity, highly stable form, and pore size tunability, making them selective in several applications. Besides the spotlighted in this thesis, MOFs are applied in catalysis, fuel cells, energy storage, gas adsorption, drug delivery, and biomedicine. In this study, copper (Cu), nickel (Ni), iron (Fe), and cobalt (Co) MOFs are synthesized due to their abundance and cost-effectiveness. The effect of metal ion precursor type and second metal addition to produced MOFs and solvent selection is examined. 1,3,5-Benzenetricarboxylic acid (H_3BTC) was used as an organic linker due to the synthesis route, solvent usage, and conditions being favorable. This study aims to examine the single-metal and bimetallic MOFs synthesized from Cu, Ni, Fe, and Co application in Microbial Fuel Cell (MFC) cathode catalysts. The MOFs are used in the coating slurries prepared with carbon black and polyvinyl alcohol (PVA). The coating slurries are then coated on stainless-steel meshes. The performance of cathodes prepared with synthesized MOFs is evaluated in MFCs as oxygen reduction reaction (ORR) catalysts.

In Chapter 1, metal-organic frameworks (MOFs) are presented by discussing different design concepts, synthesis methods, and MOF synthesis-affecting factors. The application areas of MOFs expressed and MFC application examples in the literature demonstrated. Chapter 2 explained the aim of this thesis study and summarized it. Chapter 3 includes the MOF synthesis procedure, preparation of coating materials, information on prepared anode and cathode materials, and the characterization methods utilized throughout the study. In Chapter 4, the results of the study are shown and discussed. Synthesized MOFs were characterized by X-ray diffraction Analysis (XRD), Scanning Electron Microscopy (SEM), and X-ray photoelectron Spectroscopy (XPS). Chronopotentiometry and cyclic voltammetry (CV) analyzed the electrochemical properties of the prepared stainless-steel mesh electrodes. The selected electrodes were used to construct microbial fuel cells, and their performance analyses were done by Open circuit analysis (OCV), linear sweep voltammetry (LSV), and electrochemical impedance spectroscopy (EIS). Chapter 5 concludes this thesis study, and Chapter 6 finishes the thesis with possible future works.

3. EXPERIMENTAL

3.1. Materials

Cupric acetate dihydrate, nickel (II) nitrate nonahydrate, nickel (II) acetate-4-hydrate, nickel (II) nitrate hexahydrate (98%, Alfa Aesar), cobalt (II) nitrate hexahydrate (98%, Alfa Aesar), iron (III) nitrate nonahydrate, 1,3,5-benzene tricarboxylic acid, polyvinyl alcohol (Fluka Chemie), ultra-pure water (Millipore, Milli-Q), ethanol (absolute, Merck), DMF (Chem-Lab), ammonia, Carbon Black Vulcan CX-72 (Fuel Cell Earth LLC), disodium phosphate and potassium dihydrogen phosphate were used in synthesis and experiments. The sonochemical synthesis of MOFs and preparation of carbon coatings were performed using a Mercury Ultrasonic Cleaner at 40 kHz. Carbon coatings were prepared to coat stainless steel mesh collectors (stainless steel mesh 50, 304 grade) with carbon black, binder, and MOFs. The MOF synthesis experiments included the use of a drying oven (BINDER GmbH) and Domel Centric 260 R for centrifugation. For drying the coated SSM heat gun (Steinel HL 2010 E) is used. GAMRY Interface Potentiostat was used to evaluate the electrochemical properties of prepared SSM.

3.2. Synthesis of Metal-Organic Frameworks (MOFs)

Cu, Ni, Fe, Co, and bimetallic MOFs are synthesized from metal salts and organic ligands, H_3BTC, at different temperatures, and the Sonochemical synthesis method. The syntheses were classified into two groups based on the solvent used. The DMF solvent was used to synthesize FeBTC according to the literature [38], and CoBTC and FeCoBTC were synthesized following the literature with some modifications. NH_3 solvent is used to dissolve H_3BTC since EtOH is insufficient to dissolve it. In [39], distilled water and ethanol were used to dissolve the metal precursor and H_3BTC, respectively. Using DMF solvent to synthesize CuBTC, NiBTC, and CuNiBTC is tried applying a similar process in the literature [38].

3.2.1. Dimethylformamide (DMF) Solvent

3.2.1.1. FeBTC. 10 mmol iron (III) nitrate nonahydrate and 10 mmol 1,3,5-Benzenetricarboxylic acid were dissolved in 30 mL DMF separately. Two solutions were mixed onto a magnetic stirrer and then placed in the US generator at 60°C 40 kHz. After 1 hour of reaction time, a brown gel-like product was collected. The product was dried at 90°C for 12h.

3.2.1.2. CoBTC. 10 mmol cobalt (II) nitrate hexahydrate and 10 mmol 1,3,5-Benzenetricarboxylic acid were dissolved in 30 mL DMF separately. Two solutions were mixed onto a magnetic stirrer and then placed in the US generator at 60°C 40 kHz. After 6 hours of reaction time, the purple-colored precipitate was collected. The product was dried at 90°C for 12h.



Figure 3.1.Pictures of the synthesized MOFs, (a) FeBTC, (b) CoBTC, (c) FeCoBTC, (d) CuBTC, (e) NiBTC, and (f) CuNiBTC respectively.

3.2.1.3. FeCoBTC. 5 mmol iron (III) nitrate nonahydrate and 5 mmol cobalt (II) nitrate hexahydrate were dissolved in 30 mL DMF separately. In another container, 10 mmol of 1,3,5-Benzenetricarboxylic acid was dissolved. First, metal solutions were mixed, and then an organic linker solution was added. Two solutions were mixed onto a magnetic stirrer and

then placed in the US generator at 60°C 40 kHz. After 1 hour of reaction time, a brown-purple-colored gel-like product was collected. The product was dried at 90°C for 12h.

3.2.1.4. CuBTC. 10 mmol copper acetate and 10 mmol H3BTC were dissolved in 30 mL DMF separately. The two solutions were mixed into a magnetic stirrer, and the test tube was fixed in the US generator at 60°C 40 kHz. After 2h of reaction time, blue-colored precipitates were collected and dried at 90°C for 12h.

3.2.1.5. NiBTC. 10 mmol Nickel (II) acetate-4-hydrate and 10 mmol H_3BTC were dissolved in 30 mL DMF separately. Two solutions were mixed onto a magnetic stirrer and the test tube was fixed in the US generator at 60°C 40 kHz. After 2h of reaction time blue colored precipitates were collected and dried at 90°C for 12h.

3.2.1.6. NiCuBTC. 5 mmol copper acetate and 5 mmol nickel (II) acetate-4-hydrate were dissolved in 10 3 mL DMF and mixed onto a magnetic stirrer. Two metal solutions were mixed, and an organic linker solution prepared by 10 mmol H3BTC was dissolved in 30 mL DMF. Two solutions were mixed onto a magnetic stirrer, and the test tube was fixed in the US generator at 60°C 40 kHz. After 2h of reaction time, blue-colored precipitates were collected and dried at 90°C for 12h. Pictures of the synthesized MOFs are shown in Figure 3.1.

3.2.2. Ammonia (NH_3) Solvent

3.2.2.1. CuBTC. 5 mmol 1,3,5-Benzenetricarboxylic acid was dissolved in 6 mL of 2M NH_3 solution. 5 mmol metal salt Cupper acetate was dissolved in 3 mL deionized water. Two solutions were mixed onto a magnetic stirrer and the test tube was fixed in the US generator at 60°C 40 kHz. After 4h of reaction time, pale blue colored precipitates were collected and dried at 90°C for 12 h.

3.2.2.2. NiBTC. 5 mmol 1,3,5-Benzenetricarboxylic acid was dissolved in 6 mL of 2M NH_3 solution. 5 mmol Nickel (III) Nitrate hexahydrate was dissolved in 3 mL deionized water, and the two solutions were mixed into a magnetic stirrer. Then, the test tube was fixed in the

US generator at 60°C 40 kHz. After 4h of reaction time, pale green-colored precipitates were collected and dried at 90°C for 12h.

3.2.2.3. NiCuBTC. 10 mmol 1,3,5-Benzenetricarboxylic acid was dissolved in 6 mL of 2M NH_3 solution. 5 mmol of Cupper acetate and 5 mmol of Nickel hexahydrate were dissolved in 3 mL deionized water separately. Two metal solutions were mixed onto a magnetic stirrer and the mixture was added to the organic linker solution. The test tube was fixed in the US generator at 60°C 40 kHz. After 4h of reaction time, precipitates were collected and dried at 90°C for 12 h. Pictures of the synthesized MOFs are shown in Figure 3.2.



Figure 3.2. Pictures of the synthesized MOFs, (a) CuBTC, (b) NiBTC, and (c) CuNiBTC respectively.

3.3.Preparation of Coated Stainless-Steel Mesh (SSM) Electrodes

Stainless steel meshes are cut into and washed with ethanol, acetone, and water respectively, and dried. All meshes have the same thickness of 0.35 mm. Coatings are prepared from different constituents for anode and cathodes. The anode material is prepared from carbon black and polyvinyl alcohol (PVA) binder. Cathode materials are prepared from carbon black/MOF composite and PVA binder. PVA binder is prepared 10% by weight with dissolving PVA in distilled water at 60°C and 350 rpm on the magnetic stirrer.

3.3.1. SSM Electrodes Coated for Anode

Coatings are prepared with 90% CB and 10% PVA binder. SSM#1: A slurry containing 90 mg of CB was ready with 90% CB and 10% PVA by weight. 90 mg CB was dispersed in

1 mL EtOH on the stirrer. Then, 100 mg PVA solution and 10 drops of EtOH were added and stirred for 40 minutes. The mixture was placed in a US bath for 40 minutes. The coating was coated on the SSM and dried at RT for a day.

3.3.2. SSM Electrodes Coated with MOF-CB for Cathode

All the MOF-CB composite-coated SSM electrodes were prepared by stirring 80% MOF, 10 % CB, and 10% PVA in 1 mL of EtOH on the stirrer. Firstly, the CB-MOF mixture was dissolved in EtOH, and PVA was added. After the stirring process, a US bath was utilized to obtain a more dense structure, and prepared slurries were coated on SSMs from number 2 to number 10. The following table shows the DMF solvent synthesis of MOFs and their corresponding SSM numbers.

Table 3.1. SSM numbers of DMF solvent synthesis MOFs.

SSM #2	CoBTC
SSM #3	FeBTC
SSM #4	FeCoBTC
SSM #5	CuBTC
SSM #6	NiBTC
SSM #7	CuNiBTC

The following table shows the NH_3 solvent synthesis MOFs and their corresponding SSM numbers.

Table 3.2.SSM numbers of NH_3 solvent synthesis MOFs.

SSM #8	CuBTC
SSM #9	NiBTC
SSM #10	CuNiBTC

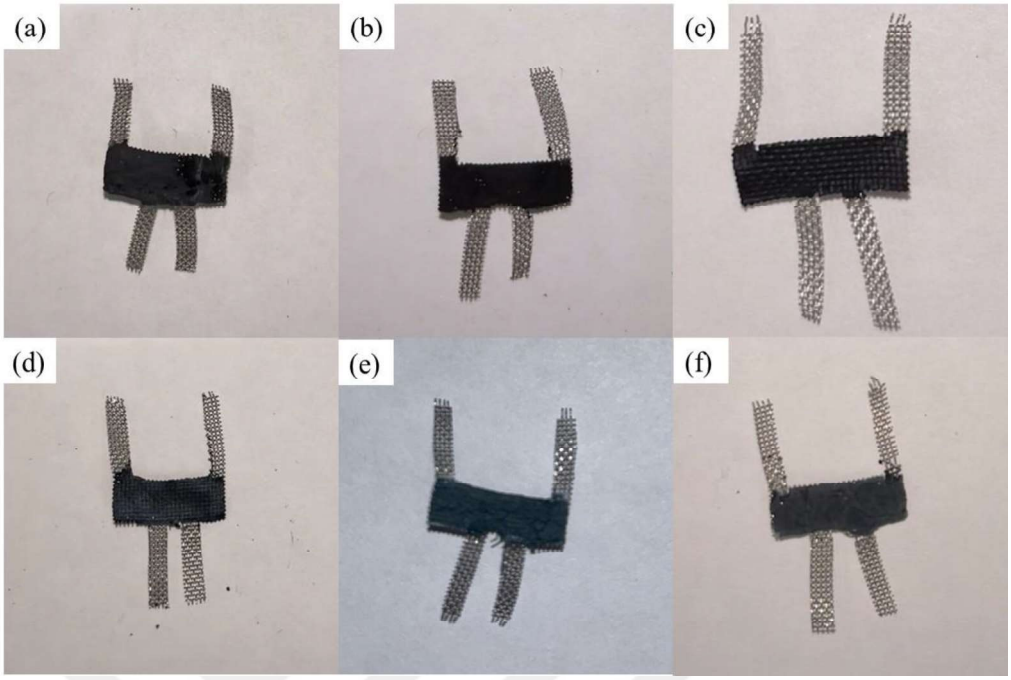

Figure 3.3. a) CoBTC, b) FeBTC, c) FeCoBTC, d) CuBTC, e) NiBTC and f) CuNiBTC.

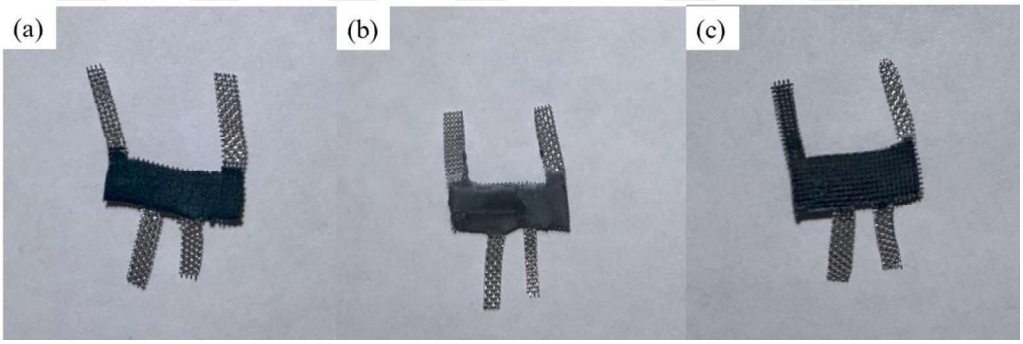

Figure 3.4. a) CuBTC, b) NiBTC, and c) CuNiBTC.

3.4. Setup of MFC and Bacterial Inoculation

Bacterial inoculum was performed at the Boğaziçi University Department of Molecular Biology and Genetics and E-Coli bacteria was used. The Miller Hinten agar plate was used to resurrect the frozen stock of bacteria cells. Then, one of the colonies was taken, and bacteria were cultured in 10 mL of LB medium at 37 °C in an incubator. After 24h incubation, samples were used for electrochemical measurements. The UV Spectroscopy was used to determine the OD_{600} value. When the value is between 0.5 - 0.8 nm, the sample was ready to use.



Figure 3.5. Images of constructed MFC on operation.

The two-chamber reactor was constructed using plexiglass, according to a previous study [40]. The reason for choosing plexiglass material is to autoclave the materials. Two chambers were separated by using a Nafion membrane. There are holes in the plexiglass that are used to inject bacteria, immersion cathode electrodes, and give off oxygen and nitrogen gases. The anode electrode was prepared by coating the stainless steel mesh with carbon black and PVA binder. The SSM has a 0.35 mm thickness, and the width and height were adjusted to fit in the plexiglass chamber. The cathode electrodes were prepared by coating stainless-steel mesh using carbon black, PVA, and synthesized metal-organic frameworks. Figure 3.5 demonstrates the operation of the bacteria-inoculated fuel cell. The left-hand side is the anode compartment which contains E-Coli and nitrogen gas was given off. The right-hand side is the cathode compartment contains a cathode electrode prepared by MOF-CB composites.

3.5.Characterization Methods

XRD, SEM, and XPS analysis characterize the crystal structure, porosity, and elemental analysis of synthesized MOFs. The electrochemical properties of prepared meshes are evaluated with chronopotentiometry and cyclic voltammetry (CV). The performance

analysis of the prepared cells is evaluated with open circuit voltage (OCV), linear sweep voltammetry (LSV), and electrochemical impedance spectroscopy (EIS).

3.5.1. X-Ray Diffraction Analysis (XRD)

X-ray diffraction (XRD) is used to characterize the crystal structure, phase purity, and crystallinity of synthesized MOFs. These analyses involve directing X-rays at a material and measuring the distance between lattice planes. As X-rays enter the material, the electron clouds surrounding the atom cause scattering. By applying Bragg's Law, distances between lattice planes can be calculated [41, 42]. Bragg's Law is expressed as

$$n\lambda = 2dsin\theta \tag{3.1}$$

where n is the diffraction order (an integer), λ is the wavelength of the radiation, d is the spacing between lattice planes and θ is the angle between the incident beam of radiation and lattice planes [41]. XRD analyses of synthesized MOFs are collected with Rigaku D/MAX-Ultima+/PC Diffractometer with Cu-Kα radiation (λ=1.54 Å) in the XRD Facility of BU Advanced Technologies R&D Center.

3.5.1. Scanning Electron Microscopy (SEM)

Scanning electron microscope (SEM) is a technique employed to study the topography of materials. SEM analysis relies on the interaction between the electron beam and the material. When the electron beam is directed onto the sample, electrons interact with the material and scatter in various ways. Inelastically scattered electrons, known as secondary electrons provide information about the surface morphology while elastically scattered electrons, known as backscattered electrons provide information about the elemental structure [43]. SEM images of MOFs are collected via Thermoscientific Quattro S in Boğaziçi University Center for Life Sciences & Technologies.

3.5.2. X-Ray Photoelectron Spectroscopy (XPS)

X-ray photoelectron spectroscopy (XPS) is another characterization method employed in qualitative analysis. It enables the determination of surface composition and the chemical states of the surface elements [44]. XPS spectra are collected using the Thermo Scientific K-

Alpha X-ray Photoelectron Spectrometer at Bogazici University Advanced Technologies R&D Center.

3.5.4. Chronopotentiometry

The first electrochemical analysis technique applied to the stainless steel meshes is chronopotentiometry. This analysis was utilized to measure the four-probe conductivity of meshes. Chronopotentiometry provides information such as open circuit potential and solution resistance or resistance across the surface of a material. Currents ranging from 0.1 A - 0.2 A and 1A - 2A were applied and voltage responses over time were monitored and recorded using GAMRY Interface Potentiostat to evaluate the conductivities of the meshes. Working and counter leads apply the current while working sense and reference leads measure the voltage. The voltage across the inner probes is obtained through current flow between the outer probes. All probes are positioned at equal spacings throughout the mesh.

The following figure illustrates an example of a resulting graph from a chronopotentiometry measurement conducted at 0.1 – 0.2 A on a bare mesh.

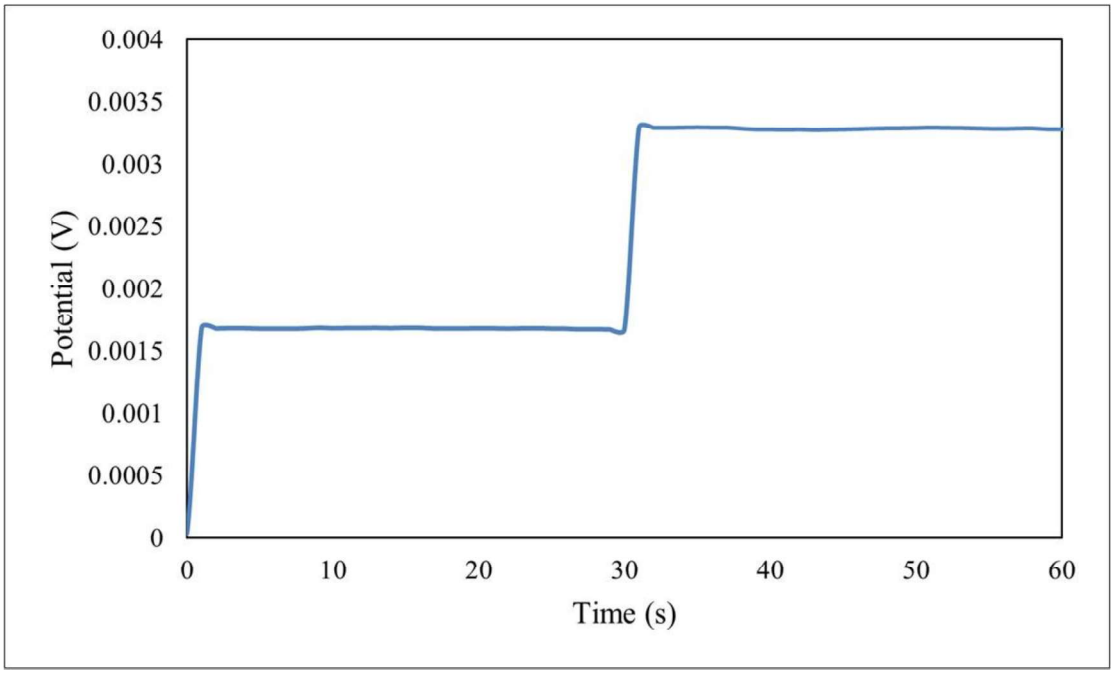

Figure 3.6. Chronopotentiometry resulting graph for an example sample.

3.5.5. Electrochemical Impedance Spectroscopy (EIS)

Electrochemical impedance spectroscopy (EIS) is a technique used to measure the internal resistance of an electrochemical cell. It can help characterize the performance of it. Internal resistance is composed of different components such as electrolyte resistance, electrode resistance, and charge transfer resistance in the cell, and measuring EIS measurements helps discover the contribution of each component [45]. EIS is generally conducted by applying alternating current (AC) voltage and taking the current response through the cell [46]. EIS analysis was performed using GAMRY Interface Potentiostat and an AC Voltage of 10 mV rms was applied between, an initial frequency (Hz) of 10000 and a final frequency of 0.1.

3.5.6. Cyclic Voltammetry (CV)

Cyclic voltammetry is a technique utilized to determine the redox properties of an electrochemical cell. CV provides details about the electron transfer mechanisms occurring during redox reactions [47, 48] CV measurements were conducted using a three-electrode system which consists of counter, working, and reference electrodes. The reference electrode was Ag/AgCl, the counter electrode was Pt wire, the working electrode was the corresponding SSM, and all electrodes were placed at equal distances. The electrolyte was a phosphate buffer solution (PBS) with a pH of 7. (PBS was prepared from the stock solutions of 0.2 M Na_2HPO_4 and KH_2PO_4). GAMRY Interface Potentiostat was employed to apply a voltage between scan limits of 0.8 V to -0.8 V. To determine the effect of scan rate, 50 mV/s, and 100 mV/s under N_2, O_2, and no gas environments.

3.5.7. Open Circuit Voltage Analysis (OCV)

Open circuit voltage (OCV) is the potential of a cell in an open circuit as implied by its name. During measurements, there is no external load on the cell i.e. the cell experiences no flow of current. Open circuit potential varies based on the charges surrounding the electrodes and provides information on the net current direction during the oxidation-reduction reactions. OCV also provides information on the highest possible cell voltage and the difference between anodic and cathodic open circuit potentials [49, 50].

3.5.8. Linear Sweep Voltammetry (LSV)

Linear sweep voltammetry (LSV) is the technique used to calculate a cell's maximum power density and current density. The working electrode is scanned while the voltage between an initial and a final potential is applied. The current response is then monitored. The current response gives a peak or dip when there is an oxidation or reduction of the species [51]. LSV measurements were conducted at a scan rate of 20 mV/s, utilizing GAMRY potentiostat with a two-electrode system. The two-electrode system was constructed by connecting the working sense and working leads and the reference lead, counter sense, and counter leads. The working electrode section was connected to the anode, while the reference section was connected to the cathode. The current response data were normalized to the cathode surface area.

4. RESULTS AND DISCUSSION

All structural and chemical analyses of MOFs were completed by using XRD, SEM, and XPS for crystallography, morphology, and oxidation state, respectively.

4.1.Characterization of MOFs

The MOFs were categorized according to the solvent utilized to dissolve organic linker molecules. The first group of MOFs was produced by using DMF solvent. Metal salts were also dissolved in DMF solvent. The second group of MOFs was produced by dissolving the organic linker in an ammonia solution. In the second case, metal salts were dissolved in distilled water.

4.1.1. MOFs Synthesized by Using DMF Solvent

4.1.1.1.FeBTC. The SEM images of the FeBTC at different zoom levels were demonstrated in Figure 4.1. The metal salt Fe(NO3)3.9H2O and the organic linker H3BTC were dissolved in DMF for the synthesis. SEM images demonstrate the shapes like agglomerated particles. This MOF shows a low degree of crystal structure as shown in previous literature [52, 53].

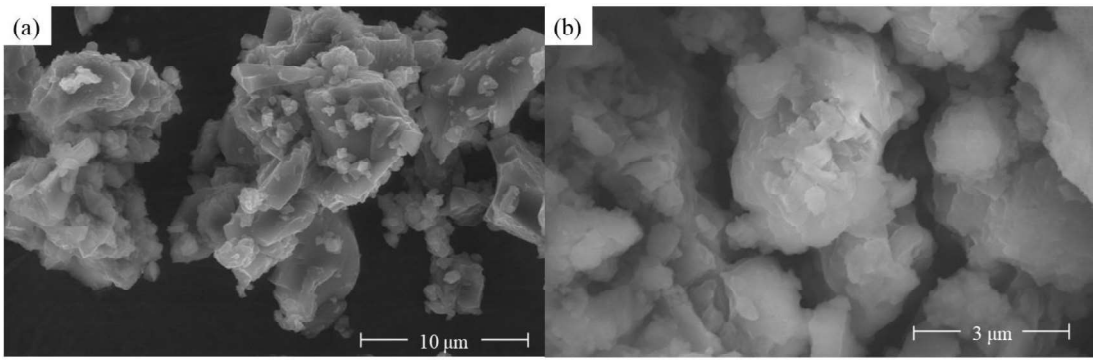

Figure 4.1. SEM images of FeBTC at a) 6000x, b) 25000x zoom level.

Figure 4.2 shows the XRD peaks of the FeBTC MOF. The resulting spectrum exhibits broad and overlay peaks. The XRD spectrum is evidence of the semi-amorphous structure

of the MOF. The reason for this kind of peak is the disordered structure of the small-sized crystals, which is very similar to the literature [54].

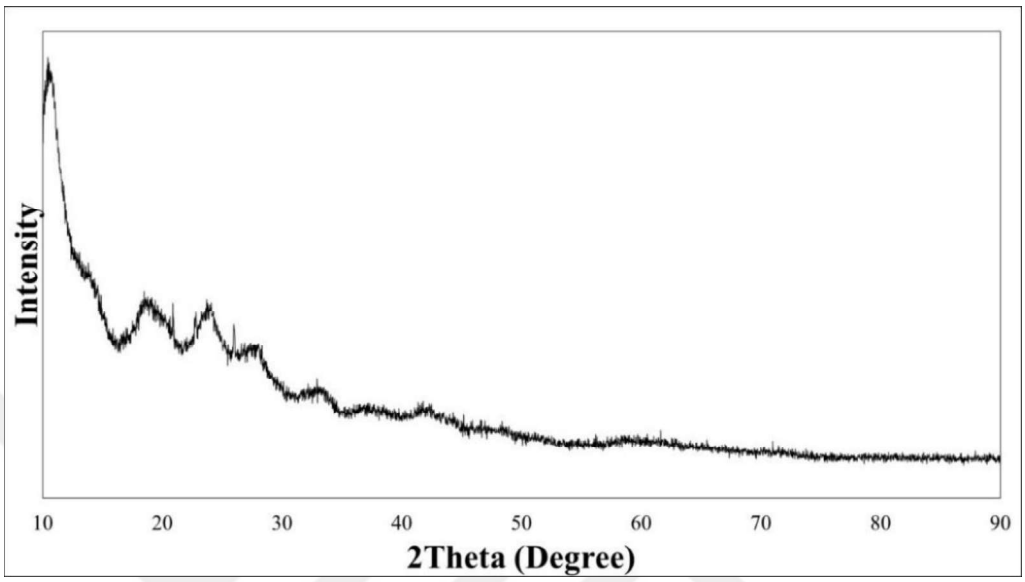

Figure 4.2.XRD pattern of FeBTC.

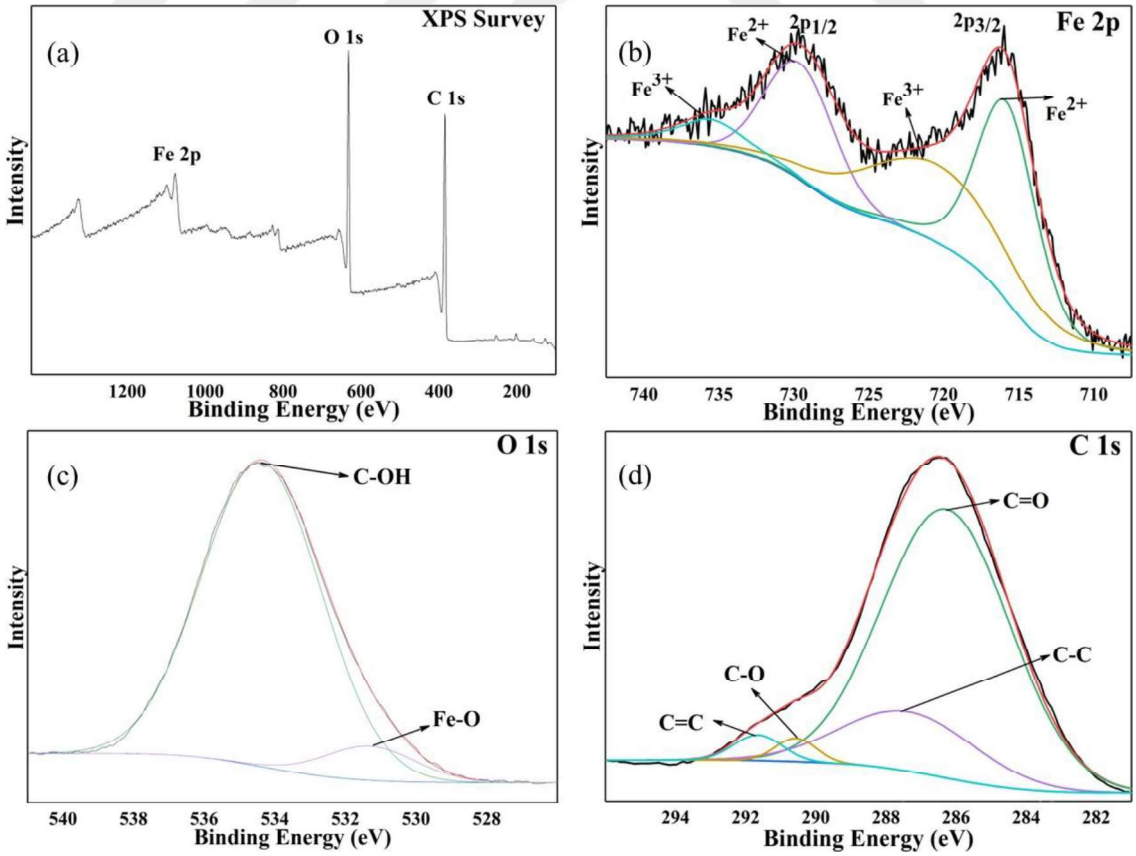

Figure 4.3. XPS pattern of FeBTC deconvoluted data a) XPS survey, b) Fe2p, c) O1s, and d) C1s.

XPS spectra of FeBTC MOF were demonstrated in Figure 4.3. XPS survey analysis was done, and the Fe 2p, O 1s, and C 1s peaks were given in (a). Deconvoluted spectra of Fe 2p, O1s, and C 1s were given in (b), (c) and (d) respectively. In the Fe 2p spectrum, the peaks were observed at the binding energies of 713.6 eV, 718.9 eV, 727.51 eV, and 733.08 eV and the binding energies were attributed to $2p_{3/2}$, the satellite peak of $2p_{3/2}$, $2p_{1/2}$ and the satellite peak of $2p_{1/2}$ respectively [55]. O1s spectra show peaks at 530.22 eV and 533.37 eV and they were assigned to C-OH and Fe-O bonds respectively [56]. At C 1s spectrum, the peaks were observed at 284.6 eV, 285.2 eV, 286.3 eV, and 289.4 eV. In the literature, the first peak corresponds to sp^2 hybridized carbon which could be a C=O bond, the second bond is sp^3 hybridized carbon (C-C bond), the third peak is a C-O bond and the last one is for C=C bond. [56].

4.1.1.2. CoBTC. The SEM images of the CoBTC at different zoom levels were demonstrated in Figure 4.4. The metal salt $Co(NO_3)_2.6H_2O$ and the organic linker H_3BTC were dissolved in DMF for the synthesis. CoBTC seems to have an uneven structure. According to the publications examined, the morphology of CoBTC varies based on the synthesis process employed and its modifications. CoBTC can have the shape of a rod or a distorted octahedral form. The resulting CoBTC tends to agglomerate and has an uneven size distribution. The synthesized CoBTC has a cubical form with six unevenly conditioned surfaces [57].

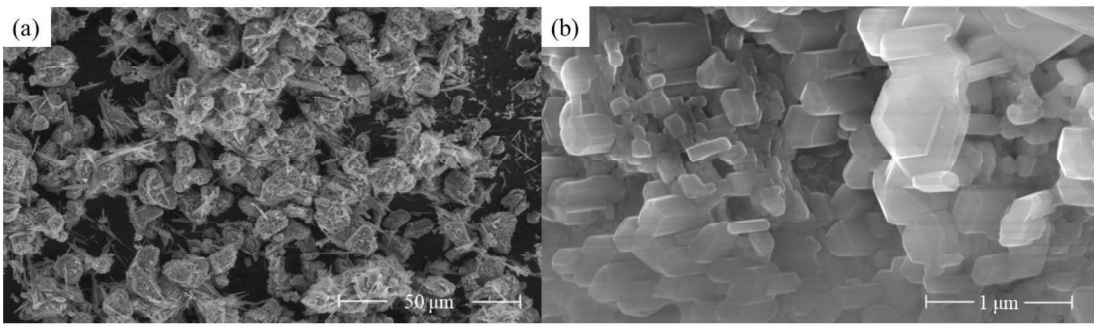

Figure 4.4. SEM images of CoBTC at a) 1000x, b) 60000x zoom level.

XRD pattern for CoBTC MOF shows distinctive peaks which are signs of crystal structure. There are two highest peaks at around 10-20 degrees and around 25 degrees. These peaks resemble the simulated peaks given in the literature [58, 59]. The XRD results are proof that the synthesized MOF was consistent with the literature. Therefore, Co-BTC synthesis was completed successfully.

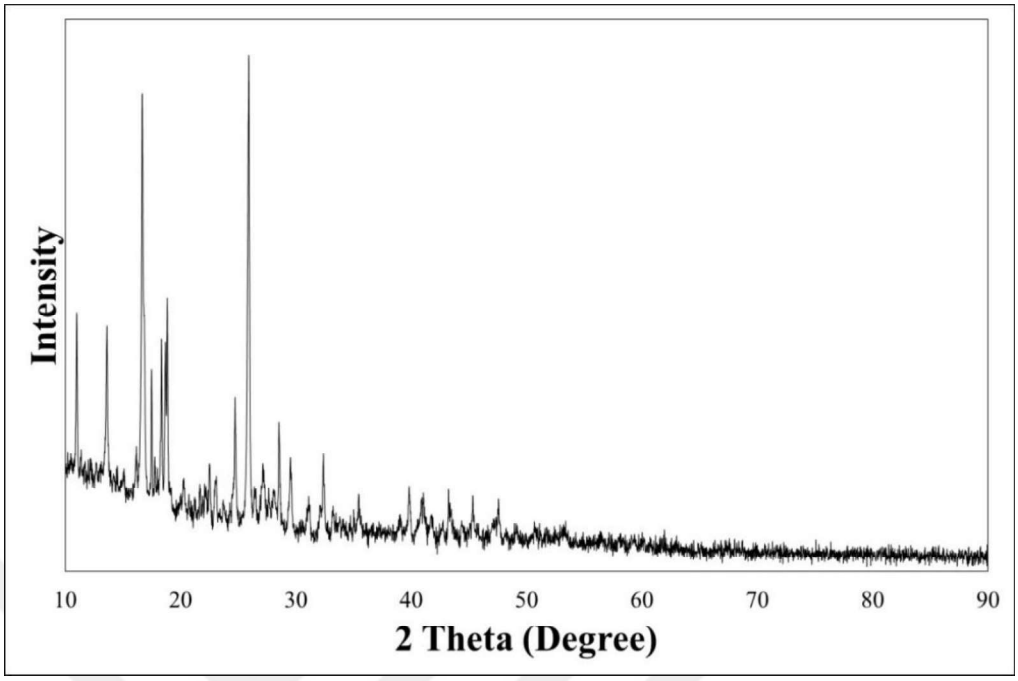

Figure 4.5. XRD pattern of CoBTC.

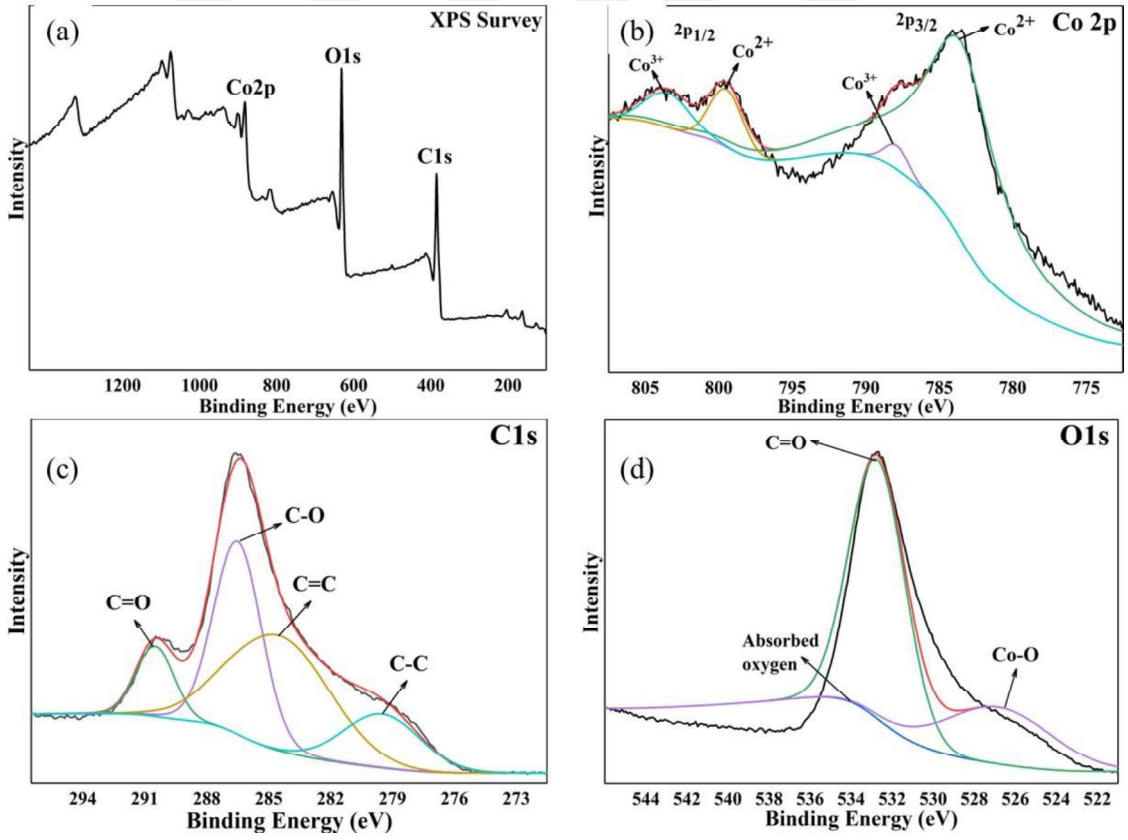

Figure 4.6. XPS pattern of CoBTC deconvoluted data a) XPS survey, b) Co2p, c) O1s, and d) C1s.

XPS spectra for CoBTC MOF were demonstrated in Figure 4.6. XPS survey analysis was done and the peaks for Co 2p, O 1s, and C 1s were given in (a). Deconvoluted spectra of Co 2p, O1s, and C 1s were given in (b), (c) and (d) respectively. At the spectra (b) the binding energies at 781.55 eV, 785.52 eV, 797.1 eV, and 801.18 eV binding energies were attributed to Co^{2+} ($2p_{3/2}$), Co^{3+} ($2p_{3/2}$), Co^{2+} ($2p_{1/2}$) and Co^{3+} ($2p_{1/2}$) respectively [58]. O1s spectra show peaks at 531.8 eV, 525.6, and 532.9 which were assigned to C=O, Co-O bonds, and absorbed oxygen respectively [60]. At the C1s spectrum, the peaks were observed at 278 eV, 283.1 eV, 285.08 eV, and 289 eV. These peaks were assigned to C-C, C=C, C-O, and C=O bonds respectively [58]. The SEM, XRD, and XPS results are consistent that Co-BTC MOF obtained successfully.

4.1.1.3. FeCoBTC. The SEM images of the FeCoBTC at different zoom levels were demonstrated in Figure 4.7. The metal salts Fe(NO3)3.9H2O, Co(NO3)2.6H2O, and the organic linker H3BTC were dissolved in DMF for the synthesis. SEM images provided insight into the shape and microstructure of the as-prepared FeCoBTC MOF particles. Figure 4.7 shows the layered structure of the FeCoBTC, which increased the catalytic reaction's mass and electricity transfer area. A characteristic porous structural pattern is seen, as shown in Figure 4.7. (b) [61]

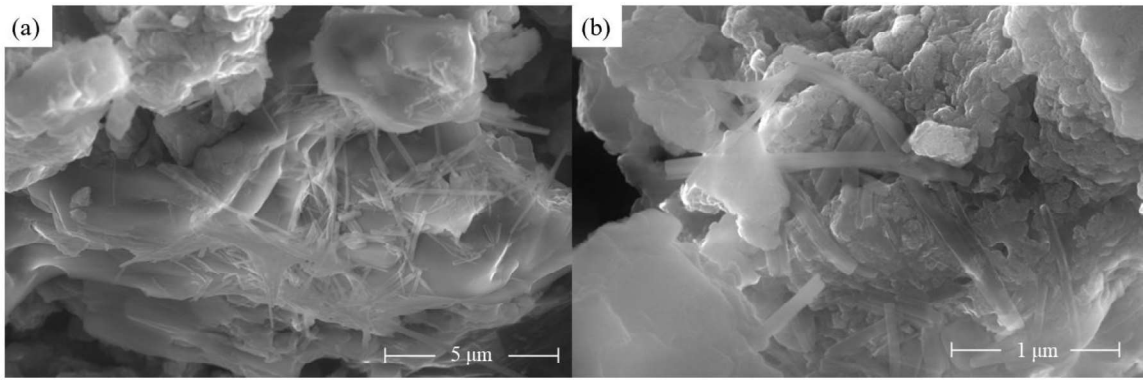

Figure 4.7. SEM images of FeCoBTC at a) 12000x, b) 50000x zoom level.

Comparing the FeCoBTC MOF with the FeBTC and the CoBTC validates its crystallographic and physical characteristics. The FeCoBTC exhibits a few characteristic peaks of the FeBTC and the CoBTC, demonstrating the FeCoBTC MOF's successful synthesis [61].

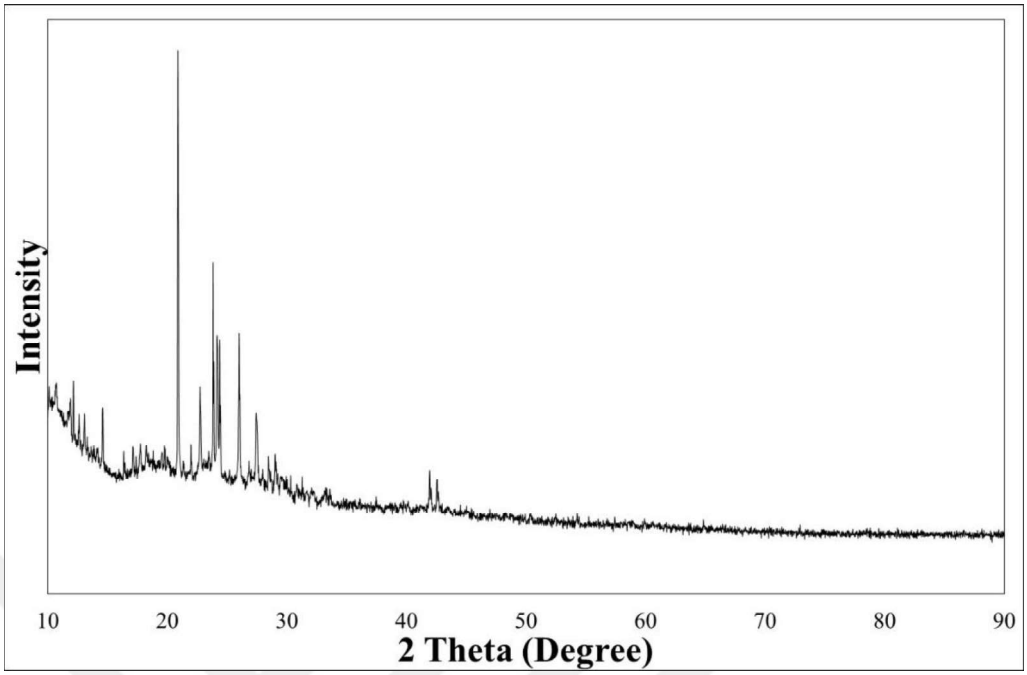

Figure 4.8. XRD pattern of FeCoBTC.

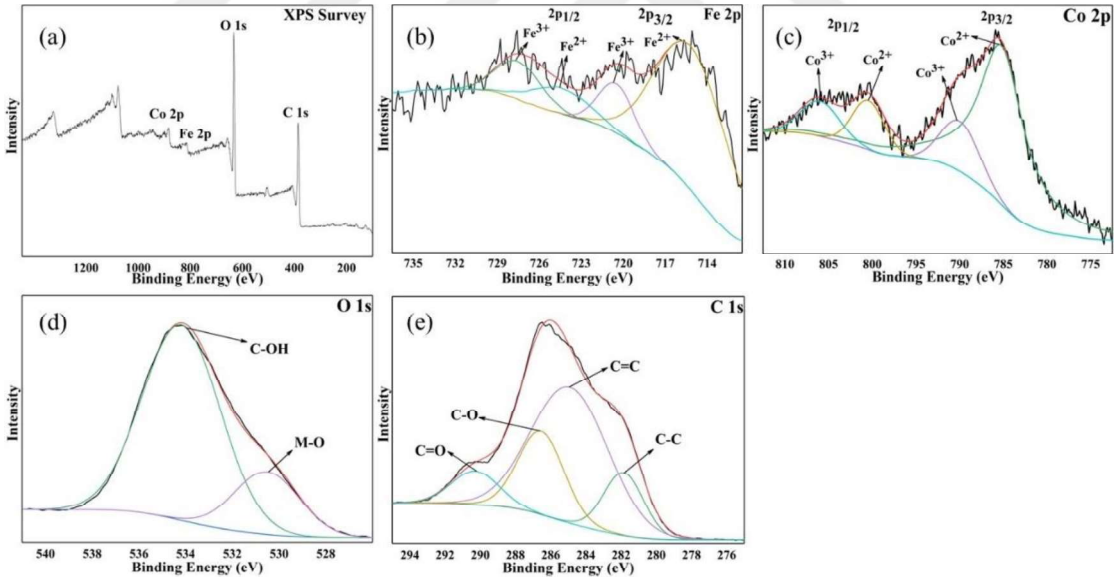

Figure 4.9. XPS pattern of FeCoBTC deconvoluted data a) XPS survey, b) Co2p, c) Fe2p, d) O1s, and e) C 1s.

XPS survey analysis revealed the presence of C, O, Fe, and Co components and provided information about the surface condition and composition of the FeCoBTC MOF. The peaks at 281.87, 285.03, and 286.52 eV in the high-resolution spectra of C 1s are ascribed to C-C, C=C, and C─O, respectively. Moreover, the signal at 290.21 eV is linked to O─C=O, indicating that the FeCoBTC had a functional group that contained oxygen that

was derived from H_3BTC. The binding energies of 529.56 and 533.25 eV, respectively, are associated with the distinctive peaks of O-Fe/Co and O─H, as the O1s spectrum demonstrates. The high-resolution curves of the Fe 2p spectra show two peaks with binding energies of 714.24 and 723.06 eV, respectively, that are associated with Fe^{3+} $2p_{3/2}$ and Fe^{3+} $2p_{1/2}$ of the FeCoBTC. The distinctive peaks of Fe^{3+} $2p_{3/2}$ Sat. and Fe^{3+} $2p_{1/2}$ Sat. are responsible for binding energies of 719.22 and 726.36 eV, respectively. The peaks in the Co 2p spectrum are attributed to Co^{3+} $2p_{3/2}$ and Co^{3+} $2p_{1/2}$, respectively, at 782.9 and 798.1 eV. Co^{2+} $2p_{3/2}$ and Co^{2+} $2p_{1/2}$ are responsible for the two peaks at 787.9 and 803.74 eV [61].

4.1.1.4.CuBTC. The SEM images of the CuBTC at different zoom levels were demonstrated in Figure 4.10. The metal salt $Cu(OAc)_2$ and the organic linker H_3BTC were dissolved in DMF for the synthesis. A smooth surface and typical hexagonal shape of the crystal are displayed in the CuBTC SEM picture shown in Figure 4.10 [60].

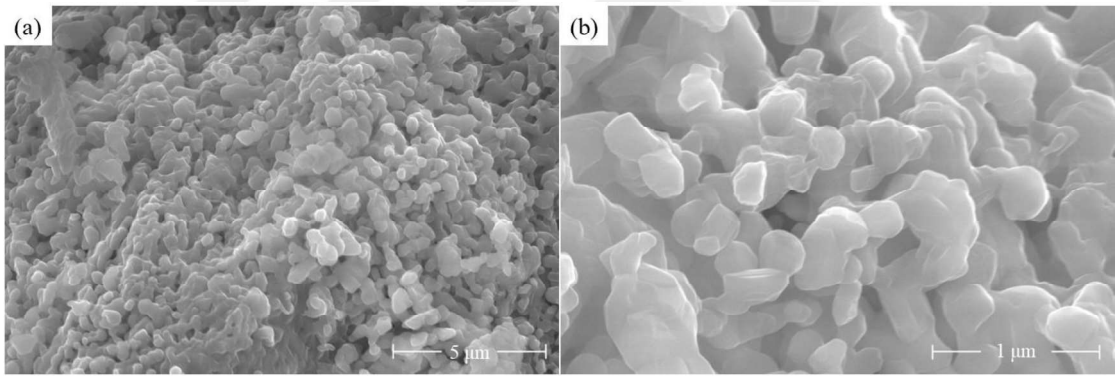

Figure 4.10. SEM images of CuBTC at a) 12000x, b) 50000x zoom level.

Powder X-ray diffraction was used to assess the crystallinity of the synthesized CuBTC MOF. Figure 4.11 illustrates the XRD pattern of the synthesized CuBTC matches with the literature. The positions and features have a unique peak at 2θ, suggesting that the products are pure phases and crystalline [62].

At 281.22, 284.21, 285.86 eV, and 289.95 eV, the XPS peak of C 1s can be seen. The carbon bonds corresponding to these peaks are C-C, C=C, C-O, and C=O respectively. O1s has binding energies of 532.87 eV and 530.06 eV which come from the bonds C-OH and O-Cu. The peaks corresponding to Cu $2p_{3/2}$ and Cu $2p_{1/2}$ have binding energies of 933.9 eV and

955.6 eV, respectively. Binding energies of 939.51 and 944.05 eV, are associated with the satellite peaks of Cu $2p_{3/2}$ and Cu $2p_{1/2}$ [63].

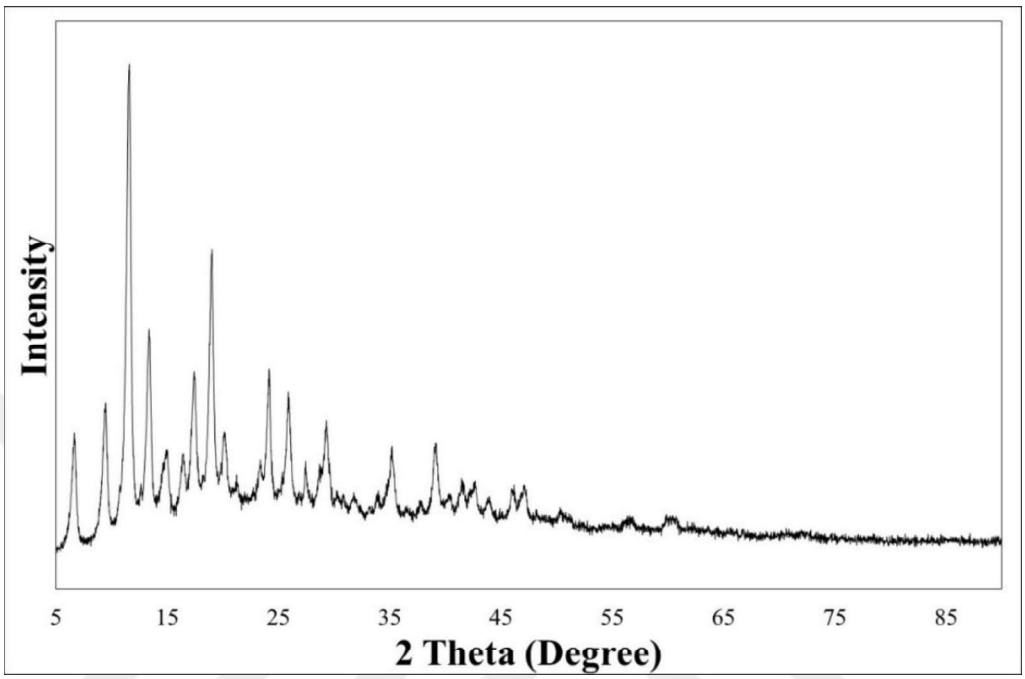

Figure 4.11. XRD pattern of CuBTC.

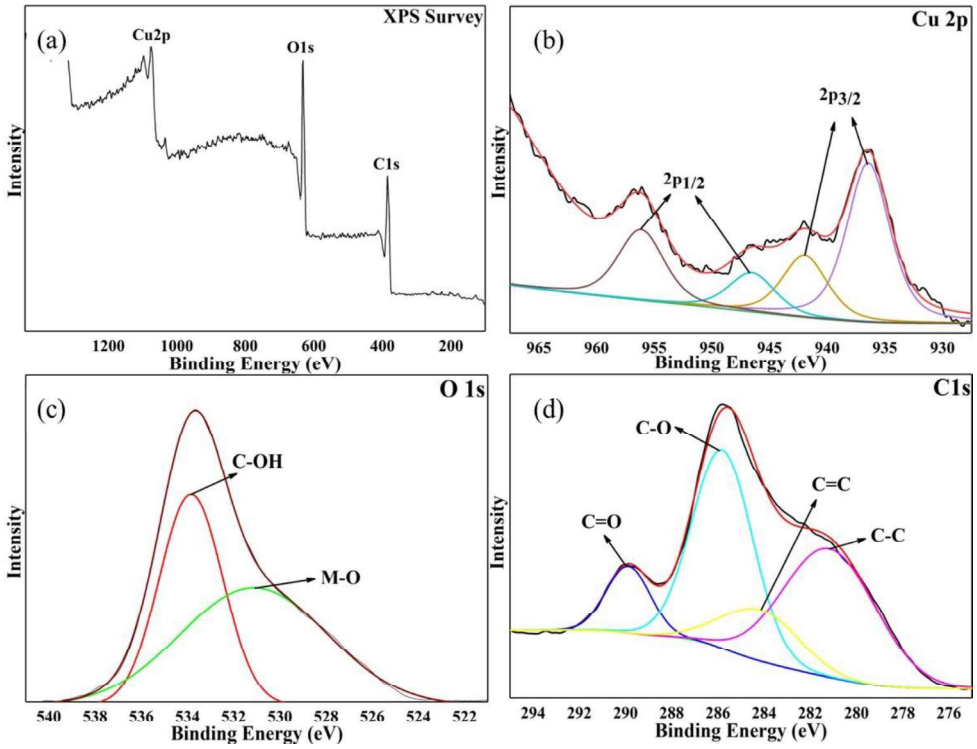

Figure 4.12. XPS pattern of CuBTC deconvoluted data a) XPS survey, b) Cu2p, c) O1s, and e) C 1s.

4.1.1.5.NiBTC. The SEM images of the NiBTC at different zoom levels were demonstrated in Figure 4.13. The metal salt $Ni(CH_3CO_2)_2.4H_2O$ and the organic linker H_3BTC were dissolved in DMF for the synthesis. The SEM morphology and crystal structure analysis verify that the NiBTC has hexagonal, rod-like structures that closely correspond to previously published research [64].

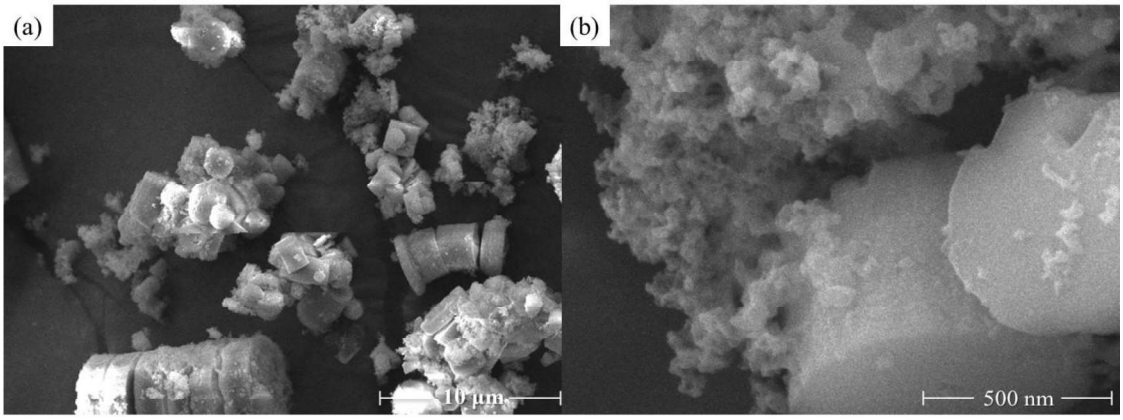

Figure 4.13. SEM images of NiBTC at a) 5000x, b) 100000x zoom level.

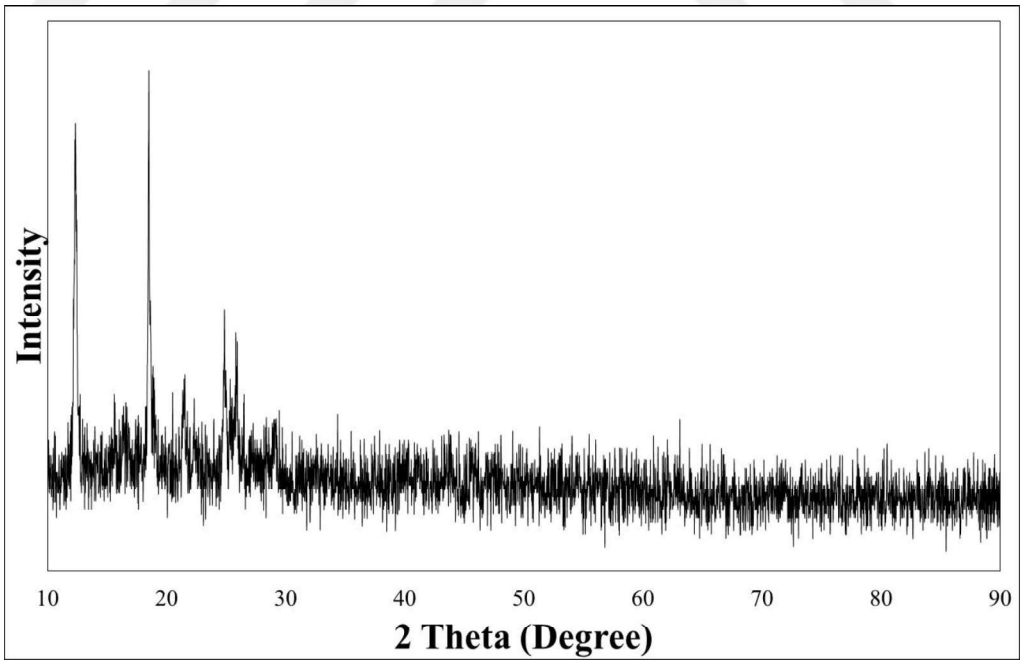

Figure 4.14. XRD pattern of NiBTC.

The Ni-BTC MOFs' XRD patterns are displayed in Figure 4.14. The sharpness of each peak indicates inherent crystallinity, and the XRD patterns are quite consistent with the literature [65].

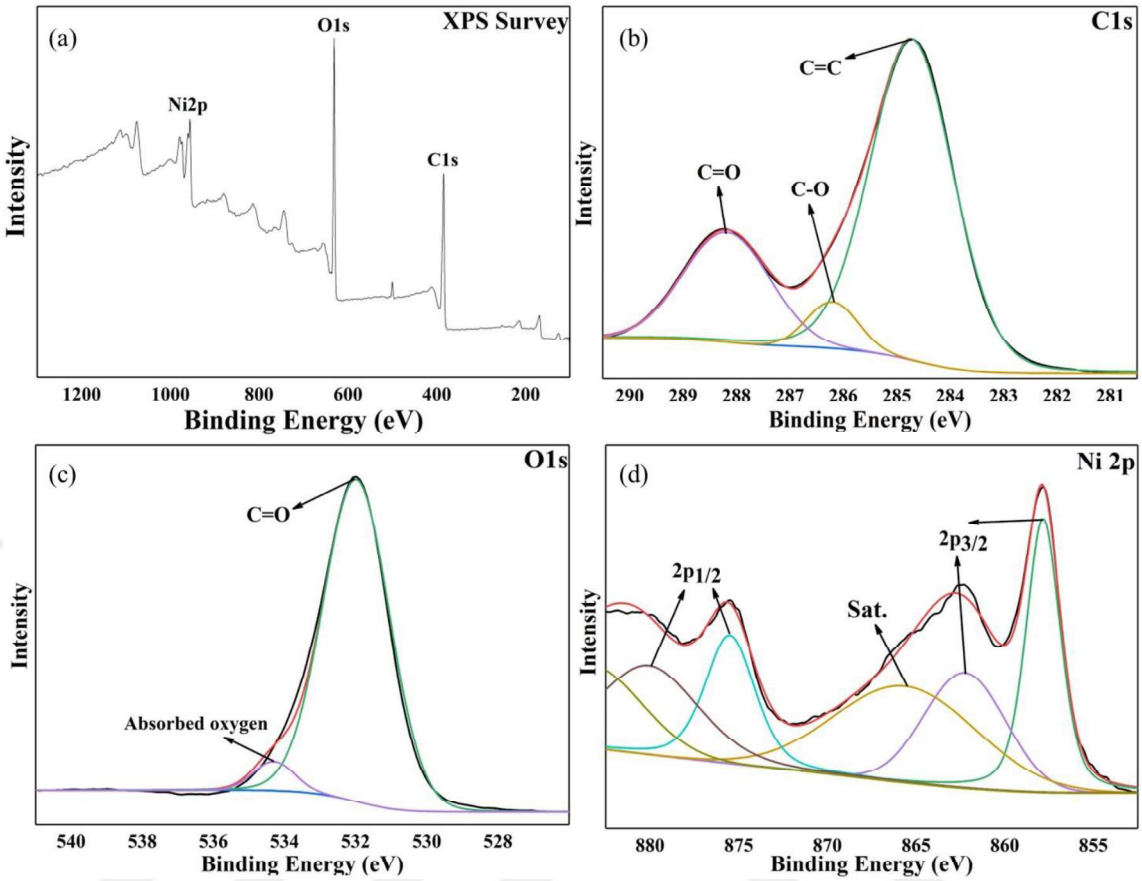

Figure 4.15. XPS pattern of NiBTC deconvoluted data a) XPS survey, b) Ni2p, c) O1s, and e) C 1s.

The surface properties and chemical state of the molecule were further examined using XPS technology. Three binding peaks in the whole spectrum were attributed to the C 1s, O 1s, and Ni 2p levels, respectively, as the figure illustrates. The peaks have been deconvoluted using many symmetrical components to identify the chemical linkages in order to fully explain the XPS results. Three symmetrical peaks at 284.21, 285.72, and 287.66, which represent the C=C, C-O, and C=O, functional groups, respectively, were used to fit the C 1s spectrum [58]. The oxygen in NiBTC shows peaks for C = O, and chemisorbed oxygen at 531.0, and 533.3 eV, in that order. The binding energy peak cannot be separately deconvoluted from the C=O peak. The synthesis of NiBTC was further validated by these binding properties [60]. The Ni 2p emission spectrum allowed for a thorough characterization of Ni^{2+} and Ni^{3+}, as demonstrated in Figure 4.15. (b), which also revealed a satellite peak. The peaks at 859.72 eV and 877.69 eV are attributed to Ni^{3+}, while the fitting peaks at 855.34 eV and 873.0 eV are associated with Ni^{2+}. The satellite peak was also discovered, with an energy of 863.12 [66].

4.1.1.6.CuNiBTC. The SEM images of the CuNiBTC at different zoom levels were demonstrated in Figure 4.16. The metal salts $Cu(OAc)_2$, $Ni(CH_3CO_2)_2.4H_2O$, and the organic linker H_3BTC were dissolved in DMF for the synthesis.

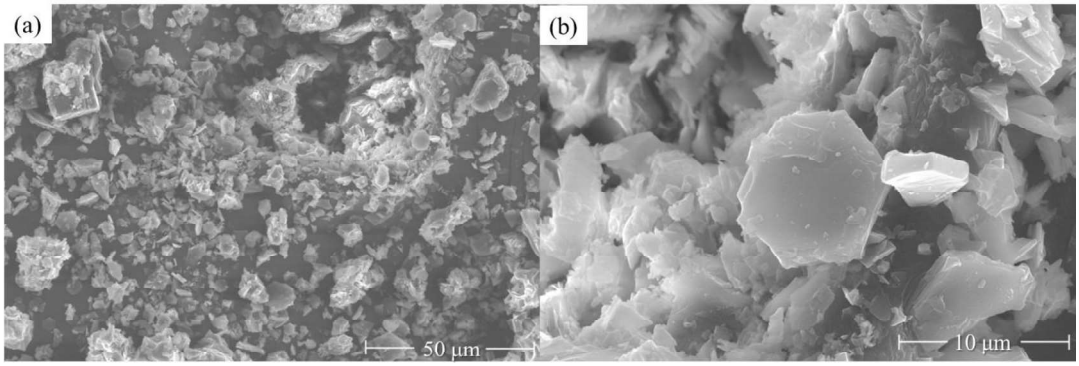

Figure 4.16. SEM images of CuNiBTC at a) 1000x, b) 8000x zoom level.

The production of hexagonal forms was demonstrated by the Ni-MOF scanning electron microscopy (SEM) image and the smooth surface of CuBTC was given previously. SEM image (in Figure 4.16) of CuNiBTC revealed that the combination of Cu-BTC and NiBTC forms the bimetallic MOF's structure. This suggests that the synthesizing nickel species with the Cu-BTC framework was successful [67].

Figure 4.17 shows the XRD peaks of the NiBTC MOF. The XRD pattern illustrates the purity of the produced bimetallic crystalline phase. The XRD pattern of the synthesized Cu-Ni-BTC clearly shows the primary diffraction peaks of Ni-BTC MOF and Cu-BTC MOF. Furthermore, these peaks show good agreement with results that have been published, suggesting that the suggested approach was successful in synthesizing Cu-Ni-BTC BMOF [68].

XPS survey analysis revealed the presence of C, O, Cu, and Ni components and provided information about the surface condition and composition of the CuNiBTC MOF. The peaks at 280.0, 283.7, 285.5, and 288.9 eV in the high-resolution spectra of C 1s are ascribed to C-C, C=C, C─O, and C=O respectively. The binding energies of 525.7 and 531.6 eV, respectively, are associated with the distinctive peaks of O-Cu/Ni and O=C, as the O1s spectrum demonstrates.

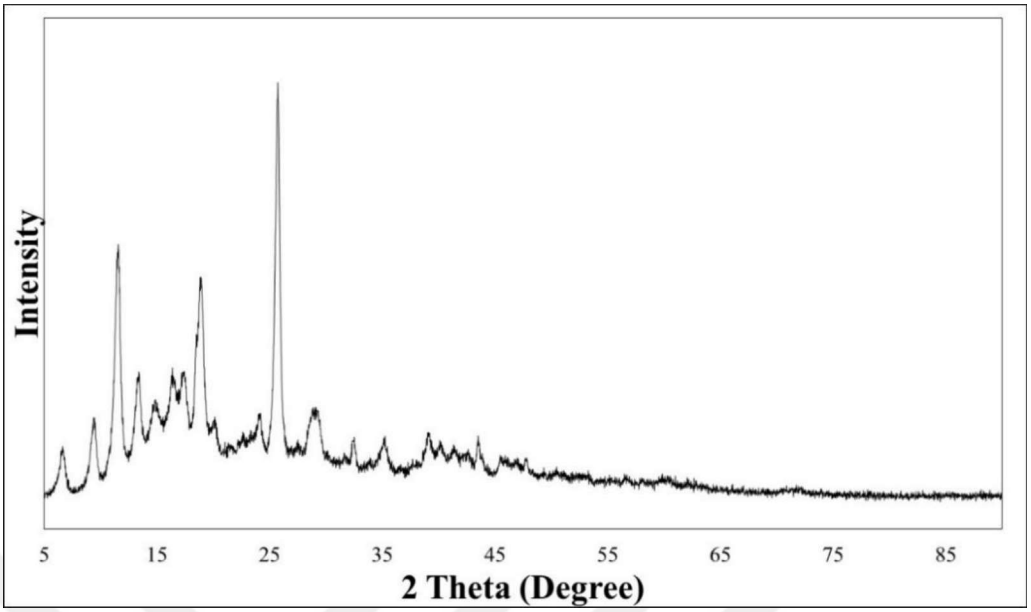

Figure 4.17. XRD pattern of CuNiBTC.

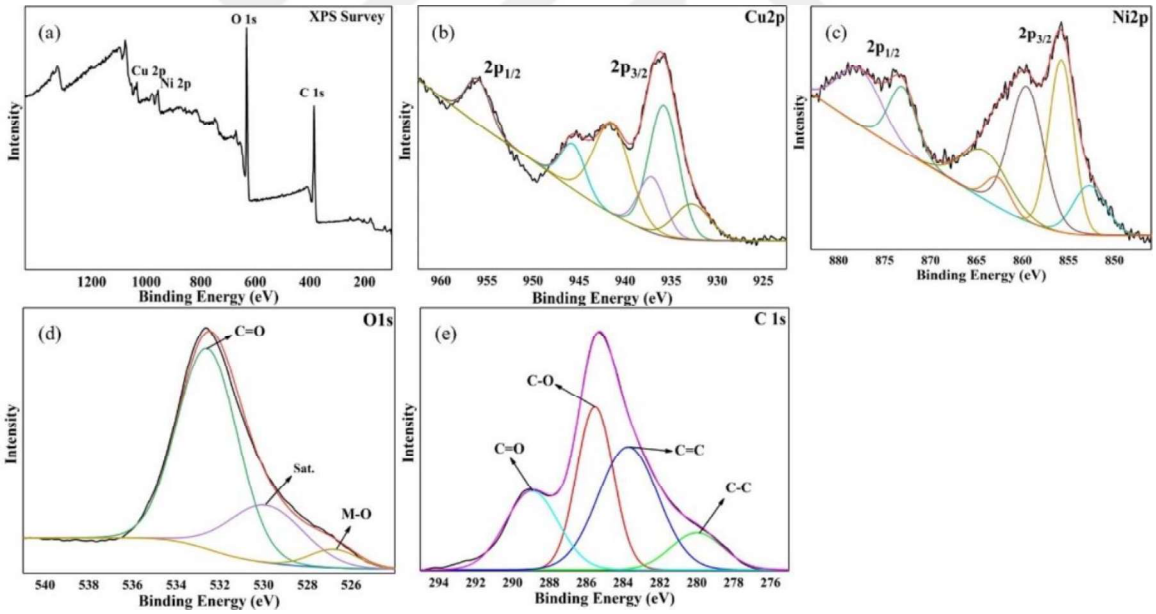

Figure 4.18. XPS pattern of CuNiBTC deconvoluted data a) XPS survey, b) Cu2p, c) Ni2p, d) O1s, and e) C 1s.

There is a peak at the binding energy of 528.8 eV and this is assigned as the satellite peak. The high-resolution curves of the Ni 2p spectra show two peaks with binding energies of 859.6 and 878.1 eV, respectively, that are associated with Ni^{3+} $2p_{3/2}$ and Ni^{3+} $2p_{1/2}$ of the CuNiBTC. The distinctive peaks of Ni^{3+} $2p_{3/2}$ Sat. and Ni^{3+} $2p_{1/2}$ Sat. are responsible for binding energies of 862.8 and 864.5, respectively [69]. The peaks at binding energies of

852.7, 855.7, and 873.1 eV at the Ni 2p XPS spectrum can be attributed to the Ni^0 $2p_{3/2}$, Ni^{2+} $2p_{3/2}$, and Ni^{2+} $2p_{1/2}$ respectively [69]. The peaks in the Cu 2p spectrum are binding energies of 930.2, 933.3, 934.7, 939.0, 943.3, and 953.5 eV. The peaks are attributed to Cu $2p_{3/2}$ at the lower energy side and Cu $2p_{1/2}$ at the higher energy side. Cu $2p_{3/2}$ and Cu $2p_{1/2}$ have binding energies of 934.7 eV and 953.5 eV, respectively. The other peaks at the binding energies are associated with the satellite peaks of Cu $2p_{3/2}$ and Cu $2p_{1/2}$ [63].

4.1.2. MOFs Synthesized with NH_3 Solvent

4.1.2.1.CuBTC. The SEM images of the CuBTC at different zoom levels were demonstrated in Figure 4.19. The metal salt $Cu(OAc)_2$ was dissolved in deionized water while the organic linker H_3BTC was dissolved in 2M of NH_3 solvent for the synthesis. A smooth surface and typical hexagonal shape of the crystal are displayed in the CuBTC SEM picture shown in Figure 4.19 [60].

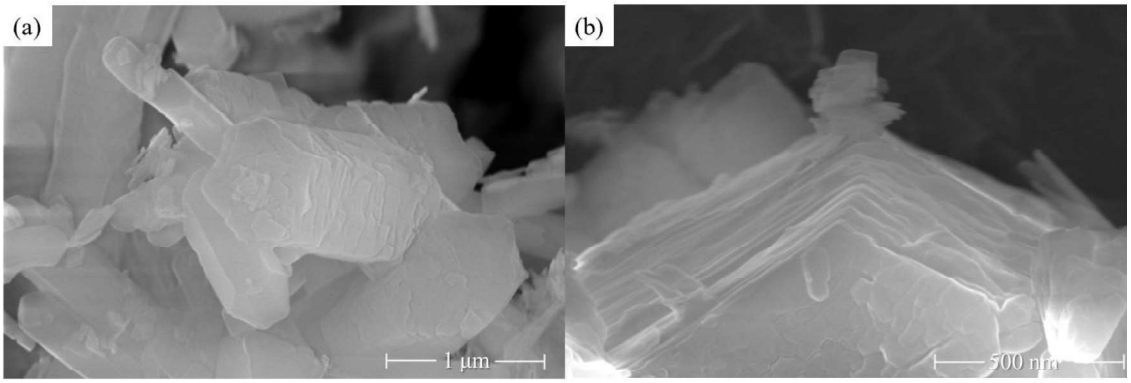

Figure 4.19. SEM images of CuBTC at a) 50000x, b) 100000x zoom level.

Powder X-ray diffraction was used to assess the synthesized materials' crystallinity. Figure 4.20 illustrates how the synthesized CuBTC's XRD pattern matches the literature's peak positions and features a unique peak at 2θ, suggesting that the products are pure phases and crystalline [62].

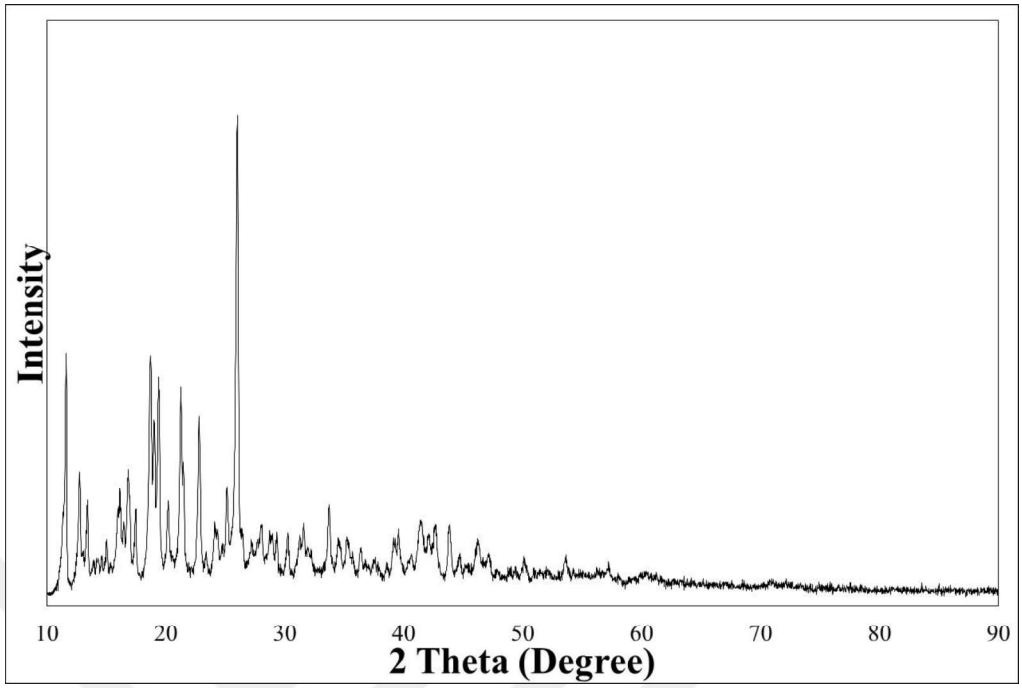

Figure 4.20. XRD pattern of CuBTC.

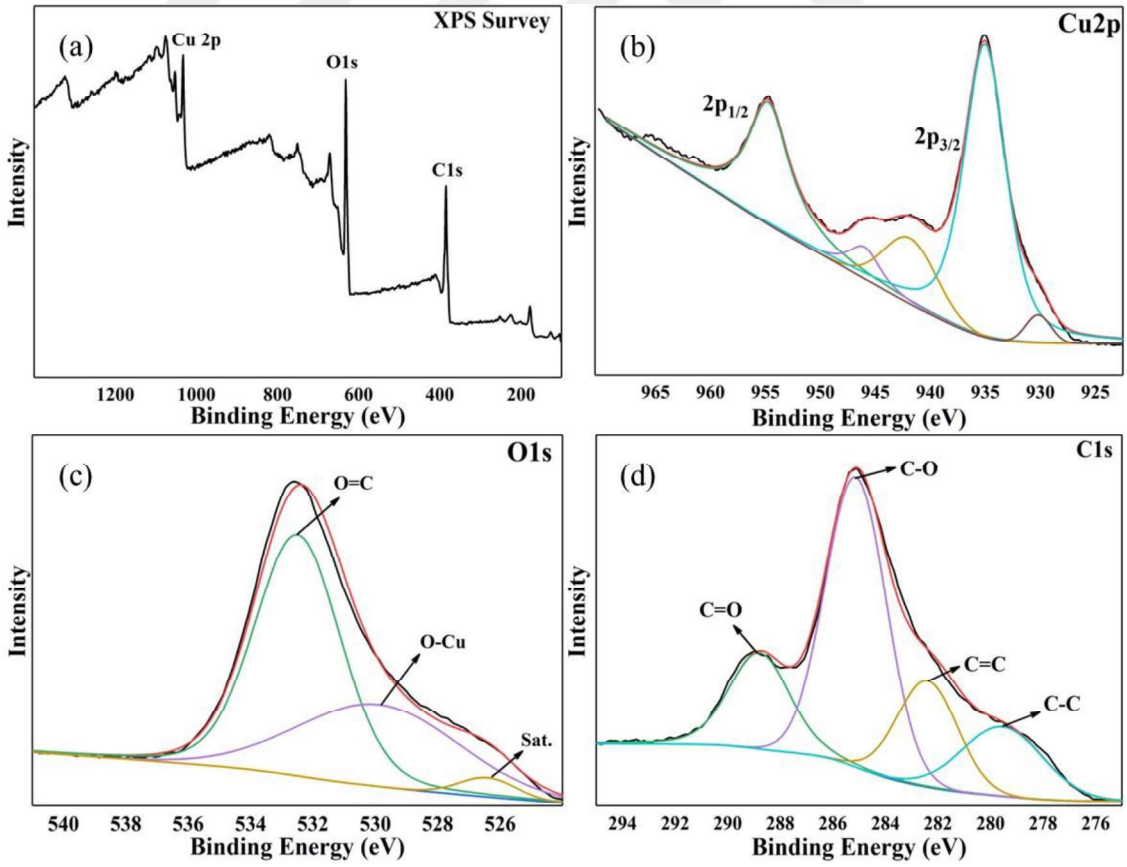

Figure 4.21. XPS pattern of CuBTC deconvoluted data a) XPS survey, b) Cu2p, c) O1s, and e) C 1s.

In Figure 4.21, deconvoluted XPS spectra were given for CuBTC. At 279.5, 282.4, 285.1 eV, and 288.7 eV, the XPS peak of C 1s can be seen. The carbon bonds corresponding to these peaks are C-C, C=C, C-O, and C=O respectively. O1s have binding energies of 531.5 eV and 529.0 eV which come from the bonds C=O and O-Cu. The peaks corresponding to Cu $2p_{3/2}$ and Cu $2p_{1/2}$ have binding energies of 932.6 eV and 952.3 eV, respectively. Binding energies of 927.7, 939.6, and 943.7 eV, are associated with the satellite peaks of Cu $2p_{3/2}$ and Cu $2p_{1/2}$ [63].

4.1.2.2.NiBTC. The SEM images of the NiBTC at different zoom levels were demonstrated in Figure 4.22. The metal salt $Ni(CH_3CO_2)_2.4H_2O$ was dissolved in deionized water while the organic linker H_3BTC was dissolved in 2M of NH_3 solvent for the synthesis. The SEM morphology and crystal structure analysis verify that the NiBTC has hexagonal, rod-like structures that closely correspond to previously published research [64].

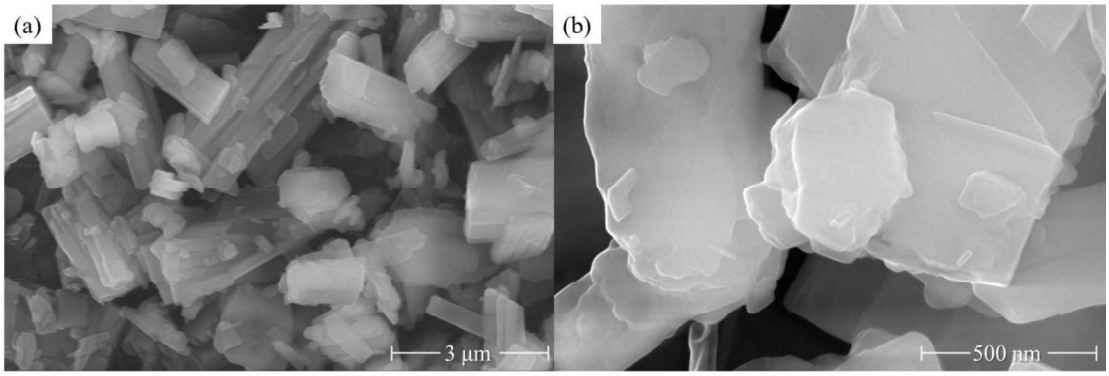

Figure 4.22. SEM images of NiBTC at a) 25000x, b) 100000x zoom level.

The Ni-BTC MOFs' XRD patterns are displayed in Figure 4.23. The sharpness of each peak indicates inherent crystallinity, and the XRD patterns are quite consistent with the literature [65].

The surface properties and chemical state of the molecule were further examined using XPS technology. Three binding peaks in the whole spectrum were attributed to the C 1s, O 1s, and Ni 2p levels, respectively, as the figure illustrates. The peaks have been deconvoluted using many symmetrical components to identify the chemical linkages in order to fully explain the XPS results. Four peaks at 283.4, 285.0, 288.9, and 291.8 eV which represent

the C-C, C=C, C-O, and C=O, functional groups, respectively, were used to fit the C 1s spectrum [58].

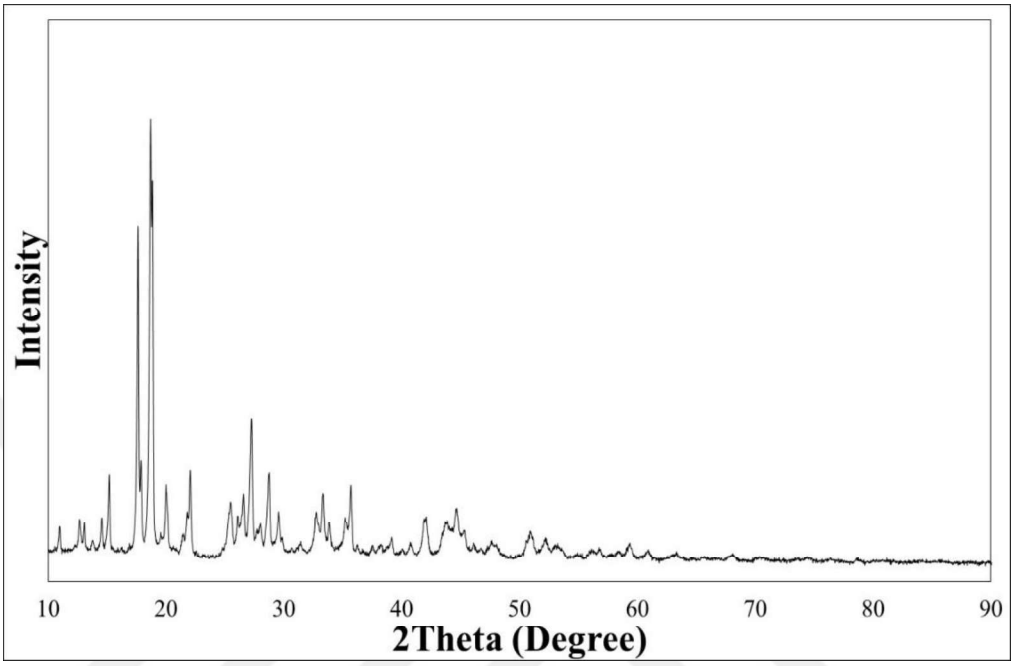

Figure 4.23. XRD pattern of NiBTC.

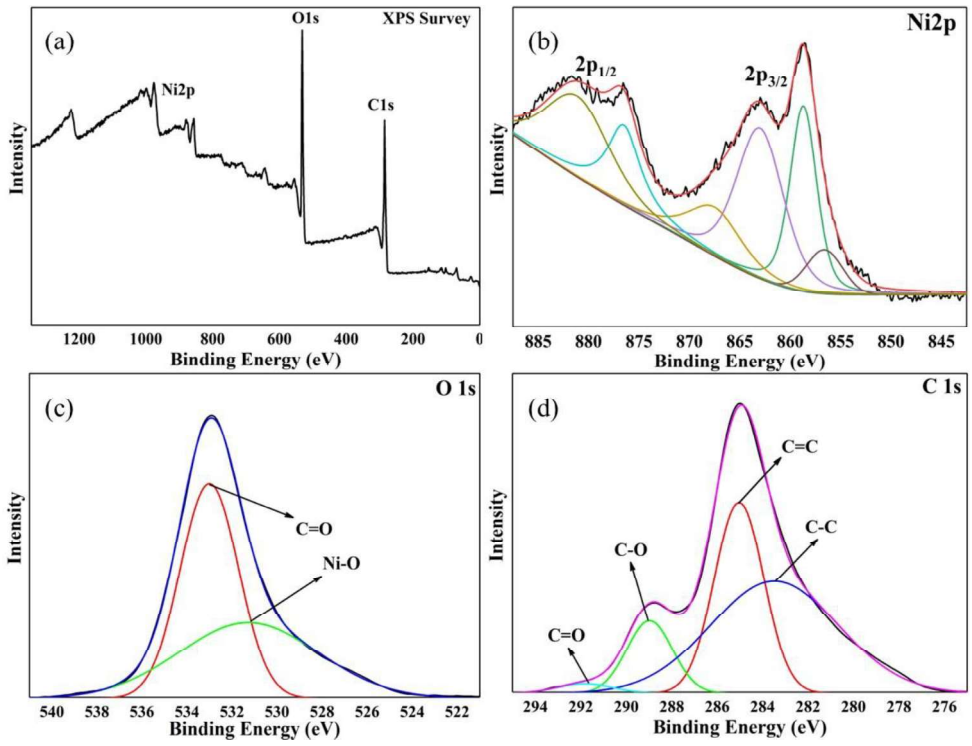

Figure 4.24. XPS pattern of NiBTC deconvoluted data a) XPS survey, b) Ni2p, c) O1s, and e) C 1s.

The oxygen in NiBTC shows peaks for C=O, and Ni-O bond at 530.2, and 531.9 eV, in that order. The synthesis of NiBTC was further validated by these binding properties [60]. The Ni 2p emission spectrum allowed for a thorough characterization of Ni^{2+} and Ni^{3+}, which also revealed a satellite peak. The peaks at 856.2 eV and 874.1 eV are attributed to Ni^{3+}, while the fitting peaks at 854.0 eV and 865.3 eV are associated with Ni^{2+}. The satellite peaks were also discovered, with energies of 860.5 and 879.1 eV [66].

4.1.2.3.CuNiBTC. The SEM images of the CuNiBTC at different zoom levels were demonstrated in Figure 4.25. The metal salts $Cu(OAc)_2$, $Ni(CH_3CO_2)_2.4H_2O$ were dissolved in deionized water while the organic linker H_3BTC was dissolved in 2M of NH_3 solvent for the synthesis. The production of the hexagonal and rod-like structure was demonstrated by the Ni-MOF scanning electron microscopy (SEM) image and the hexagonal shape with the smooth surface of CuBTC was given previously. SEM image of CuNiBTC revealed that the combination of Cu-BTC and NiBTC forms the bimetallic MOF's structure. This suggests that the synthesizing nickel species with the Cu-BTC framework was successful [67].

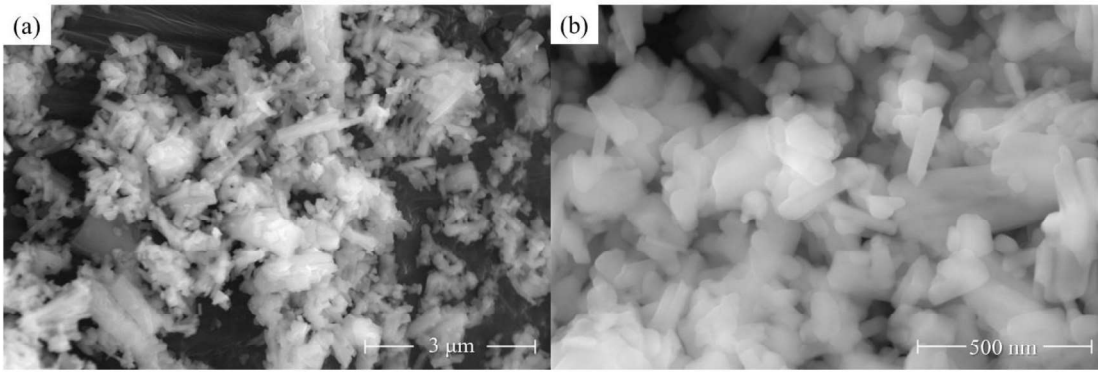

Figure 4.25. SEM images of CuNiBTC at a) 24000x, b) 100000x zoom level.

Figure 4.26 shows the XRD peaks of the CuNiBTC MOF. The XRD pattern illustrates the purity of the produced bimetallic crystalline phase. The XRD pattern of the synthesized Cu-Ni-BTC clearly shows the primary diffraction peaks of Ni-BTC MOF and Cu-BTC MOF. Furthermore, these peaks show good agreement with results that have been published, suggesting that the suggested approach was successful in synthesizing Cu-Ni-BTC BMOF [68].

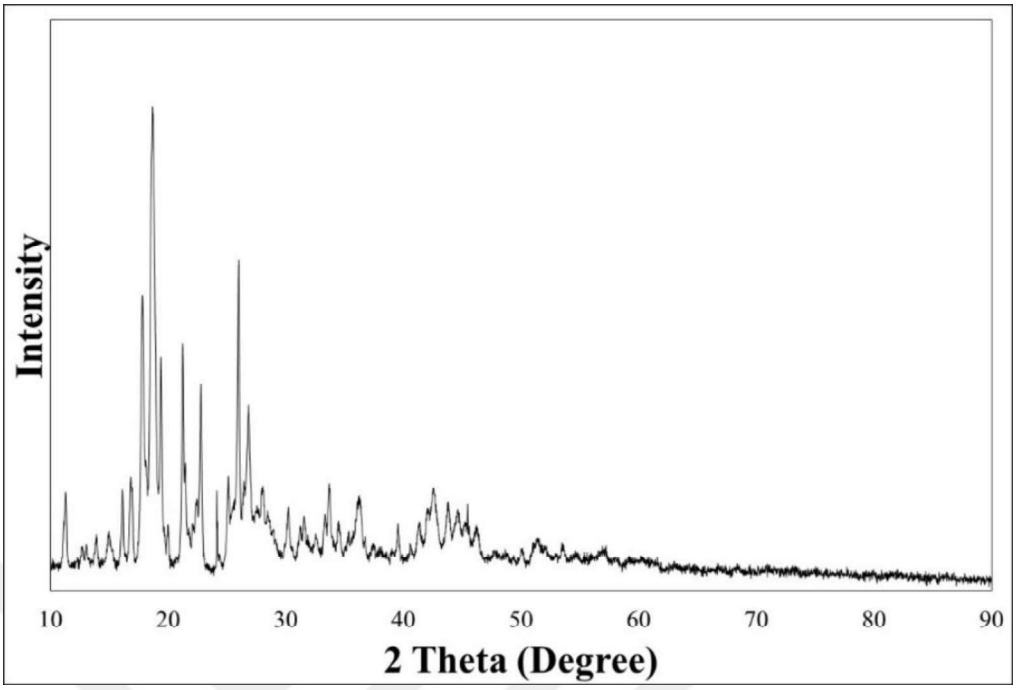

Figure 4.26. XRD pattern of CuNiBTC.

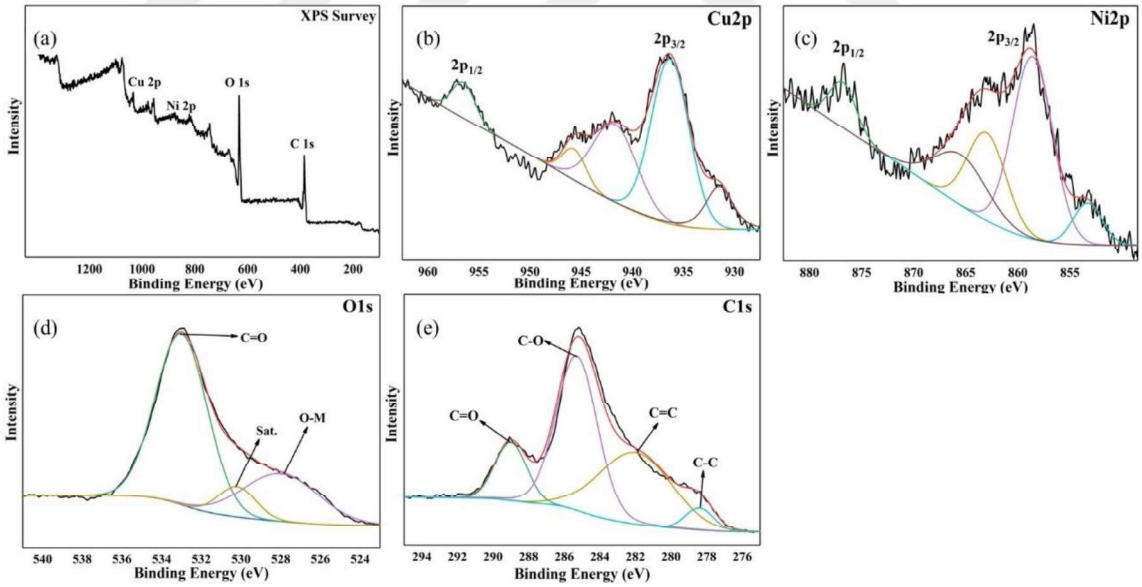

Figure 4.27. XPS pattern of CuNiBTC deconvoluted data a) XPS survey, b) Cu2p, c) Ni2p, d) O1s, and e) C 1s.

XPS survey analysis revealed the presence of C, O, Cu, and Ni components and provided information about the surface condition and composition of the CuNiBTC MOF. The peaks at 278.3, 281.9, 285.3, and 289.0 eV in the high-resolution spectra of C 1s are

ascribed to C-C, C=C, C─O, and C=O respectively. The binding energies of 526.9 and 531.9 eV, respectively, are associated with the distinctive peaks of O-Cu/Ni and O=C, as the O1s spectrum demonstrates. There is a peak at the binding energy of 529.2 eV and this is assigned as the satellite peak. The high-resolution curves of the Ni 2p spectra show two peaks with binding energies of 860.6 and 874.4 eV, respectively, that are associated with Ni^{3+} $2p_{3/2}$ and Ni^{3+} $2p_{1/2}$ of the CuNiBTC. The distinctive peak of Ni^{2+} $2p_{3/2}$ Sat. is responsible for a binding energy of 850.7 [69]. The peaks at binding energies of 856.1 and 863.7 eV at the Ni 2p XPS spectrum can be attributed to the Ni^{2+} $2p_{3/2}$ and Ni^{2+} $2p_{1/2}$ respectively [69]. The peaks in the Cu 2p spectrum are binding energies of 928.9, 933.8, 939.4, 939.0, 943.4 and 954.0 eV. The peaks are attributed to Cu $2p_{3/2}$ at the lower energy side and Cu $2p_{1/2}$ at the higher energy side. Cu^{3+} $2p_{3/2}$ and Cu^{3+} $2p_{1/2}$ have binding energies of 933.8 eV and 954.0 eV, respectively. The binding energy of 939.4 can be associated with the Cu^{2+} $2p_{3/2}$. The other peak at the binding energy of 928.9 is assigned as the satellite peak of Cu $2p_{3/2}$ [63].

4.2. Conductivities and ORR activities of Prepared Electrodes

4.2.1. SSMs Coated with Carbon Slurries

The coating was prepared by using 90% CB and 10% PVA. Electrochemical analysis of SSM coated with CB and PVA binder uses chronopotentiometry and cyclic voltammetry. The conductivity change of the SSM was calculated according to chronopotentiometry results. The following table shows the conductivity results for the uncoated and coated SSM.

Table 4.1. Conductivity of SSM before and after the coating with CB-PVA-contained slurry.

	Uncoated Stainless-Steel Mesh (S/m)	**CB-Coated Stainless-Steel Mesh (S/m)**
CB/PVA (SSM #1)	3.56×10^7	2.24×10^8

The CV curve of SSM #1, coated with 90% CB and 10% PVA by solid weights, is shown in Figure 4.28 with a 50 mV/s scan rate. No oxidation-reduction peaks are observed in oxygen-purged and nitrogen-purged cases. Since the CB-coated SSM (SSM #1) was used as electrodes in the fuel cell, the ORR peak is not observed, therefore these materials are inert and suitable ORR under fuel cell conditions.

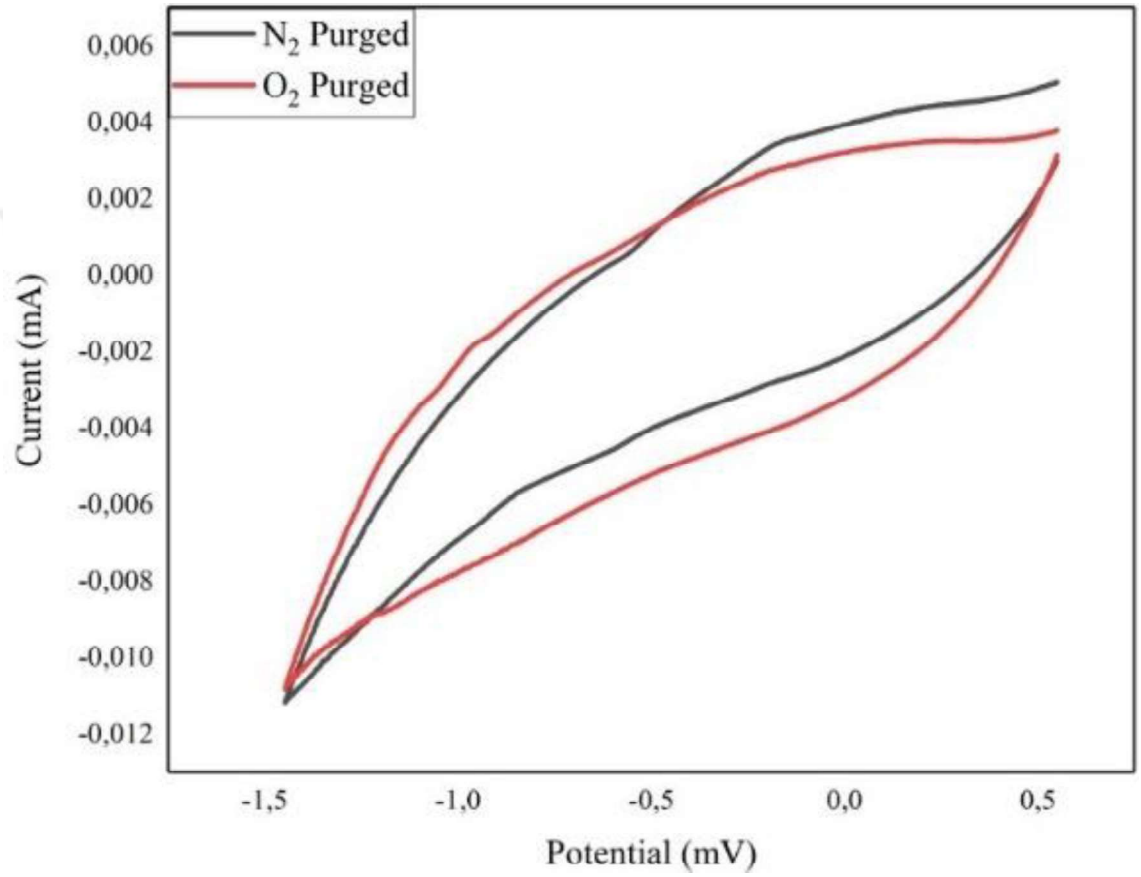

Figure 4.28. CV Curve of CB coated SSM (SSM#1) with O_2 purged and N_2 Purged at a scan rate of 50 mV/s.

4.2.2. SSMs Coated with MOF Containing Slurries

In order to prepare CB-MOF composite slurries, all coatings were prepared using 10% CB, 10% PVA, and 80% MOF material. Electrochemical analysis was done using chronopotentiometry and cyclic voltammetry measurements. Conductivity calculations were done according to chronopotentiometry measurements. The following table (Table 4.2) shows the conductivity values of the MOF-CB composite-coated SSMs. The conductivity values are expected to increase after coating due to the carbon and metal source situated in

the MOFs. All meshes showed an increasing trend in conductivity. The difference between conductivity values of uncoated and coated might be caused by the metal source variation.

Table 4.2. Conductivity values for Uncoated and MOF-CB composite coated SSMs.

SSM	MOF	Solvent	Uncoated Stainless-Steel Mesh (S/m)	MOF-CB Composite Coated Stainless-Steel Mesh (S/m)
SSM#2	CoBTC	DMF	6.44×10^7	8.87×10^7
SSM#3	FeBTC	DMF	4.34×10^7	6.32×10^7
SSM#4	FeCoBTC	DMF	7.75×10^7	9.53×10^7
SSM#5	CuBTC	DMF	5.48×10^7	13.5×10^7
SSM#6	NiBTC	DMF	26.6×10^7	46.9×10^7
SSM#7	CuNiBTC	DMF	5.94×10^7	23.2×10^7
SSM#8	CuBTC	Water-NH_3	2.08×10^7	25.1×10^7
SSM#9	NiBTC	Water-NH_3	13.2×10^7	18.8×10^7
SSM#10	CuNiBTC	Water-NH_3	2.60×10^7	58.1×10^7

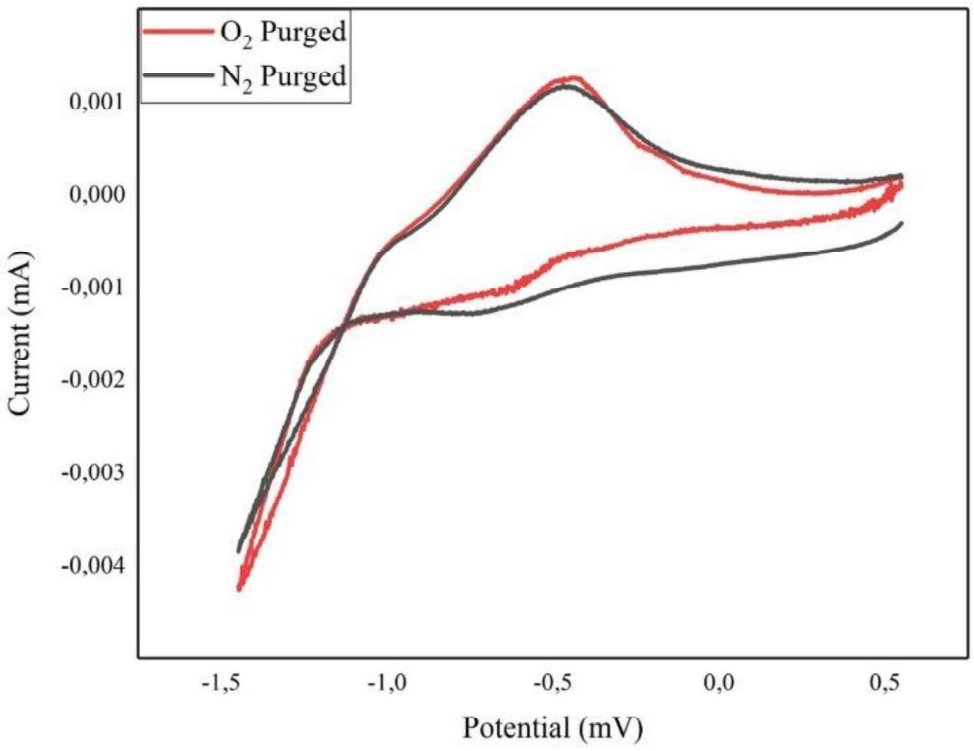

Figure 4.29. CV Curve of CB-CoBTC MOF composite coated SSM (SSM#2) with O_2 purged and N_2 Purged at a scan rate of 50 mV/s.

In Figure 4.29 CV plot of CoBTC-CB coated SSM (SSM#2) with 50 mV/s scan rate while oxygen gas and nitrogen gas purged cases are shown. There can be observed a small oxygen reduction peak around -0.5 mV in PBS with oxygen purged case. There is a peak observed in nitrogen nitrogen-purged case but it is smaller than the oxygen-purged one. The peak in nitrogen nitrogen-injected case may caused by the remained oxygen content in the PBS solution.

CV plot of FeBTC-CB composite coated SSM (SSM#3) with 50 mV/s scan rate is shown in Figure 4.30. CV curves show an oxygen reduction peak of around -0.4 mV in PBS with oxygen-purged and nitrogen-purged cases. The reason for the peak in the nitrogen purged case might be the remained oxygen in the PBS solution, in other words, the nitrogen gas was insufficient to reduce the oxygen content in the solution.

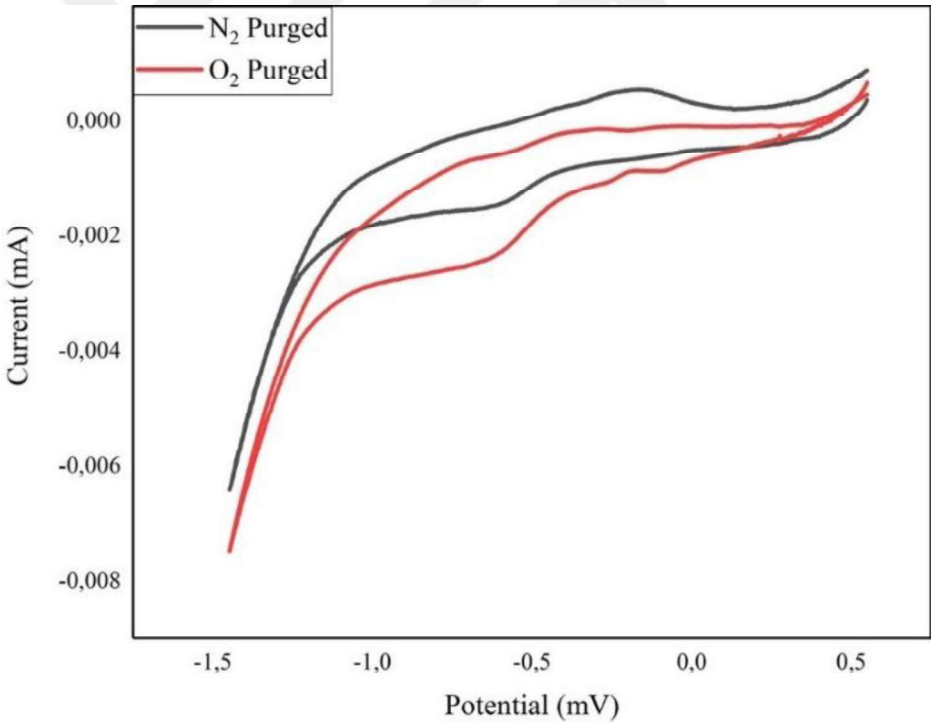

Figure 4.30. CV Curve of CB-FeBTC MOF composite coated SSM (SSM#3) with O_2 purged and N_2 Purged at a scan rate of 50 mV/s.

CV plot of FeCoBTC-CB composite coated SSM (SSM #4) at 50 mV/s scan rate is given in Figure 4.31. The CV curve of the O_2 purged system shows an oxygen reduction peak of around -0.4 mV in PBS. There is no ORR peak observed in the nitrogen-purged case as expected.

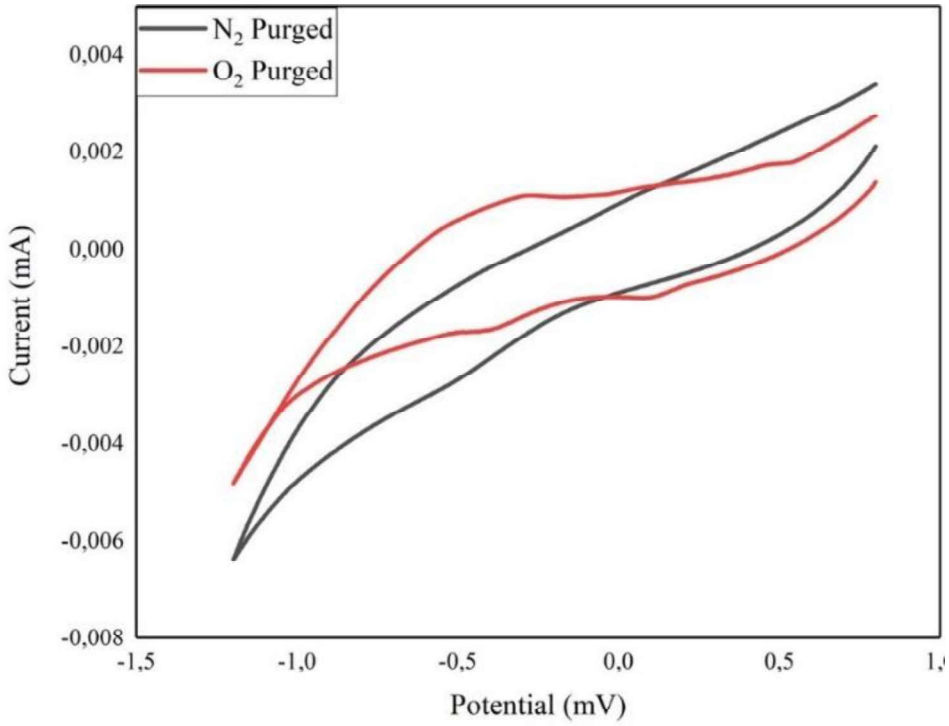

Figure 4.31. CV Curve of CB-FeCoBTC MOF composite coated SSM (SSM#4) with O_2 purged and N_2 Purged at a scan rate of 50 mV/s.

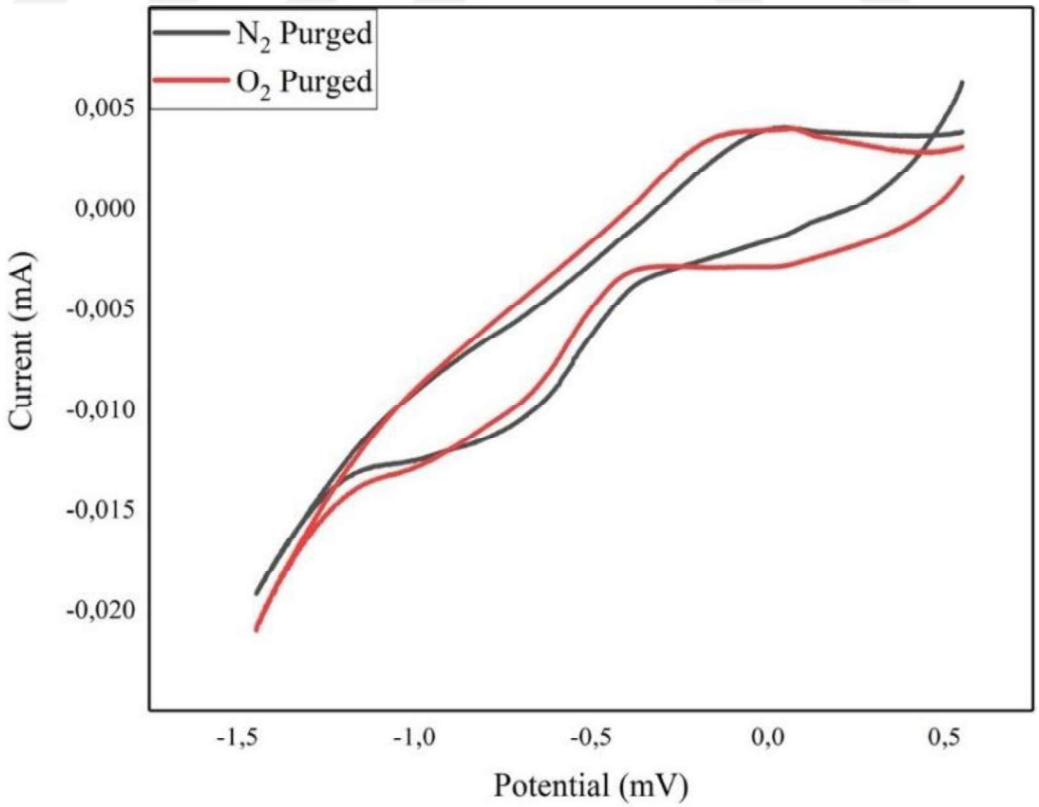

Figure 4.32. CV Curve of CB-CuBTC MOF composite coated SSM (SSM#5) with O_2 purged and N_2 Purged at a scan rate of 50 mV/s.

CV plot of CuBTC-CB composite coated SSM (SSM#5) with 50 mV/s scan rate is shown in Figure 4.32. Around -0.5 mV with oxygen purged case a peak can be observed. For the nitrogen case, there is no distinctive ORR peak in the CV curve.

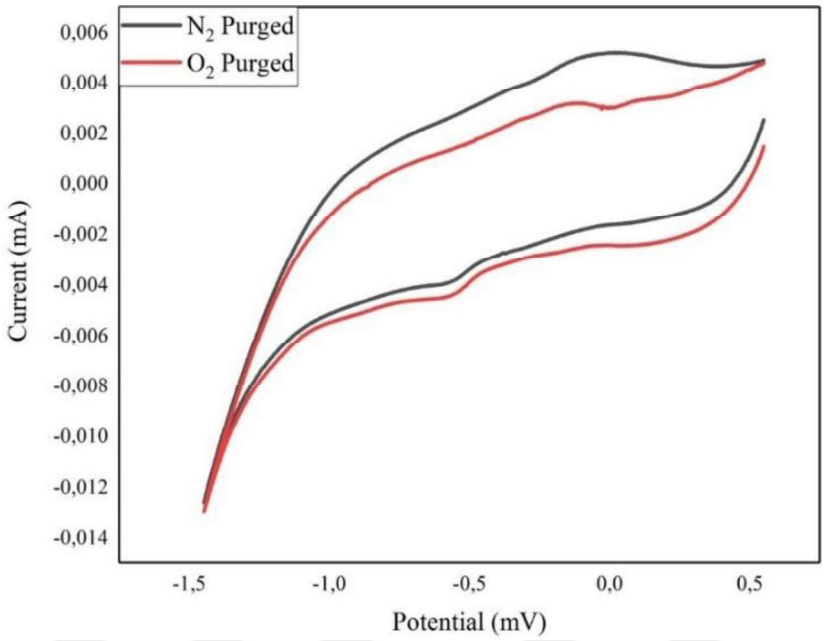

Figure 4.33. CV Curve of CB-NiBTC MOF composite coated SSM (SSM#6) with O_2 purged and N_2 Purged at a scan rate of 50 mV/s.

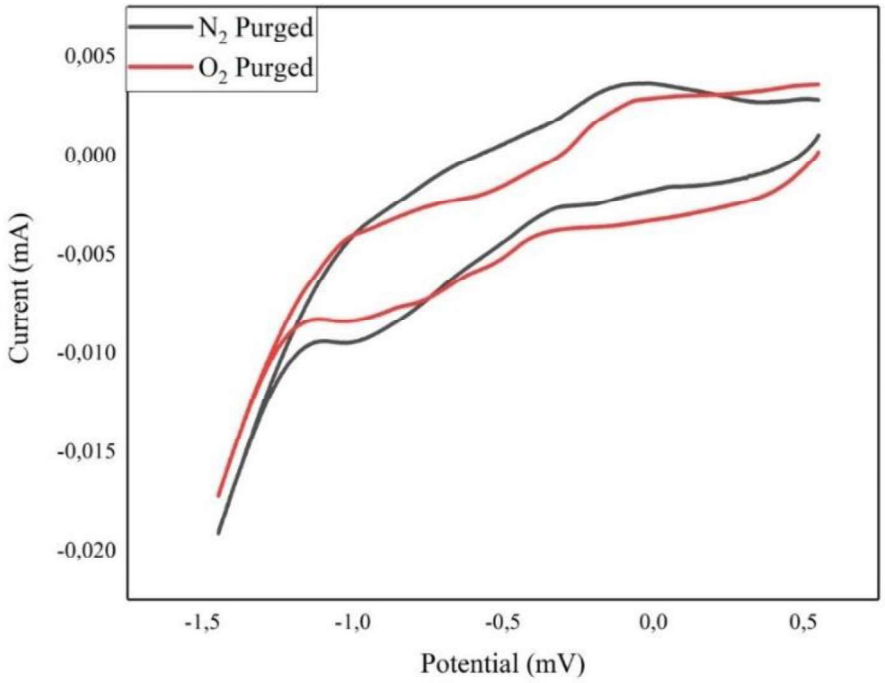

Figure 4.34. CV Curve of CB-CuNiBTC MOF composite coated SSM (SSM#7) with O_2 purged and N_2 Purged at a scan rate of 50 mV/s.

CV plot of NiBTC-CB composite coated SSM (SSM#6) with 50 mV/s scan rate is shown in Figure 4.33. CV curves show an oxygen reduction peak of around -0.3 mV in PBS with oxygen-purged and nitrogen-purged cases. The reason for the peak in the nitrogen purged case might be the remained oxygen in the PBS solution, in other words, the nitrogen gas was insufficient to reduce the oxygen content in the solution.

CV plot with 50 mV/s scan rate of CuNiBTC-CB composite coated mesh in Figure 4.34 shows a small oxygen reduction peak around -0.4 mV in PBS with oxygen purged cases but there is no distinctive ORR peak with nitrogen purged case.

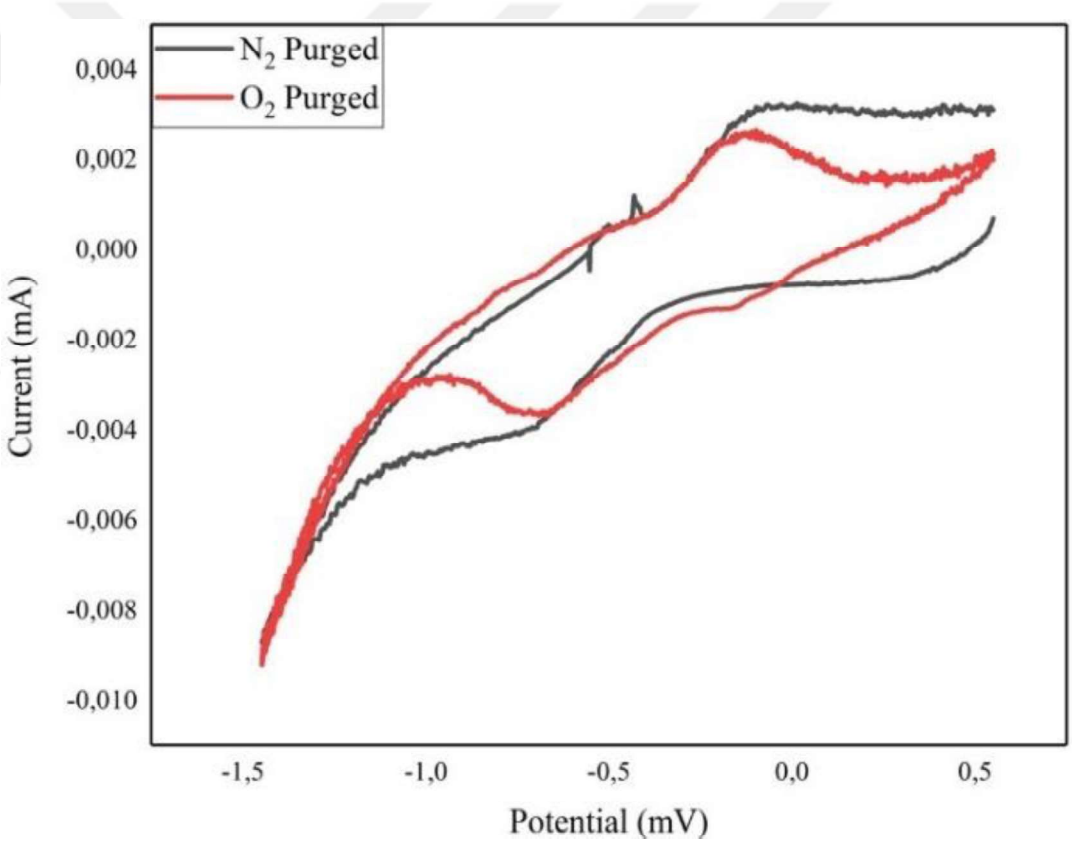

Figure 4.35. CV Curve of CB-CuBTC MOF composite coated SSM (SSM#8) with O_2 purged and N_2 Purged at a scan rate of 50 mV/s.

CV plot of CuBTC-CB composite coated SSM (SSM#8) with 50 mV/s scan rate is shown in Figure 4.35. CV curves show an oxygen reduction peak around -0.4 mV in PBS with oxygen purged case. There are smaller peaks in the CV curve of nitrogen purged system and these may caused by the remained oxygen content in the system.

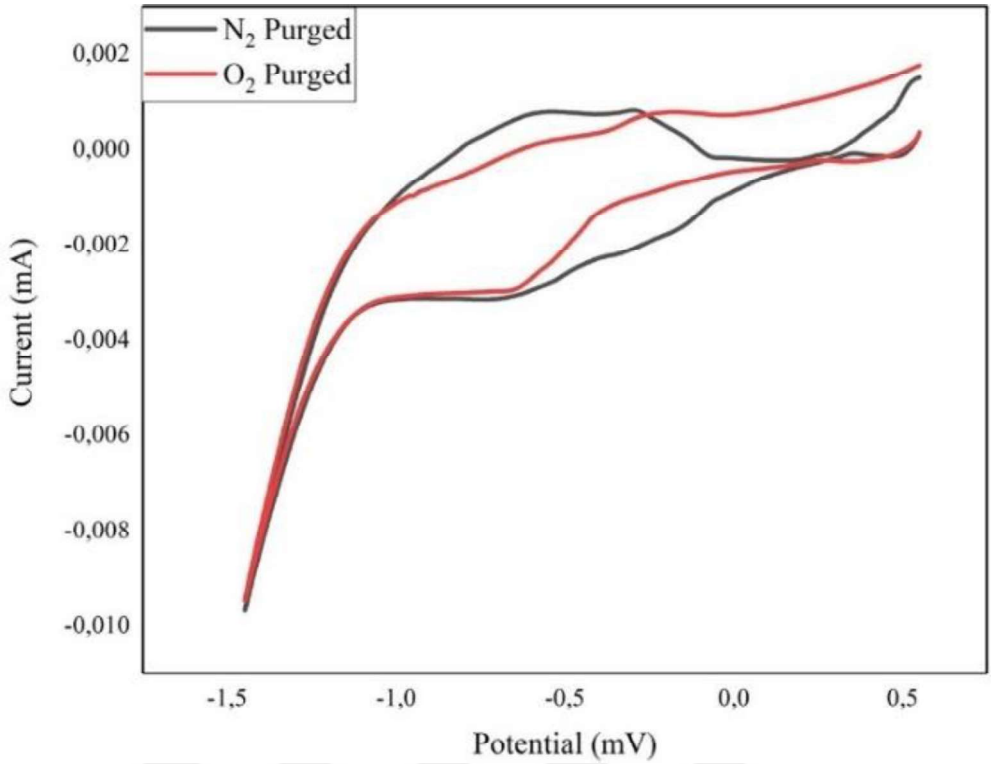

Figure 4.36. CV Curve of CB-NiBTC MOF composite coated SSM (SSM#9) with O_2 purged and N_2 Purged at a scan rate of 50 mV/s.

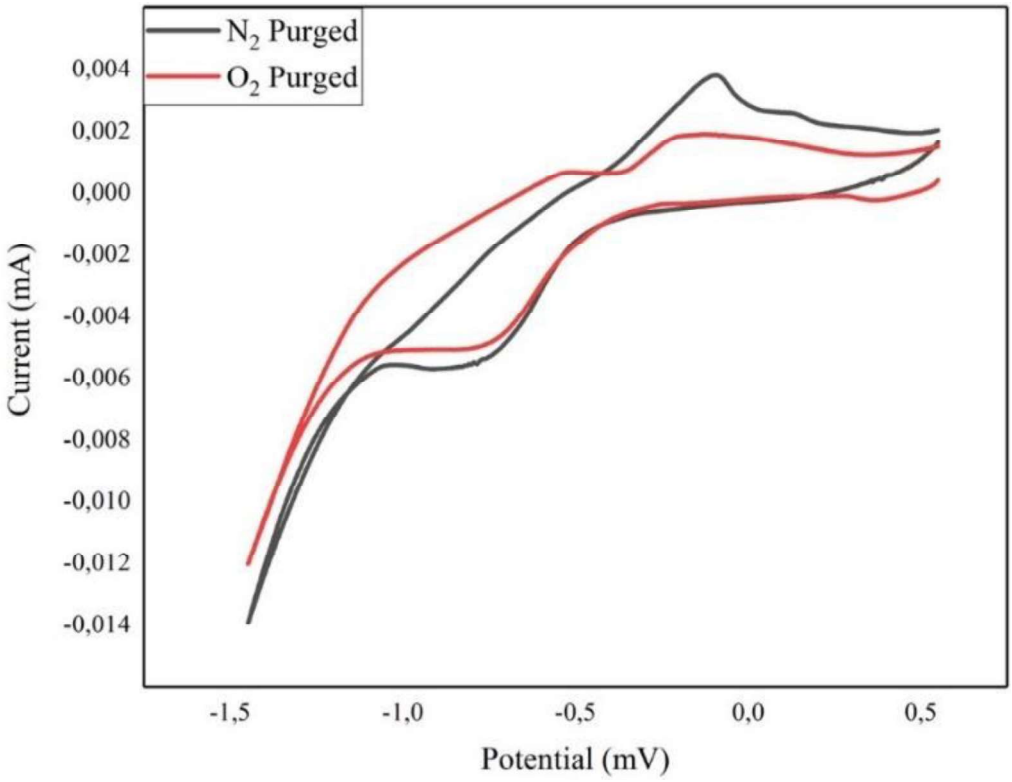

Figure 4.37. CV Curve of CB-CuNiBTC MOF composite coated SSM (SSM#10) with O_2 purged and N_2 Purged at a scan rate of 50 mV/s.

Table 4.3. ORR Peak position table for MOF coated SSMs.

SSM	ORR Peak	Peak Position
CB/PVA (SSM #1)	Not observed	-
CoBTC (SSM #2)	Observed	-0.4 V
FeBTC (SSM #3)	Observed	-0.4 V
FeCoBTC (SSM #4)	Observed	-0.4 V
CuBTC (SSM #5)	Observed	-0.5 V
NiBTC (SSM #6)	Observed	-0.4 V
CuNiBTC (SSM #7)	Observed	-0.5 V
CuBTC (SSM #8)	Observed	-0.4 V
NiBTC (SSM #9)	Observed	-0.4 V
CuNiBTC (SSM #10)	Observed	-0.5 V

CV plot of NiBTC-CB composite coated SSM (SSM#9) with 50 mV/s scan rate is shown in Figure 4.36. CV curves show an oxygen reduction peak around -0.4 mV in PBS with oxygen purged case. There is no distinctive ORR peak in the CV curve of the nitrogen-purged system.

CV plot of CuNiBTC-CB composite coated SSM (SSM#10) with 50 mV/s scan rate is shown in Figure 4.37. CV curves show an oxygen reduction peak of around -0.5 mV in PBS with oxygen-purged and nitrogen-purged cases. The reason for the peak in the nitrogen purged case might be the remaining oxygen in the PBS solution, in other words, the nitrogen gas was insufficient to reduce the oxygen content in the solution.

The CV results revealed that the synthesized MOFs were possible candidates for preparing cathode electrodes as cathode catalysts. ORR peaks were observed at similar voltage values. The small variety of ORR peak positions might be caused by the reaction kinetics between O_2 molecules and active metal sites of MOFs.

4.3. Electrochemical Performance of SSM Electrodes in MFCs

CB-coated stainless steel mesh (SSM #1) was utilized as an anode electrode since it has increasing conductivity with coating and physical integrity of the coating. Various MOFs were used to prepare MOF-CB composites, and the coated SSMs were utilized and analyzed as cathode electrodes in the constructed MFC. The evaluations of the performance of the cathodes with SSM #1 anode were completed with OCV, LSV, and EIS. Both biotic (E. Coli K-12 inoculated) and abiotic (blank, only buffer medium of E.Coli) MFCs were tested to evaluate the MOF-catalyzed performance. Before conducting LSV analyses, OCV was performed until the voltage became stable. Current density vs. power density graphs were drawn by normalizing raw data concerning the cathode surface area.

Figure 4.38 compares the abiotic and biotic cells constructed with the presence of CoBTC MOF. A point at zero current at the first (left side) vertical axis shows the open circuit potential of cells, while the second (right side) vertical axis shows maximum power density. The horizontal axis is present to demonstrate the maximum current generated. The maximum power density generated is 2.5 x 10^{-3} mW/cm^2 with the CoBTC cathode catalyst of biotic cell which is 5 times higher than the abiotic cell. The comparison summarizes that the biotic cell generates more current and power than the abiotic cell. The power density result also correlates with CV curves which gave ORR peak. CoBTC was successful in catalyzing the ORR. Also, OCV value can be observed from Figure 4.38 and it is the highest value at the potential axis. OCV value is 0.31 V for both abiotic and biotic cells.

The electrochemical impedance spectrum is shown in Figure 4.39 for the abiotic and biotic cells constructed with CoBTC MOF. The red semicircle (or arc) corresponds to the abiotically run fuel cell while the blue semicircle corresponds to the biotic cell. The significance of the semicircle is that the internal resistance on the x-axis and capacitance value on the y-axis. The graph can be evaluated as the resistance of the cell decreases after it is operated biotically. In addition, the capacitance behavior of the cell decreased after microbial inoculation. The rise at the end of the blue semicircle might correspond to the diffusion layer of the cell.

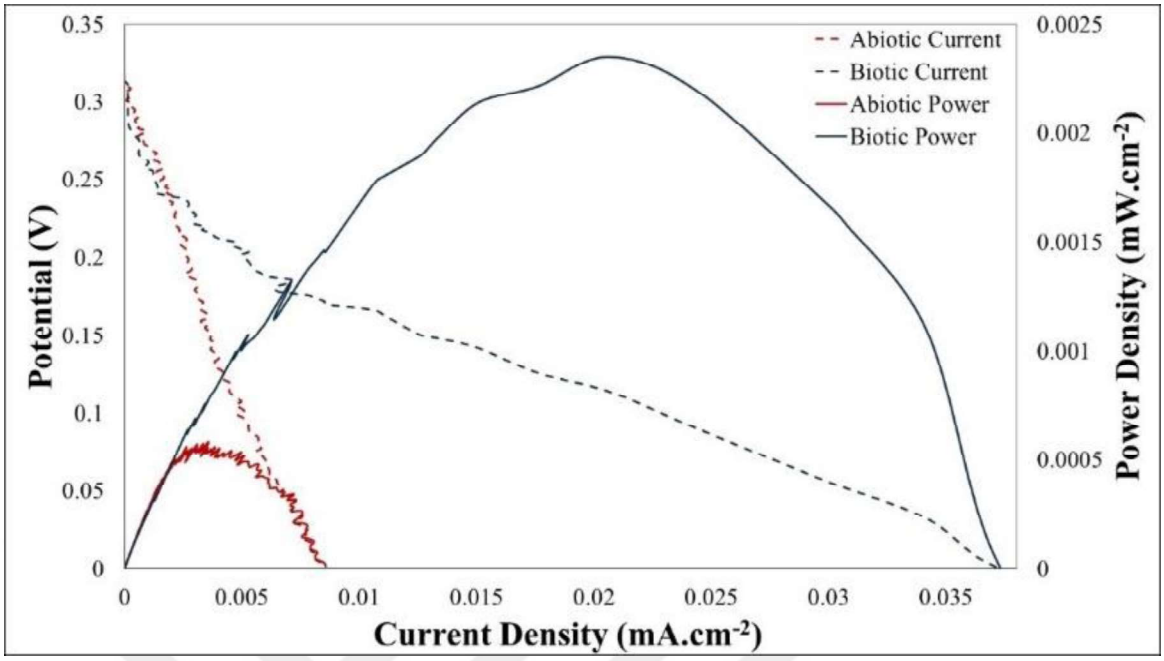

Figure 4.38.Maximum current density and maximum power density comparison between abiotic and biotic fuel cell constructed using CoBTC MOF (SSM #2) cathode catalyst.

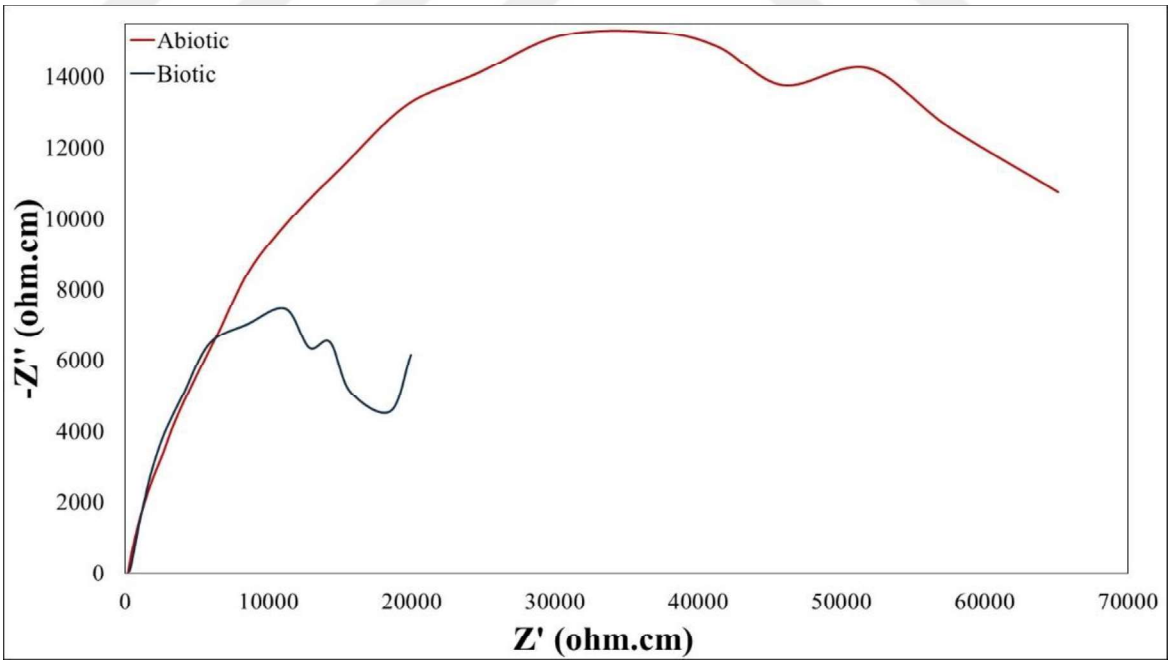

Figure 4.39. EIS curve for MFC with CoBTC (SSM #2).

Figure 4.40 compares the abiotic and biotic cells constructed with the presence of FeBTC MOF. The biotic cell generated higher current and power than the abiotic cell. The highest power density generated by biotic cells is 2.0 x 10^{-3} mW/cm^2 and abiotic cell is 9.6

x 10^{-5} mW/cm^2. The biotic cell generated a maximum power density 20 times higher than the abiotic cell. The irregularity of the biotic cell data could arise from the insufficiency of gas or lack of contact with the system. OCV for abiotic and biotic cells is 0.18 V and 0.30 V respectively.

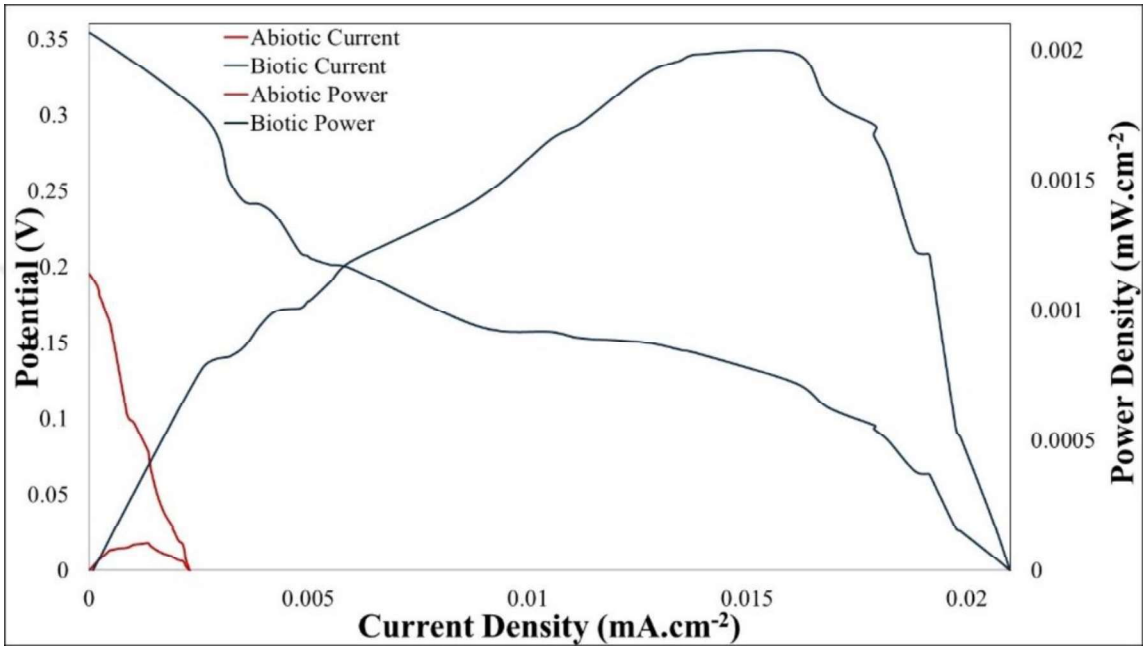

Figure 4.40. Maximum current density and maximum power density comparison between abiotic and biotic fuel cell constructed using FeBTC MOF (SSM #3) cathode catalyst.

The electrochemical impedance spectrum in Figure 4.41 for the abiotic and biotic cells constructed with FeBTC MOF shows that the internal resistance decreases after the cell is operated with bacteria. Also, the capacitance behavior of the cell decreased after microbial inoculation. The smaller semicircle at the lower frequency on the biotic cell might belong to the cathodic reaction that occurred in the biotic cell.

Figure 4.42 compares the abiotic and biotic cells constructed with the presence of FeCoBTC MOF. The biotic cell generated higher current and power than the abiotic cell. The highest power density generated by biotic and abiotic cells is 6.0 x 10^{-3} mW/cm^2 and 2.1 x 10^{-6} mW/cm^2 respectively. The bimetallic FeCoBTC has the highest power generation effect among Fe and Co-based MOFs. The OCV for abiotic cells is 0.0075 V while for biotic cells is 0.51 V.

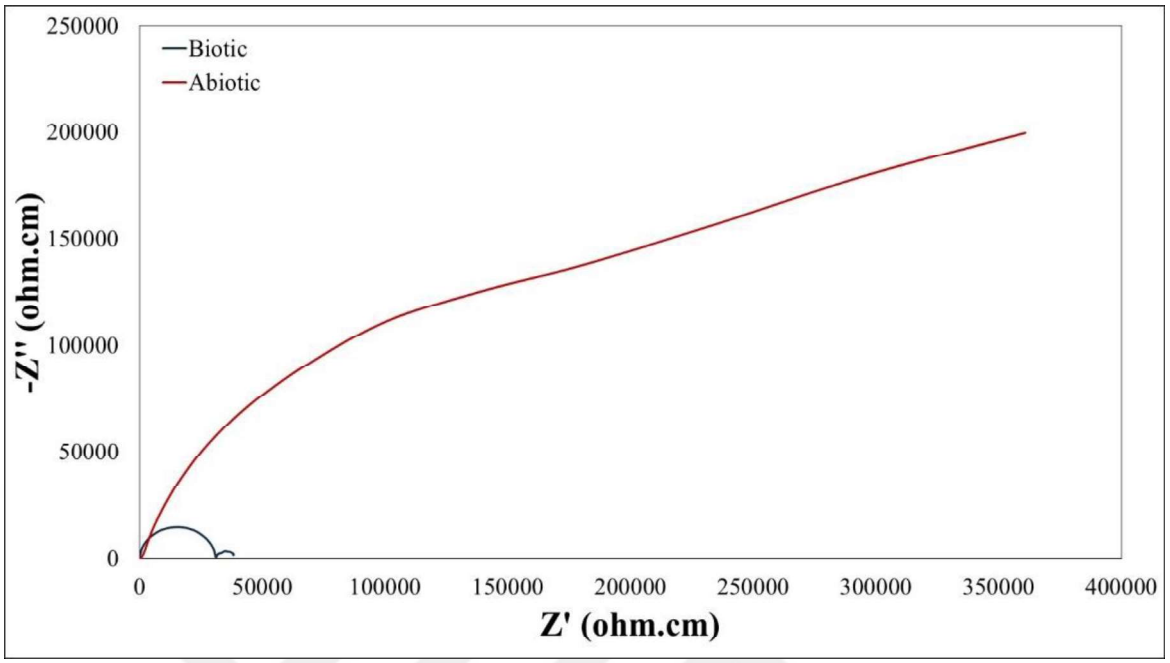

Figure 4.41. EIS curve for MFC with FeBTC (SSM#3).

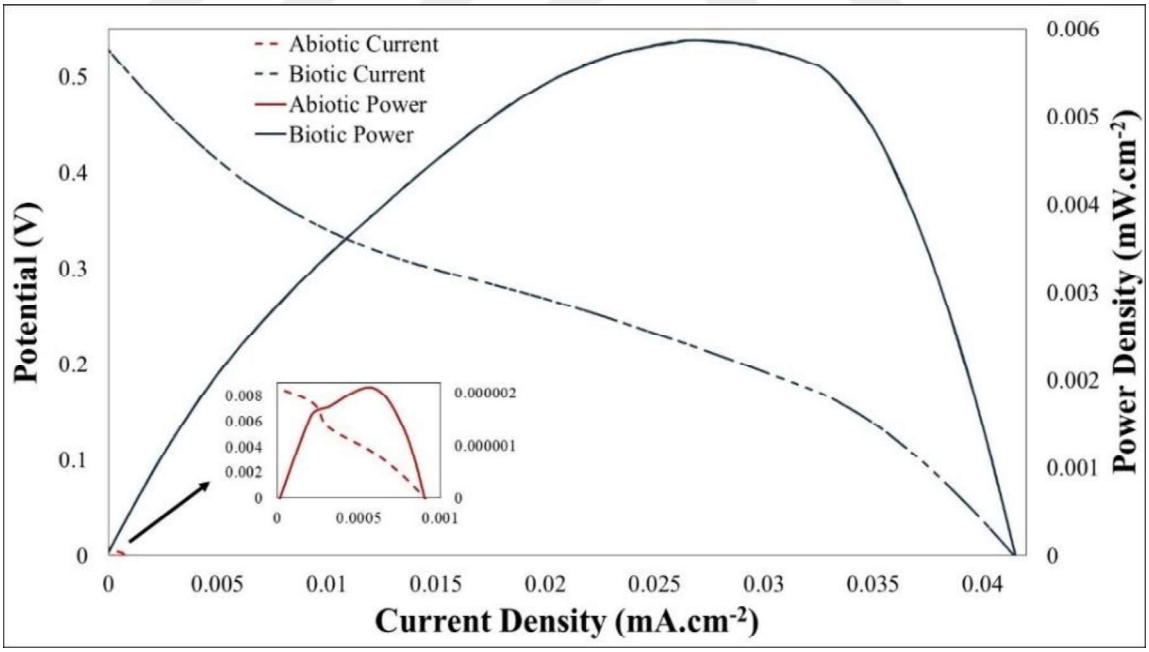

Figure 4.42. Maximum current density and maximum power density comparison between abiotic and biotic fuel cell constructed using FeCoBTC MOF (SSM #4) cathode catalyst.

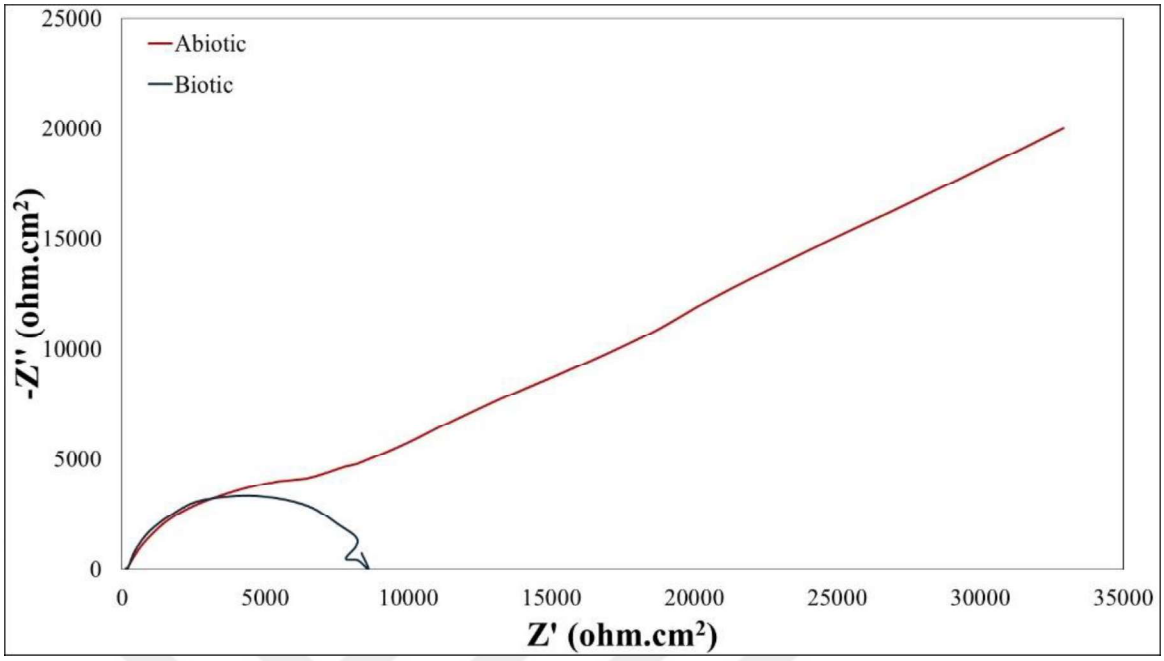

Figure 4.43. EIS curve for MFC with SSM#4 (FeCoBTC).

The electrochemical impedance spectrum in Figure 4.43 for the abiotic and biotic cells constructed with FeCoBTC MOF shows that the internal resistance decreases after the cell is operated with bacteria.

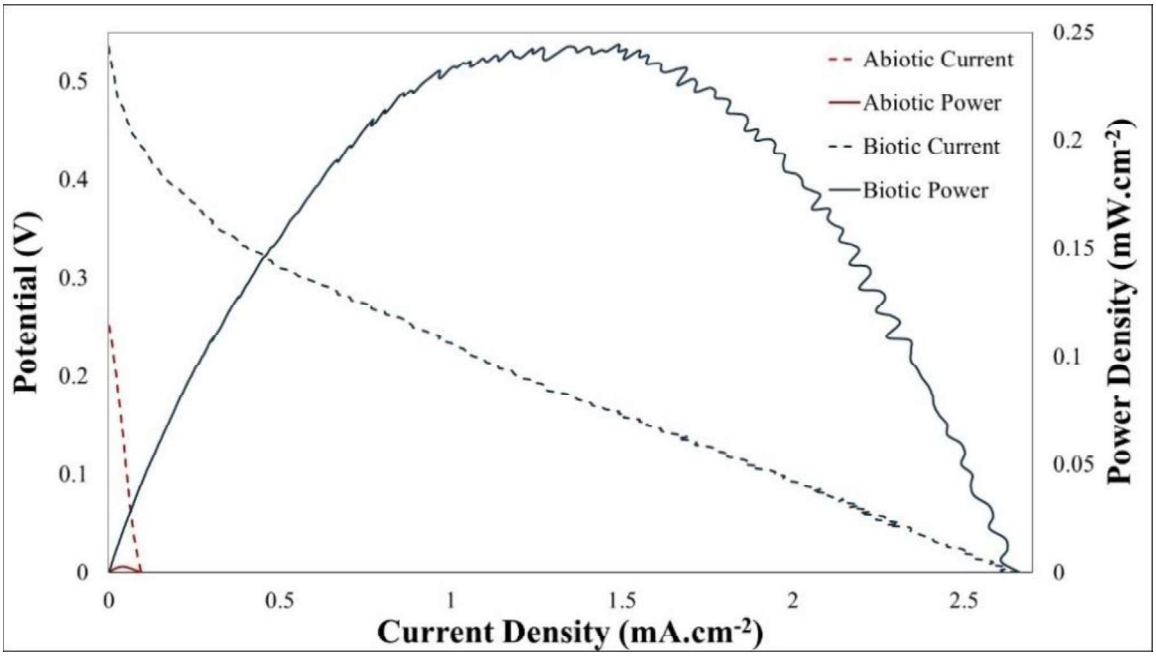

Figure 4.44. Maximum current density and maximum power density comparison between abiotic and biotic fuel cell constructed using CuBTC MOF (SSM #5) cathode catalyst.

Figure 4.44 compares the abiotic and biotic cells constructed with the presence of CuBTC MOF. The biotic cell generated higher current and power than the abiotic cell with the value of 2.4 x 10^{-1} mW/cm^2 and 5.8 x 10^{-3} mW/cm^2 respectively. OCV is 0.53 V and 0.25 V for biotic and abiotic cells respectively.

The electrochemical impedance spectrum in Figure 4.45 for the abiotic and biotic cells constructed with CuBTC MOF shows that the internal resistance decreases after the cell is operated with bacteria.

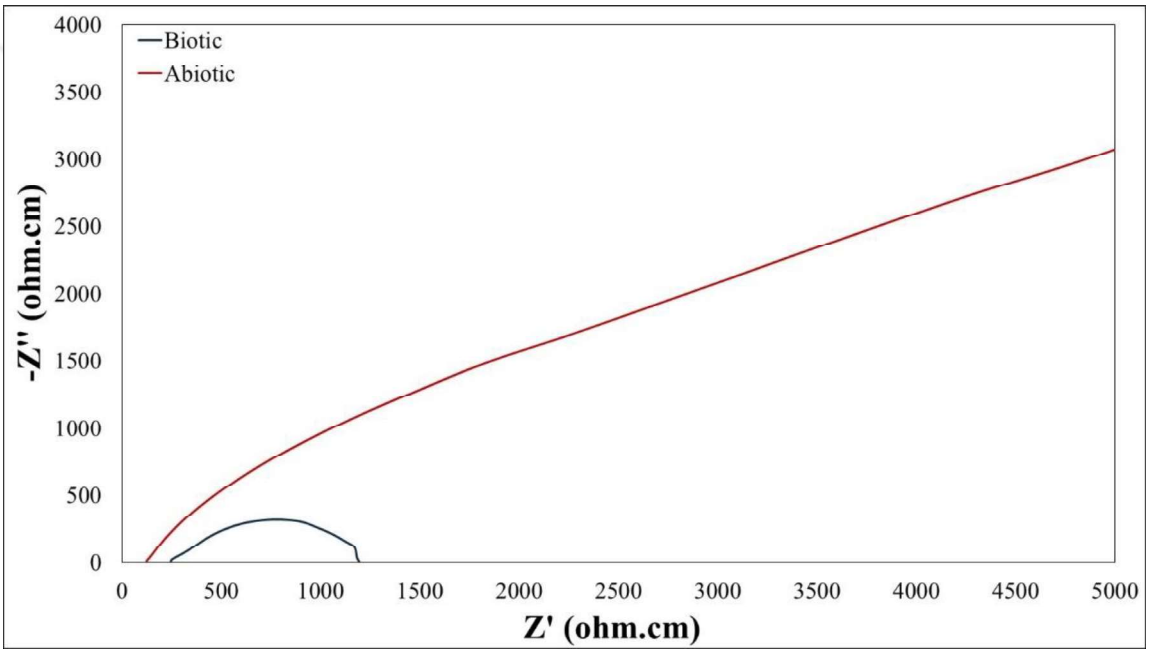

Figure 4.45. EIS curve for MFC with CuBTC (SSM#5).

Figure 4.46 compares the abiotic and biotic cells constructed with the presence of NiBTC MOF. The biotic cell generated higher current and power than the abiotic cell. The irregularity of the biotic cell data could arise from the insufficiency of gas or lack of contact with the system. The maximum power density generated is 5.5 x 10^{-4} mW/cm^2 with biotic cells while it is 1.0 x 10^{-4} mW/cm^2 with abiotic ones. NiBTC helped to produce 5 times larger power from abiotic to biotic. The OCV of the abiotic cell is 0.057 V while the OCV of the biotic cell is 0.13 V.

The electrochemical impedance spectrum in Figure 4.47 for the abiotic and biotic cells constructed with NiBTC MOF shows that the internal resistance decreases after the cell is operated with bacteria.

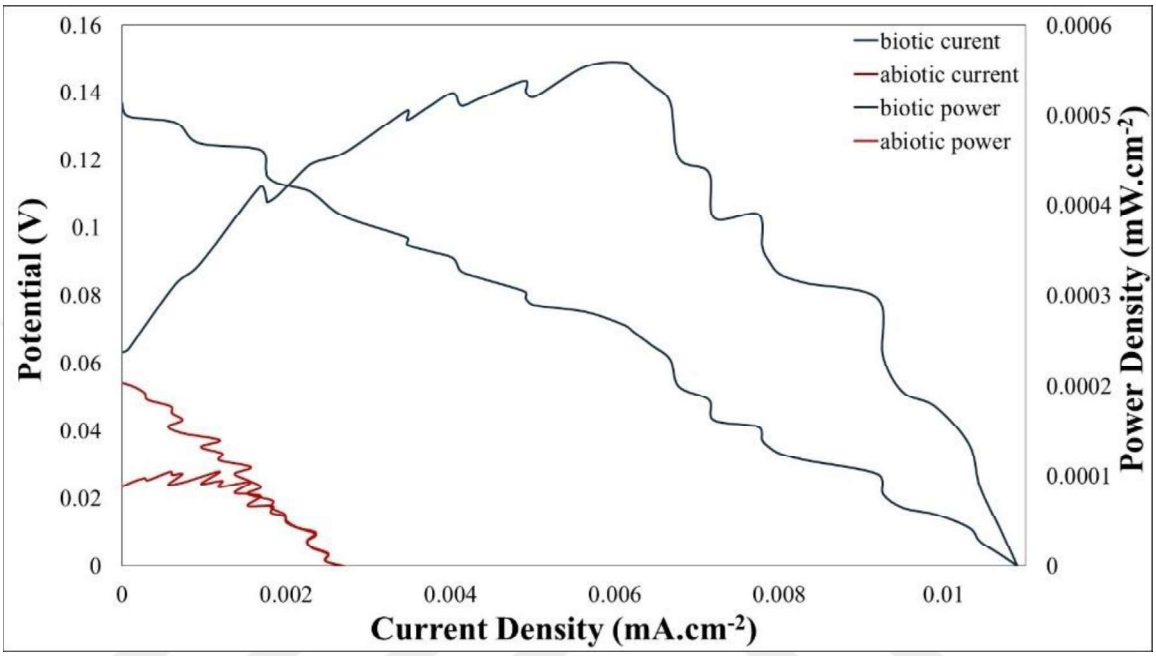

Figure 4.46. Maximum current density and maximum power density comparison between abiotic and biotic fuel cell constructed using NiBTC MOF (SSM #6) cathode catalyst.

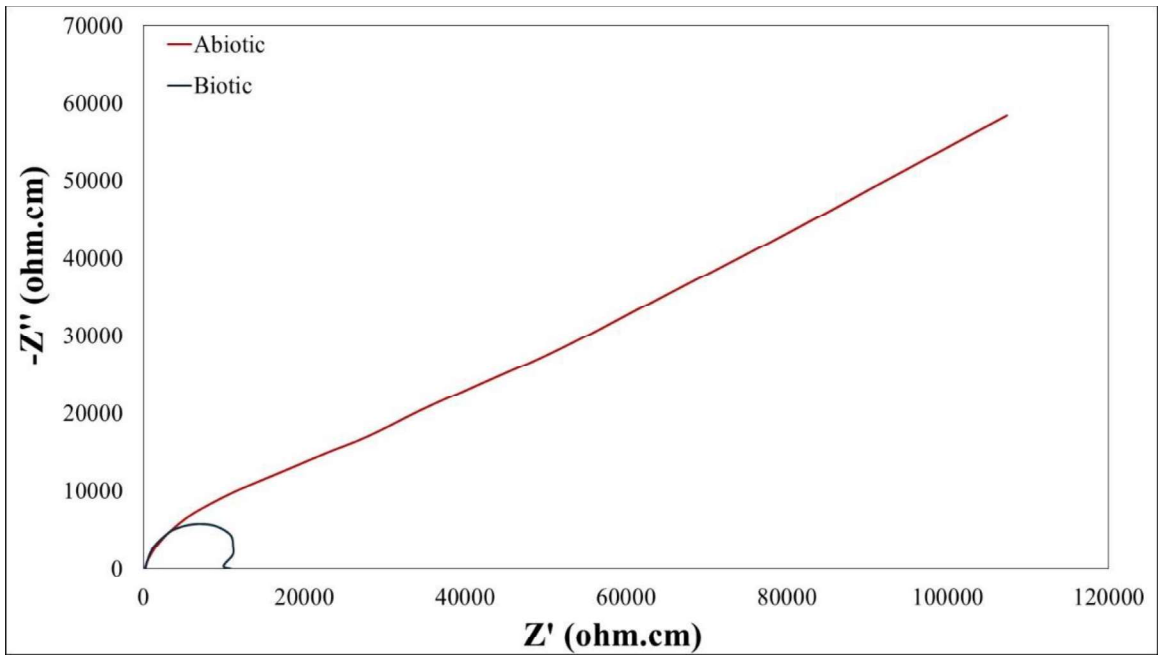

Figure 4.47. EIS curve for MFC with NiBTC (SSM#6).

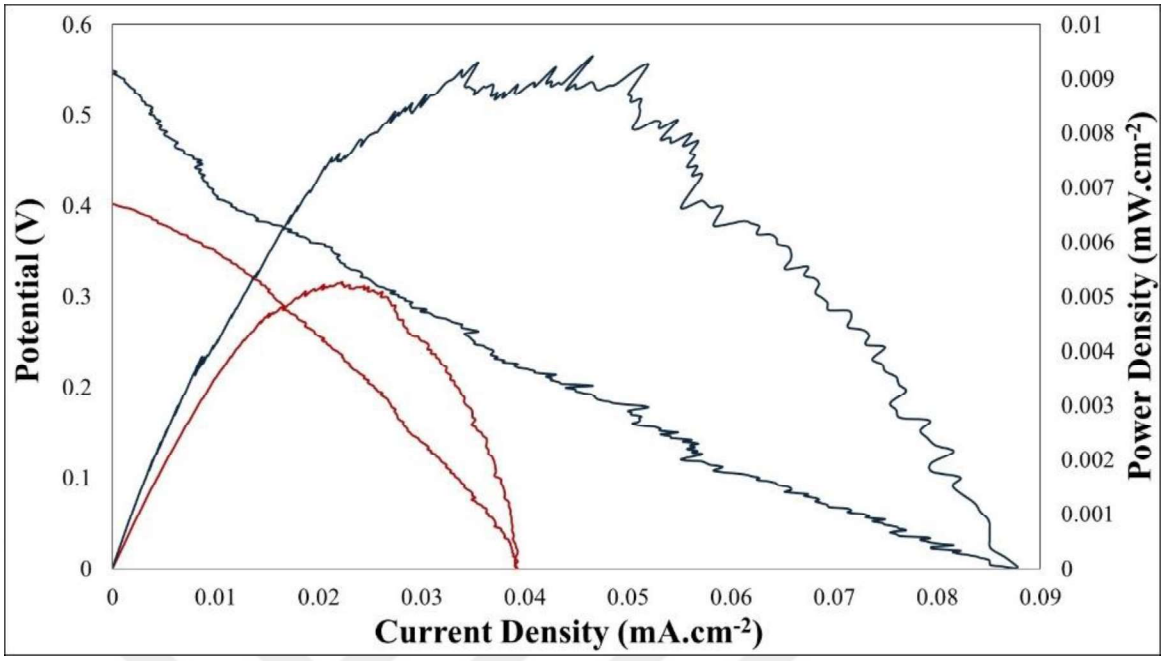

Figure 4.48. Maximum current density and maximum power density comparison between abiotic and biotic fuel cell constructed using CuNiBTC MOF (SSM #7) cathode catalyst.

Figure 4.48 compares the abiotic and biotic cells constructed with the presence of CuNiBTC MOF. The biotic cell generated higher current and power than the abiotic cell. The bimetallic CuNiBTC MOF utilized in MFC and the abiotic cell generates the maximum power density of 5.0 x 10^{-3} mW/cm^2 while the biotic cell generates 9.0 x 10^{-3} mW/cm^2. Although the power generation increased from abiotic to biotic, the performance of CuNiBTC MOF is less than single metal CuBTC MOF. The irregularity of the biotic cell data could arise from the insufficiency of gas or lack of contact with the system. The abiotic OCV is 0.40 V and the biotic OCV is 0.55 V for the system.

The electrochemical impedance spectrum in Figure 4.49 for the abiotic and biotic cells constructed with CuNiBTC MOF shows that the internal resistance decreases after the cell is operated with bacteria.

Figure 4.50 compares the abiotic and biotic cells constructed with the presence of CuBTC MOF. The biotic cell generated higher current and power than the abiotic cell. The maximum power density generated using CuBTC MOF is 4.5 x 10^{-2} mW/cm^2 biotically and

2.5 x 10^{-5} mW/cm^2 abiotically. The irregularity of the biotic cell data could arise from the insufficiency of injected gas. OCV for biotic cell is 0.58 V and for abiotic cell is 0.13 V.

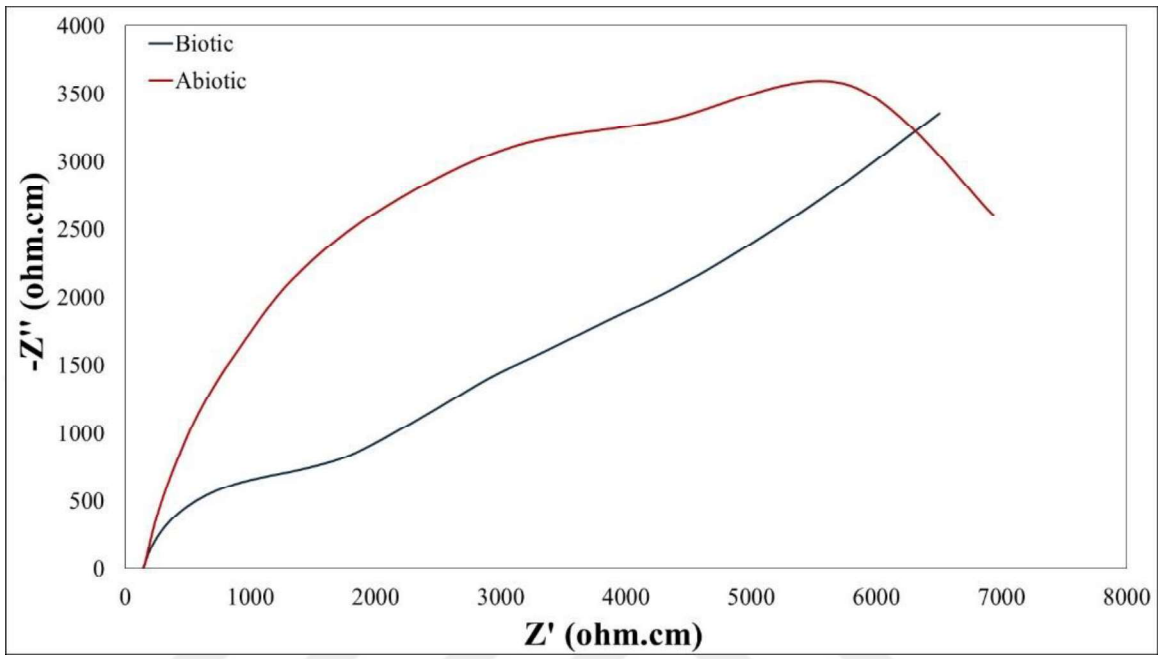

Figure 4.49. EIS curve for MFC with CuNiBTC (SSM#7).

The electrochemical impedance spectrum in Figure 4.51 for the abiotic and biotic cells constructed with CuBTC MOF shows that the internal resistance decreases after the cell is operated with bacteria.

Figure 4.52 compares the abiotic and biotic cells constructed with the presence of NiBTC MOF. The biotic cell generated higher current and power than the abiotic cell. The abiotic cell generates 1.6 x 10^{-4} mW/cm^2 of power and the biotic cell generates 7.0 x 10^{-3} mW/cm^2. The OCV values for abiotic and biotic cells are 0.11 V and 0.25 V respectively.

The electrochemical impedance spectrum in Figure 4.53 for the abiotic and biotic cells constructed with NiBTC MOF shows that the internal resistance decreases after the cell is operated with bacteria.

Figure 4.54 compares the abiotic and biotic cells constructed with the presence of CuNiBTC MOF. The biotic cell generated higher current and power than the abiotic cell. The maximum power density generated by a biotic cell is 1.6 x 10^{-2} mW/cm^2 while an abiotic

cell generates 3.0 x 10^{-4} mW/cm^2 of power. Even though the biotic cell constructed with a cathode catalyst of CuNiBTC has a higher maximum power density than the abiotic cell, The bimetallic CuNiBTC has a lower catalyzing effect than single metal CuBTC when compared. The abiotic cell has an OCV value of 0.15 V while the biotic cell has 0.34 V.

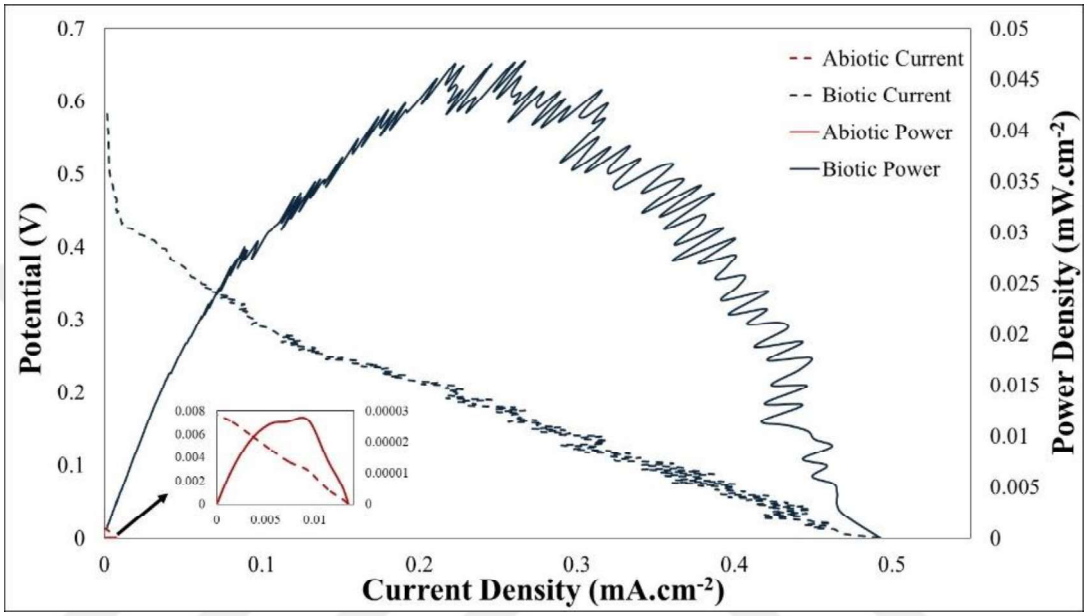

Figure 4.50. Maximum current density and maximum power density comparison between abiotic and biotic fuel cell constructed using CuBTC MOF (SSM #8) cathode catalyst.

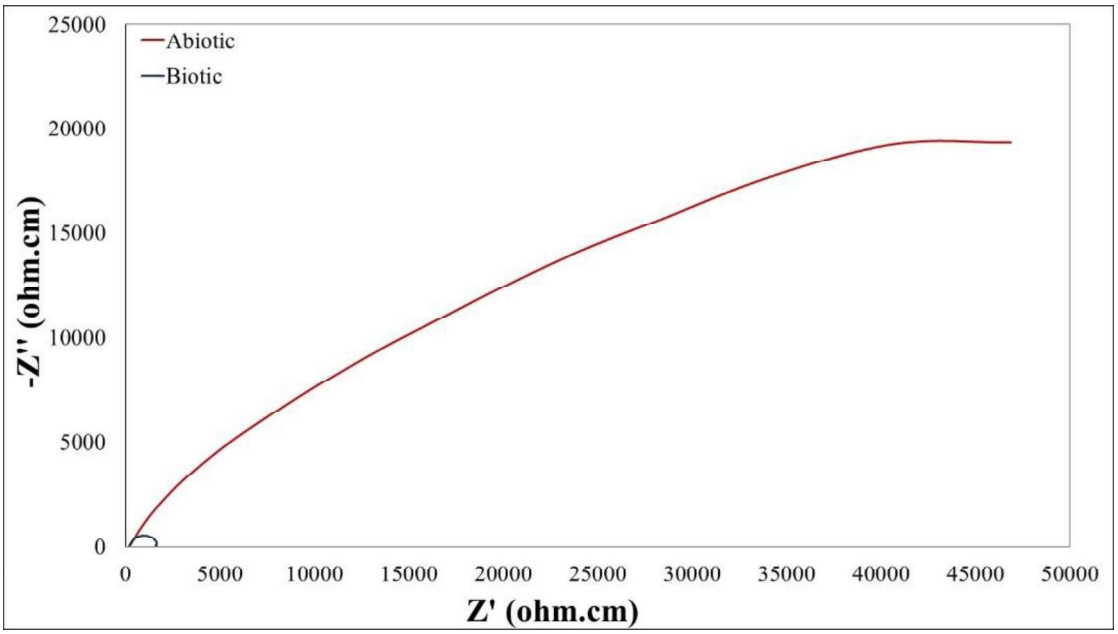

Figure 4.51. EIS curve for MFC with CuBTC (SSM#8).

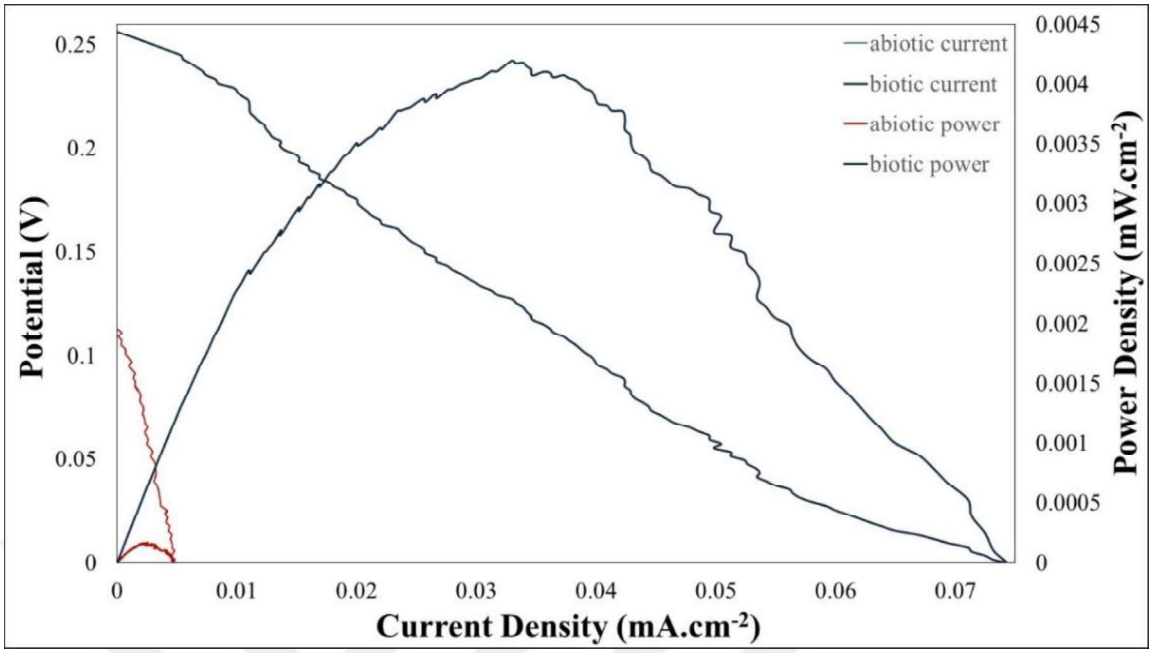

Figure 4.52. Maximum current density and maximum power density comparison between abiotic and biotic fuel cell constructed using NiBTC MOF (SSM #9) cathode catalyst.

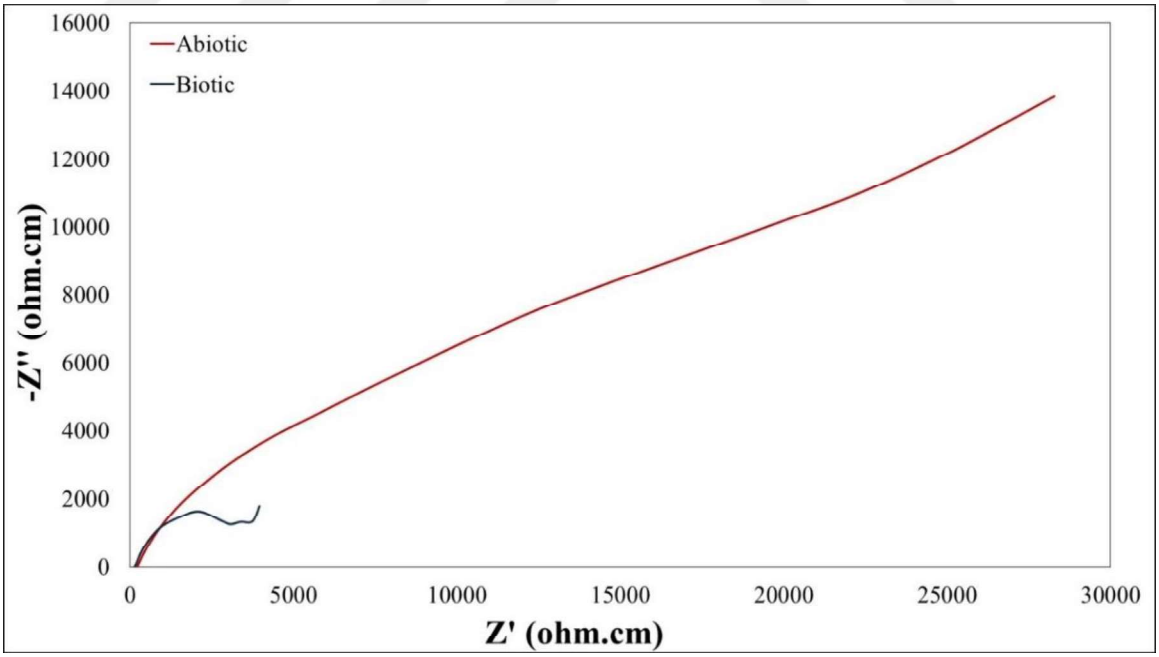

Figure 4.53. EIS curve for MFC with SSM#9 (NiBTC).

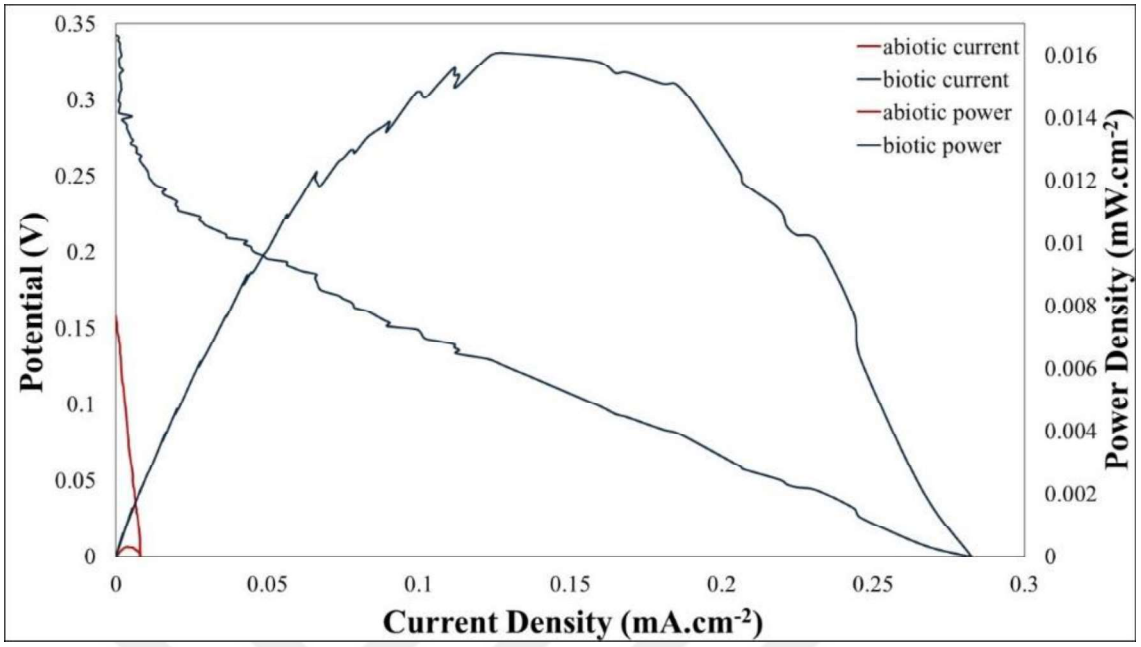

Figure 4.54. Maximum current density and maximum power density comparison between abiotic and biotic fuel cell constructed using CuNiBTC MOF (SSM #10) cathode catalyst.

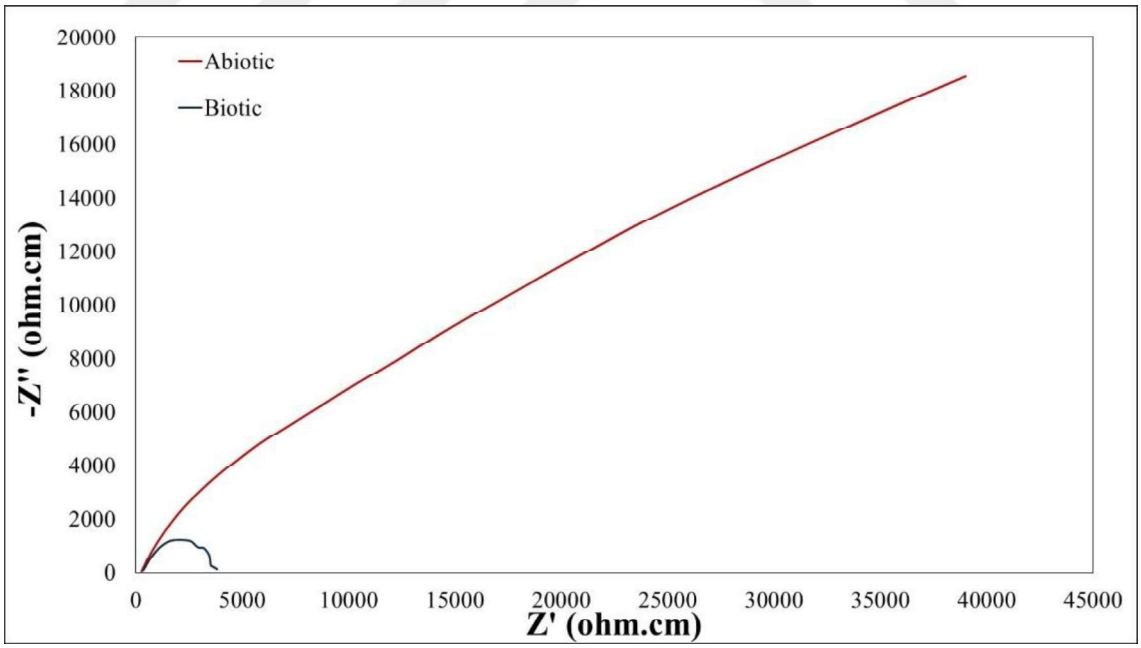

Figure 4.55. EIS curve for MFC with CuNiBTC (SSM#10).

The electrochemical impedance spectrum in Figure 4.55 for the abiotic and biotic cells constructed with CuNiBTC MOF shows that the internal resistance decreases after the cell is operated with bacteria.

Table 4.4. Comparison table for MOFs used in abiotic and biotic fuel cells

MOF	ABIOTIC		BIOTIC	
	Maximum Current Density (mA/cm^2)	**Maximum Power Density (mW/cm^2)**	**Maximum Current Density (mA/cm^2)**	**Maximum Power Density (mW/cm^2)**
FeBTC	1.6×10^{-6}	9.6×10^{-5}	2.0×10^{-2}	2.0×10^{-3}
CoBTC	1.0×10^{-2}	5.0×10^{-4}	3.5×10^{-2}	2.5×10^{-3}
FeCoBTC	8.0×10^{-4}	2.1×10^{-6}	4.1×10^{-2}	6.0×10^{-3}
CuBTC (DMF)	9.4×10^{-2}	5.8×10^{-3}	2.7	2.4×10^{-1}
NiBTC (DMF)	2.8×10^{-3}	1.0×10^{-4}	1.0×10^{-2}	5.5×10^{-4}
CuNiBTC (DMF)	4.0×10^{-2}	5.0×10^{-3}	7.8×10^{-2}	9.0×10^{-3}
CuBTC (NH_3)	7.0×10^{-3}	2.5×10^{-5}	5.0×10^{-1}	4.5×10^{-2}
NiBTC (NH_3)	4.7×10^{-3}	1.6×10^{-4}	7.0×10^{-2}	7.0×10^{-3}
CuNiBTC (NH_3)	8.0×10^{-3}	3.0×10^{-4}	2.7×10^{-2}	1.6×10^{-2}

The comparison between abiotic and biotic fuel cells constructed by using synthesized MOFs as cathode catalysts is given in Table 4.5. The table includes the maximum current density and the maximum power density generated in the cell. Calculations were done by normalizing data concerning the cathode surface area. The comparison table shows that all of the synthesized MOFs successfully produce electricity, besides bacteria contributing to electricity production.

These CV results have shown the ORR abilities of the synthesized MOFs and all of them present an ORR peak at around (-0.5V) and (-0.4V). Hence, these results were supported and correlated with the maximum current and power density curves.

The synthesized MOFs were divided into two groups the synthesized with using DMF solvent and using water/ammonia solvent. The first group contains FeBTC, CoBTC, FeCoBTC, CuBTC, NiBTC, and CuNiBTC while the second group contains CuBTC, NiBTC, and CuNiBTC. The MOFs should be compared into three groups such as the first

group is Fe and Co metal-containing MOFs, the second is Cu and Ni metal-containing and dissolved in DMF and the last one is Cu and Ni metal-containing and solvated in ammonia.

In the first group, it can be said that all MOF-containing fuel cells show increasing max. current density and power density behavior from abiotically operated to biotically operated. When we compare single metal catalysts, CoBTC MOF contained fuel cell has the better max. current and power densities with 3.5 x 10^{-2} mA/cm^2 and 2.5 x 10^{-3} mW/cm^2 respectively. The cell constructed by using the bimetallic FeCoBTC MOF as a cathode catalyst has the highest max. current density with 4.1 x 10^{-2} mA/cm^2 and max. power density of 6.0 x 10^{-3} mW/cm^2 among these three and we can say that combining two metals increases the power production.

The expectation was to improve the electricity generation by changing the catalyst from single metal to double metal and FeCoBTC MOF met the expectations. While the single metal MOFs FeBTC and CoBTC catalyzed the ORR at the cathode of MFC, FeCoBTC has shown a noticeably higher effect. The reason for this increase might be the increasing number of active sites of FeCoBTC. In addition, The varieties of oxidation states also be effective in the reduction of oxygen.

Another comparison can be made among the MOFs that were synthesized using DMF solvent and Copper and Nickel metal precursors. The results showed that the highest power density produced is the cell constructed with CuBTC MOF with 2.4 x 10^{-1} mW/cm^2. Although the bimetallic CuNiBTC MOF has a better effect than NiBTC MOF, CuBTC MOF has the highest effect on the fuel cell.

The last comparison is amongst the MOFs synthesized using ammonia solvent. The fuel cell operated using CuBTC MOF has the highest max. power density and current density of 4.5 x 10^{-2} mW/cm^2 and 5.0 x 10^{-1} mA/cm^2 respectively. The bimetallic CuNiBTC MOF has a higher max. current and power densities than NiBTC but CuBTC is still the better catalyst than the others.

For both DMF solvent synthesis and NH_3 solvent synthesis of Cu and Ni metal-based MOFs, The bimetallic MOFs have not met the expectations of increasing power generation

trend. In addition, for both solvents, CuBTC has the highest values when compared to NiBTC and CuNiBTC. On the contrary, NiBTC has the lowest values. Combining these two metals may have a negative effect on power generation.

The electrochemical impedance spectra were provided to demonstrate the difference between abiotic and biotic cells in terms of internal resistances. EIS results showed that the internal resistance decreased when the cell operated biotically. In other words, the conductivity of all cells increased after bacterial inoculation. This also proves the contribution of bacteria.

In addition to all comparisons, we can comment on the effect of the used solvent during the synthesis of the MOFs of Copper and Nickel metals. Overall, two groups of solvents gave similar results on fuel cells. In other words for the two solvents, CuBTC MOF is the best MOF that affects the fuel cell performance amongst the copper and nickel metal MOFs.

5. CONCLUSION

The objective of this thesis is to use energy-efficient room temperature and sonochemical synthesis techniques to synthesize Cu, Ni, Co, and Fe metal-organic frameworks (MOFs) with organic linker H_3BTC, intending to use them as ORR catalysts for MFC cathodes. SEM, XRD, and XPS analysis are used to evaluate the synthesized frameworks, and the impacts of solvent, metal ion precursor, and second metal doping on the resulting compounds were also investigated.

The application of obtained MOFs as Microbial Fuel Cell (MFC) cathode catalysts is examined by coating stainless-steel mesh (SSM) current collectors with slurries made of carbon black and PVA. SEM is used to show the morphologies of the SSMs coated with slurries containing MOF. The conductivities of the coated SSMs in this thesis study were determined using the results of the Chronopotentiometry analysis. The electrochemical characterization of the composites was carried out using CV for the manufactured MOF-Carbon Black composite coated SSMs.

Current density vs. Power density curves obtained from the LSV results that were normalized concerning the cathode surface area revealed that the SSM coated with the CuBTC-CB composite has the highest power density. In addition, it has the highest maximum current density flow through the cell.

Combining two metal precursors to produce bimetallic MOFs gives slightly higher power density results in the case of iron-cobalt MOFs. FeCoBTC-utilized MFC has the highest maximum power density with the value of 6.0×10^{-3} mW/cm^2 among FeBTC, CuBTC, and FeCoBTC-utilized MFCs. For cupper-nickel MOFs, bimetallic MOF is better than the single metal NiBTC MOF while single metal CuBTC MOF has the highest result of maximum power density with 2.4×10^{-1} mW/cm^2.

The effect of the solvent utilized while synthesizing a MOF can be observed between the DMF solvent and NH_3 solvent. For the cupper-nickel MOFs, it can be observed that the results were similar. Both solvent groups show the highest power density on the fuel cell

constructed with CuBTC MOF. Also, CuNiBTC bimetallic MOFs synthesized with both solvents demonstrate better performance than the single metal NiBTC MOFs.

6. FUTURE WORK

As the binders utilized in this study are electrical insulators, their concentration in the slurries was kept to a minimum to avoid a drop in conductivity; conductive polymeric binders could be investigated as an alternative to PVA to prepare the MOF composite slurries.

The performance of the newly developed electrodes made by coating SSMs should be evaluated by using them in MFCs that have longer operating durations, such as several months so that their stabilities can be examined as well. Additionally, for better reproducibility and comparability with the reported studies in the literature and between the cathode materials in interest with well-established, stable anode electrodes, MFC operations should be carried out using commercially available standard anode materials like carbon cloth, carbon felt, etc.

Although this study showed that E. Coli catalyzed current production, the amount was very small, which may have been caused by the poor exoelectrogenic character of E. Coli K-12. For this reason, additional exoelectrogenic bacteria should be used in future research.

REFERENCES

1. Dharmalingam, S., V. Kugarajah, and M. Sugumar, “Chapter 1.7 - Membranes for Microbial Fuel Cells”, *Microbial Electrochemical Technology*, Elsevier, pp. 143–194, 2019.

2. Dange, P., N. Savla, S. Pandit, R. Bobba, P. S. Jung, P. Kumar Gupta, M. Sahni, and R. Prasad, “A Comprehensive Review on Oxygen Reduction Reaction in Microbial Fuel Cells”, *Journal of Renewable Materials*, Vol. 10, No. 3, pp. 665–697, 2022.

3. Zhang, F., M. D. Merrill, J. C. Tokash, T. Saito, S. Cheng, M. A. Hickner, and B. E. Logan, “Mesh Optimization for Microbial Fuel Cell Cathodes Constructed Around Stainless Steel Mesh Current Collectors” *Journal of Power Sources*, Vol. 196, No. 3, pp. 1097–1102, 2011.

4. Obileke, K., H. Onyeaka, E. L. Meyer, and N. Nwokolo, “Microbial Fuel Cells, A Renewable Energy Technology for Bio-electricity Generation: A Mini-review”, *Electrochemistry Communications*, Vol. 125, pp. 107003, 2021.

5. Gupta, S., A. Patro, Y. Mittal, S. Dwivedi, P. Saket, R. Panja, T. Saeed, F. Martínez, and A.K. Yadav, “The Race Between Classical Microbial Fuel Cells, Sediment-Microbial Fuel Cells, Plant-Microbial Fuel cells, and Constructed Wetlands-Microbial Fuel Cells: Applications and Technology Readiness Level”, *Science of The Total Environment*, Vol. 879, pp. 162757, 2023.

6. Slate, A. J., K. A. Whitehead, D. A. C. Brownson, and C. E. Banks, “Microbial Fuel Cells: An Overview of Current Technology”, *Renewable and Sustainable Energy Reviews*, Vol. 101, pp. 60–81, 2019.

7. Boas, J. V., V. B. Oliveira, M. Simões, and A. M. F. R. Pinto, “Review on Microbial Fuel Cells Applications, Developments and Costs”, *Journal of Environmental Management*, Vol. 307, pp. 114525, 2022.

8. Choi, S., B. Kim, and I. S. Chang, “Tracking of Shewanella Oneidensis MR-1 Biofilm Formation of A Microbial Electrochemical System Via Differential Pulse Voltammetry”, *Bioresource Technology*, Vol. 254, pp. 357–361, 2018.

9. Rabaey, K., N. Boon, S. D. Siciliano, M. Verhaege, and W. Verstraete, “Biofuel Cells Select for Microbial Consortia That Self-Mediate Electron Transfer”, *Applied and Environmental Microbiology*, Vol. 70, No. 9, pp. 5373–5382, 2004.

10. Rinaldi, A., B. Mecheri, V. Garavaglia, S. Licoccia, P. Di Nardo, and E. Traversa, “Engineering Materials and Biology to Boost Performance of Microbial Fuel Cells: A Critical Review”, *Energy & Environmental Science*, Vol. 1, No. 4, pp. 417-429, 2008.

11. Janicek, A., Y. Fan, and H. Liu, “Design of Microbial Fuel Cells for Practical Application: A Review and Analysis of Scale-up Studies”, *Biofuels*, Vol. 5, No. 1, pp. 79–92, 2014.

12. Malik, S., S. Kishore, A. Dhasmana, P. Kumari, T. Mitra, V. Chaudhary, R. Kumari, J. Bora, A. Ranjan, T. Minkina, and V. D. Rajput, “A Perspective Review on Microbial Fuel Cells in Treatment and Product Recovery From Wastewater”, *Water*, Vol. 15 No. 2, pp. 316, 2023.

13. Singh, S., A. Modi, and N. Verma, “Enhanced Power Generation Using A Novel Polymer-Coated Nanoparticles Dispersed-Carbon Micro-nanofibers-based Air-cathode in A Membrane-less Single Chamber Microbial Fuel Cell”, *International Journal of Hydrogen Energy*, Vol. 41, No. 2, pp. 1237–1247, 2016.

14. Boas, J. V., V. B. Oliveira, M. Simões, and A. M. F. R. Pinto, “Review on Microbial Fuel Cells Applications, Developments and Costs”, *Journal of Environmental Management*, Vol. 307, pp. 114525, 2022.

15. Roy, H., T. U. Rahman, N. Tasnim, J. Arju, M. Rafid, R. Islam, N. Pervez, Y. Cai, V. Naddeo, and S. Islam, “Microbial Fuel Cell Construction Features and Application for Sustainable Wastewater Treatment”, *Membranes*, Vol. 13, No. 5, pp. 490, 2023.

16. Selvasembian, R., J. Mal, R. Rani, R. Sinha, R. Agrahari, I. Joshua, A. Santhiagu, and N. Pradhan, “Recent Progress in Microbial Fuel Cells for Industrial Effluent Treatment and Energy Generation: Fundamentals to Scale-up Application and Challenges” *Bioresource Technology*, Vol. 346, pp. 126462, 2022.

17. Costa de Oliveira, M. A., A. D’Epifanio, H. Ohnuki, and B. Mecheri, “Platinum Group Metal-free Catalysts for Oxygen Reduction Reaction: Applications in Microbial Fuel Cells”, *Catalysts*, Vol. 10, No. 5, pp. 475, 2020.

18. Safaei, M., M. M. Foroughi, N. Ebrahimpoor, S. Jahani, A. Omidi, and M. Khatami, “A Review on Metal-Organic Frameworks: Synthesis and Applications”, *TrAC Trends in Analytical Chemistry*, Vol. 118, pp. 401–425, 2019.

19. Priyadarshini, M., A. Ahmad, S. Das, and M. M. Ghangrekar, “Metal Organic Frameworks as Emergent Oxygen-Reducing Cathode Catalysts for Microbial Fuel Cells: A Review”, *International Journal of Environmental Science and Technology*, Vol. 19, No. 11, pp. 11539–11560, 2021.

20. Saiyed, T. A., J.o. Adeyemi, and D. C. Onwudiwe, “The structural chemistry of zinc(II) and nickel(II) dithiocarbamate complexes” *Open Chemistry*, Vol. 19, No. 1, pp. 974–986, 2021.

21. Sharanyakanth, P. S., and M. Radhakrishnan, “Synthesis of Metal-Organic Frameworks (MOFs) and Its Application in Food Packaging: A Critical Review”, *Trends in Food Science & Technology*, Vol. 104, pp. 102–116, 2020.

22. Aftab, L., N. Iqbal, A. Asghar, and T. Noor, “Synthesis, Characterization and Gas Adsorption Analysis of Solvent Dependent Zn-BTC Metal Organic Frameworks”, *Separation Science and Technology*, Vol. 56, No. 13, pp. 2159–2169, 2020.

23. Huelsenbeck, L., H. Luo, P. Verma, J. Dane, R. Ho, E. Beyer, H. Hall, G. M. Geise, and G. Giri, “Generalized Approach for Rapid Aqueous MOF Synthesis by

Controlling Solution pH", *Crystal Growth & Design*, Vol. 20, No. 10, pp. 6787–6795, 2020.

24. Figueroa-Quintero, L., E. V. Ramos-Fernandez, and J. Narciso, "Synthesis and Characterization of the Metal–Organic Framework CIM-80 for Organic Compounds Adsorption", *Materials*, Vol. 15, No. 15, pp. 5326, 2022.

25. Rodríguez, N. A., R. Parra, and M. A. Grela, "Triethylamine As A Tuning Agent of the MIL-125 Particle Morphology and Its Effect on the Photocatalytic Activity", *SN Applied Sciences*, Vol. 2, No. 11, 2020.

26. Guo, H., Y. Zhu, S. Wang, S. Su, L. Zhou, and H. Zhang, "Combining Coordination Modulation With Acid–Base Adjustment for the Control Over Size of Metal–Organic Frameworks" *Chemistry of Materials*, Vol. 24, No. 3, pp. 444–450, 2012.

27. Diring, S., S. Furukawa, Y. Takashima, T. Tsuruoka, and S. Kitagawa, "Controlled Multiscale Synthesis of Porous Coordination Polymer in Nano/micro Regimes", *Chemistry of Materials*, Vol. 22, No. 16, pp. 4531–4538, 2010.

28. Ma, M., D. Zacher, X. Zhang, R. A. Fischer, and N. Metzler-Nolte, "A Method for the Preparation of Highly Porous, Nanosized Crystals of Isoreticular Metal−Organic Frameworks", *Crystal Growth & Design*, Vol. 11, No. 1, pp. 185–189, 2010.

29. Hermes, S., T. Witte, T. Hikov, D. Zacher, S. Bahnmüller, G. Langstein, K. Huber, and R. A. Fischer, "Trapping Metal-Organic Framework Nanocrystals: An *In-situ* Time-resolved Light Scattering Study on the Crystal Growth of MOF-5 in Solution" *Journal of the American Chemical Society*, Vol. 129, No. 17, pp. 5324–5325, 2007.

30. Seetharaj, R., P. V. Vandana, P. Arya, and S. Mathew, "Dependence of Solvents, pH, Molar Ratio and Temperature in Tuning Metal Organic Framework Architecture", *Arabian Journal of Chemistry*, Vol. 12, No. 3, pp. 295–315, 2019.

31. Chen, J., J. Yang, Y. Zhao, Y. Wu, J. Tian, J. Liu, R. Wang, Y. Yang, and Y. Liu, "Research Progress in the Application of Metal Organic Frameworks and Its Complex in Microbial Fuel Cells: Present Status, Opportunities, Future Directions and Prospects", *International Journal of Hydrogen Energy*, Vol. 48, No. 62, pp. 23956–23966, 2023.

32. Chen, J., J. Yang, X. Wang, D. Yang, Q. Wei, Y. Wang, R. Wang, Y. Liu, and Y. Yang, "Zeolitic Imidazolate Framework ZIF-67 Grown on Nial-layered Double Hydroxide/Graphene Oxide as Cathode Catalysts for Oxygen Reduction Reaction in Microbial Fuel Cells", *International Journal of Hydrogen Energy*, Vol. 47, No. 85, pp. 36283–36293, 2022.

33. Chen, J., J. Yang, Y. Zhao, Y. Wu, J. Tian, J. Liu, R. Wang, Y. Yang, and Y. Liu, "Research Progress in the Application of Metal Organic Frameworks and Its Complex in Microbial Fuel Cells: Present Status, Opportunities, Future Directions and Prospects", *International Journal of Hydrogen Energy*, Vol. 48, No. 62, pp. 23956–23966, 2023.

34. Xu, H., J. Huang, C. Lin, J. Zheng, Z. Qiu, Q. Wen, Y. Chen, L. Qi, and Y. Wang, "Bio-functional Metal Organic Framework Composite as Bioanode for Enhanced Electricity Generation By A Microbial Fuel Cell", *Electrochimica Acta*, Vol. 368, pp. 137622, 2021.

35. Jiang, N., J. Song, M. Yan, Y. Hu, M. Wang, Y. Liu, and M. Huang, "Iron Cobalt-Doped Carbon Nanofibers Anode to Simultaneously Boost Bioelectrocatalysis and Direct Electron Transfer in Microbial Fuel Cells: Characterization, Performance, and Mechanism", *Bioresource Technology*, Vol. 367, pp. 128230, 2023.

36. Mukhopadhyay, S., A. Das, T. Jana, and S. K. Das, "Fabricating a MOF Material with Polybenzimidazole Into An Efficient Proton Exchange Membrane", *ACS Applied Energy Materials*, Vol. 3, No. 8, pp. 7964–7977, 2020.

37. Tsai, C.-H., C.-C. Wang, C.-Y. Chang, C.-H. Lin, and Y. W. Chen-Yang, “Enhancing Performance of Nafion ® -Based PEMFC by 1-D Channel Metal-Organic Frameworks as PEM Filler”, *International Journal of Hydrogen Energy*, Vol. 39, No. 28, pp. 15696–15705, 2014.

38. Hossein Zadeh, M., N. Keramati, & M. Mehdipour Ghazi, “Ultrasonic-Assisted Synthesis of New Photocatalyst Based on Fe–Benzenetricarboxylic (Fe–BTC) Metal Organic Framework: Characterization and Photocatalytic Properties”, *Journal of the Iranian Chemical Society*, Vol. 16, No. 2, pp. 401–409, 2018.

39. Tian, P., D. Liu, K. Li, T. Yang, J. Wang, Y. Liu, and S. Zhang, “Porous Metal-Organic Framework $Cu_3(BTC)_2$ As Catalyst Used in Air-Cathode for High Performance of Microbial Fuel Cell” *Bioresource Technology*, Vol. 244, pp. 206–212, 2017.

40. Kim, J. R., S. Cheng, S.-E. Oh, and B. E. Logan, “Power Generation Using Different Cation, Anion, and Ultrafiltration Membranes in Microbial Fuel Cells”, *Environmental Science & Technology*, Vol. 41, No. 3, pp. 1004–1009, 2007.

41. Bosse, S. A., and N. M. Loening, “Using Two-Dimensional Colloidal Crystals to Understand Crystallography”, *Journal of Chemical Education*, Vol. 85, No. 1, pp. 93, 2008.

42. Pednekar, P. P., S. C. Godiyal, K. R. Jadhav, and V. J. Kadam, “Chapter 23 - Mesoporous Silica Nanoparticles: A Promising Multifunctional Drug Delivery System”, *Micro Nano Technology*, pp. 593–621, 2017.

43. Lam, M., C. Schwarz, R. Sharma, and J. Donnelly, “An Introduction to Scanning Electron Microscopy and Science Communication Skills for Undergraduate Chemistry Students”, *Journal of Chemical Education*, Vol. 100, No. 7, pp. 2802–2808, 2023.

44. Powell, C. J., “Improvements in the Reliability of X-Ray Photoelectron Spectroscopy for Surface Analysis”, *Journal of Chemical Education*, Vol. 81, No. 12, pp. 1734–1750, 2004.

45. Sekar, N., R. P. Ramasamy, “Electrochemical Impedance Spectroscopy for Microbial Fuel Cell Characterization”, *Journal of Microbial & Biochemical Technology*, 2013.

46. Kashyap, D., P. K. Dwivedi, J. K. Pandey, Y. H. Kim, G. M. Kim, A. Sharma, and S. Goel, “Application of Electrochemical Impedance Spectroscopy in Bio-Fuel Cell Characterization: A Review”, *International Journal of Hydrogen Energy*, Vol. *39,* No. 35, pp. 20159–20170, 2014.

47. Bard, A. L., and L. R. Faulkner, *Electrochemical Methods Fundamentals and Applications*, Second Edition, John Wiley & Sons, 2001.

48. Zhao, K., Y. Shu, F. Li, and G. Peng, “Bimetallic Catalysts as Electrocatalytic Cathode Materials for the Oxygen Reduction Reaction in Microbial Fuel Cell: A Review”, *Green Energy & Environment*, Vol. 8, No. 4, pp. 1043–1070, 2023.

49. Sánchez, C., P. Dessì, M. Duffy, and P. N. L. Lens, “Gauging Sediment Microbial Fuel Cells Using Open-Circuit Auxiliary Electrodes”, *Journal of Power Sources*, Vol. 527, pp. 231216, 2022.

50. Snihir, I., W. Rey, E. Verbitskiy, A. Belfadhel-Ayeb, and P. H. L. Notten, “Battery Open-Circuit Voltage Estimation by A Method of Statistical Analysis”, *Journal of Power Sources*, Vol. 159, No. 2, pp. 1484–1487, 2006.

51. Nahir, T. M., R. A. Clark, and E. F. Bowden, “Linear-Sweep Voltammetry of Irreversible Electron Transfer in Surface-Confined Species Using the Marcus Theory”, *Analytical Chemistry*, Vol. 66, No. 15, pp. 2595–2598, 1994.

52. Li, X., H. Liu, X. Jia, G. Li, T. An, and Y. Gao, “Novel Approach for Removing Brominated Flame Retardant from Aquatic Environments Using Cu/Fe-Based Metal-

Organic Frameworks: A Case of Hexabromocyclododecane (HBCD)", *Science of The Total Environment*, Vol. 621, pp. 1533–1541, 2018.

53. Aguiar, L. W., C. T. P. da Silva, H. H. C. de Lima, M. P. Moises, and A. W. Rinaldi, "Evaluation of the Synthetic Methods for Preparing Metal Organic Frameworks with Transition Metals", *AIMS Materials Science*, Vol. *5,* No. 3, pp. 467–478, 2018.

54. Oveisi, A. R., A. Khorramabadi-zad, and S. Daliran, "Iron-Based Metal–Organic Framework, Fe(BTC): An Effective Dual-Functional Catalyst for Oxidative Cyclization of Bisnaphthols and Tandem Synthesis of Quinazolin-4(3H)-Ones". *RSC Advances*, Vol. 6*,* No. 2, pp. 1136–1142, 2016.

55. Yuan, A., Y. Lu, X. Zhang, Q. Chen, and Y. Huang, "Two-Dimensional Iron MOF Nanosheet as A Highly Efficient Nanozyme for Glucose Biosensing". *Journal of Materials Chemistry B*, Vol. 8*,* No. 40, pp. 9295–9303, 2020.

56. Akarçay, Ö., S. F. Kurtoğlu, and A. Uzun, "Ammonia Decomposition on A Highly-Dispersed Carbon-Embedded Iron Catalyst Derived From Fe-BTC: Stable and High Performance at Relatively Low Temperatures". *International Journal of Hydrogen Energy*, Vol. 45*,* No. 53, pp. 28664–28681, 2020.

57. Abrori, S. A., M. L. A. Trisno, R. A. Aritonang, I. Anshori, Nugraha, Suyatman, and B. Yuliarto, "Synthesis and Characterization of Metal-Organic Framework (MOF) CoBTC as A Non-Enzymatic Electrochemical Biosensor for Glucose". *IOP Conference Series: Materials Science and Engineering*, Vol. 1045*,* No. 1, pp. 012006, 2021.

58. Wu, Y., X. Song, S. Li, J. Zhang, X. Yang, P. Shen, L. Gao, R: Wei, J. Zhang, and G. Xiao, "3D-Monoclinic M–BTC MOF (M = Mn, Co, Ni) as Highly Efficient Catalysts for Chemical Fixation of CO_2 Into Cyclic Carbonates", *Journal of Industrial and Engineering Chemistry*, Vol. 58, pp. 296–303, 2018.

59. Gupta, N. K., J. Bae, S. Kim, and K. S. Kim, “Terephthalate and Trimesate Metal–Organic Frameworks of Mn, Co, and Ni: Exploring Photostability by Spectroscopy”, *RSC Advances*, Vol. 11, No. 15, pp. 8951–8962, 2021.

60. Naik Shreyanka, S., J. Theerthagiri, S. J. Lee, Y. Yu, and M. Y. Choi, “Multiscale Design of 3D Metal-Organic Frameworks (M−BTC, M: Cu, Co, Ni) via PLAL Enabling Bifunctional Electrocatalysts for Robust Overall Water Splitting”. *Chemical Engineering Journal*, Vol. 446, pp. 137045, 2022.

61. Gao, T., Y. Cai, Q. Wan, P. Deng, Q. Cai, N. Peng, H. Xu, and Y. Liu, “Terrace-Like 2D Hierarchically Porous Iron/Cobalt Metal-Organic Framework: Ambient Fast Synthesis and Efficient Oxygen Evolution Reaction Application”, *Small*, Vol. 19, No. 46, 2023.

62. Dalakoti, S., N. Singh, H. N. Wamba, J. Kaishyop, S. Divekar, A. Arya, and S. Dasgupta, “Rapid Aqueous Medium Organization of Trimesate Metal–Organic Frameworks of Cu, Fe: Exploring Suitability in Gas Separation”, *ACS Applied Engineering Materials*, Vol. 1, No. 12, pp. 3309–3322, 2023.

63. Gao, P., X.-Y. Sun, B. Liu, H.-T. Lian, X.-Q. Liu, and J.-S. Shen, “Cu MOF-Based Catalytic Sensing for Formaldehyde”, *Journal of Materials Chemistry C*, Vol. 6, No. 30, pp. 8105–8114, 2018.

64. Yaqoob, L., T. Noor, N. Iqbal, H. Nasir, and N. Zaman, “Development of Nickel-BTC-MOF-Derived Nanocomposites with rGO Towards Electrocatalytic Oxidation of Methanol and Its Product Analysis”, *Catalysts*, Vol. 9, No. 10, pp. 856, 2019.

65. Israr, F., D. Chun, Y. Kim, and D. K. Kim, “High Yield Synthesis of Ni-BTC Metal–Organic Framework with Ultrasonic Irradiation: Role of Polar Aprotic DMF Solvent”, *Ultrasonics Sonochemistry*, Vol. 31, pp. 93–101, 2016.

66. Cheng, M., H. Fan, Y. Song, Y. Cui, and R. Wang, “Interconnected Hierarchical $NiCo_2O_4$ Microspheres as High-Performance Electrode Materials for Supercapacitors”, *Dalton Trans.*, Vol. 46, No. 28, pp. 9201–9209, 2017.

67. Abd El Salam, H. M., and T. Zaki, “Removal of Hazardous Cationic Organic Dyes from Water Using Nickel-Based Metal-Organic Frameworks”, *Inorganica Chimica Acta*, Vol. 471, pp. 203–210, 2018.

68. Akhavan-Bahabadi, Z., H. R. Zare, Z. Mohammadpour, and B. B. Mirjalili, “Improvement of Anti-Corrosion Performance of A Cu-Ni Bimetallic Organic Framework Smart Coating Using Amino-Substitution Triazole”, *ChemistrySelect*, Vol. 8, No. 24, 2023.

69. Jiang, H., S. Gong, S. Xu, P. Shi, J. Fan, V. Cecen, Q. Xu, and Y. Min, “Bimetal Composites for Photocatalytic Reduction of CO_2 to CO in the Near-Infrared Region by the SPR effect”, *Dalton Transactions*, Vol. 49, No. 16, pp. 5074–5086, 2020.